Constitutive Models for Root-Soil Contact Interface Considering Hydro-Mechanical Effects

2020

Haruka TOMOBE

Acknowledgements

This study is based upon a series of research conducted over five years by the author who has been working as master and doctoral course student at the Graduate School of Agriculture, Kyoto University.

First and foremost, I would like to express sincere gratitude to Professor Akira Murakami for his ever-present supports, guidance and encouragement. I also extend my appreciation to Associate Professor Kazunori Fujisawa for precious discussions for numerical simulations of deformable bodies.

I would like to express sincere thanks to the members of my Dissertation Committee, Professor Masayuki Fujihara, Professor Kimihito Nakamura, and Professor Tatsuhiko Shiraiwa, for their insights and suggestions to completion of this thesis.

I am thankful to Dr. Sharma Vikas who was a senior of the doctoral course and working now in Indian Instutite of Technology, whose advices are vital to complete this work. I am also grateful for my laboratory member Michael Koch for his warm advices. I also take the opportunity to thank my laboratory members, family, and friends.

Contents

List of Figures

List of Tables

Chapter 1

Introduction

1.1 Background

Plant-soil mechanical interaction plays an essential role in sustaining water supply and plant production, and the interaction is a significant research subject from the standpoints of geotechnical engineering and plant production science for decades. It is widely accepted that soils are vital materials for building and supporting artificial/biological agricultural objects such as dams, irrigation/drainage open channels, agricultural fields, as well as crops. As can be seen on earth dams and embankments, soil domains are covered by vegetation which interacts with the microscopic structure and stability of soils (Ali and Osman, 2008; Liang et al., 2017). Since soil behavior is affected by microscopic soil structure such as void ratio, contact conditions of soil particles, and contamination of natural/artificial fibers, the presence of the plant roots affects the mechanical characteristics of soil structure. During the last four decades, it has been reported that plant roots often increase the shear strength of soils by reinforcing apparent cohesion and that the reinforcement is beneficial to increase the stability of soils (Endo 1980; Gray and Ohashi., 1983; Abe and Ziemer, 1991;Docker and Hubble., 2008; Hejazi et al., 2012). On the other hand, the mechanical stability of the crops is influenced by the mechanical strength of soils (Berry et al., 2003; 2004), which is an important research subject for sustainable cereal production. Cereals have their grains at their upper sides of the body, hence, loss of stability called lodging causes the decline of both the yield and the qualities. For instance, it is reported that severe lodging causes more than 45 $\%$ of yield losses (Baker et al., 1998; 2014), and also causes low grain quality due to the delay of the harvest. Since the failure of root-soil systems induces severe and permanent lodging, it is essential to present mathematical and physical models to understand and predict plant-soil interactions to sustain the productivity of cereals.

Vegetation reinforces surface layers on both of artificial soil structures and natural slopes (Bischetti et al., 2010; Liu et al., 2016; Bizet et al., 2018). Rainfall events often cause erosion of soil particles on natural/artificial slopes(Das et al., 2018), which induces geo-

disasters of soil structure as dams, embankments, slopes, roads, and other foundations. It is often employed that slope protections by using concrete, cemented soils, and artificial fibers. Although these methodologies substantially increase the resistance of the soil structures, there are annoying problems that the deterioration of concrete, cement, and synthetic fibers induces the reduction of the function. The deterioration also result in increasing the life-cycle costs of soil structures. By contrast, biological reinforcement such as plant roots increases the shear strength of soils (Hejazi et al., 2012) with far less financial costs than the artificial materials since biological materials grows and increase the resilience of the soil structures against the erosion. The reinforcement is relatively weak and hard to predict quantitatively. Therefore, the utilization of biological reinforcement is still less common than artificial ones.

From another standpoint, soil supports crops to prevent lodging. Lodging is defined as a permanent displacement of cereals (Baker et al., 1998) and induced by loss of stability of plant body and rhizosphere. Prevention of lodging is one of the most critical problems to sustain yield and quality of cereals (Baker et al., 1998; Berry et al., 2004) since the lodging causes pre-harvest sprouting, diseases, and decline of the radiation utilization efficiency. There are two types of lodging: stem lodging and root lodging. Stem lodging is caused by bending or breakage of plant stems, and there has been presented that some schemes to estimate and prevent this type of lodging (Ookawa et al., 2010). The root lodging, however, is still hard to predict, and the prediction/prevention is being challenged. Beker et al. (1998) proposed a method to predict the root lodging of wheat, which is an empirical model based on numerous observation data from field experiments. Though Baker's model is convenient for roughly simulating the lodging of wheat, it has difficulty for its accuracy when it is used for breeding or field management. To increase the accuracy of the lodging model, it is necessary to propose physics-based methods such as numerical simulations for plant-soil systems.

The problems mentioned above motivate researchers to investigate and predict plant-soil mechanical interactions for decades. it has been presented that roots reinforce the rooted soils, and the reinforcement is visible as incremental cohesion/friction. The reinforcement model has been utilized for the homogeneous approach which models rooted soils as homogeneous domain. In the 1990s, Abe and Ziemer (1990) propose a method to estimate the shear strength of the rooted soils from material properties and geometries of roots and soils. The Mohr-Coulomb model is one of the most widely-used models to estimate the stability of rooted soils in artificial/natural slopes (Rahardjo et al., 2009; Rahardjo et al., 2014; Eab et al., 2015; Zhu et al., 2017).

Recently, Dupuy et al. (2007; 2018) and Michovski et al. (2011) propose direct simulations of root-soil contact problems based on the Finite Element Method (FEM) and simple root-soil contact models. They utilize commercial software packages of the FEM with some mechanical data of plants, soils, and root-soil interfaces to directly predict the deformation

of roots, soils, and contact between roots and soils. These approaches are substantially innovative since the methods can utilize the exact root morphology in the prediction, which has not been done in the previous approaches. Their approach clearly visualizes the stress fields of the soils and roots, which provides far more detailed information to estimate and understand the deformation of rooted soils. For instance, Dupuy's approach gives a prediction of the failure zone of roots and soils and shows how wind forces are propagated from roots to soils, which did not estimate by the conventional approaches based on the Mohr-Coulomb model.

Although the direct approaches are novel and accurate, some important problems are still remained about the constitutive model of root-soil contact interfaces to utilize the models for practical problems such as soil erosions and lodging. The primary problem is the absence of a consistent method to measure the shear strength of root-soil interfaces. The FEM with contact models necessitates slip criterion of root-soil interfaces which express cohesion and frictions. However, there have not been presented any methods which accurately measure cohesion and friction of root-soil interfaces.

Further, another problem exists for the discretization scheme of the root-soil interfaces. Dupuy et al. (2007) utilized the Node-To-Node (NTN) approach, which does not allow slip of the interface, and Michovski et al. (2011) used the Line Element (LE) approach which requires special conversion from 2-D or 3-D scanned data to straight or curved lines. Therefore, to utilize the direct simulation of root-soil contact problems for the design and management of the soil structures and crops, it is necessary to develop both of discretization scheme of root-soil interfaces and software to predict the root-soil contact problems.

1.2 Motivation and objectives

This thesis aims to present a set of experiments, constitutive models, and numerical methods for predicting the deformation of rooted soils based on the computational contact mechanics (Hughes et al., 1976;) approach with FEM. As discussed in the previous subsection, numerical simulations of root-soil contact problem necessitate accurate measurements of shear strength of root-soil interfaces such as frictional coefficient of root-soil interface, and cohesion induced by suction. However, little experiments are available for measuring frictional coefficients of root-soil interfaces, and no models are presented to obtain cohesion in root-soil interfaces induced by suction. This thesis presents two novel experiments to measure friction and suction-induced cohesion, respectively. From these experiments, two models that are utilized for soil-soil interfaces are introduced to give mathematical expressions for friction (Mohr-Coulomb model) and suction-induced cohesion (Vilar model), which are implemented for numerical simulations of root-soil contact problems. It is also discussed in the previous subsection that NTN and LE approaches have limitations for expressing such root-soil contact phenomena as (1) slip between roots and soils, (2) separation between

roots and soils, or (3) complex root geometry and surface topology of root-soil interfaces. These limitations result in reduced accuracy or high pre-processing costs in the previous results. The Node-To-Segment (NTS) approach which is a modified approach of the NTN, hence, is newly introduced in the thesis to avoid these problems, which can express (1) slip between roots and soils under large-slip conditions, (2) separation/contact between roots and soils, and (3) geometrical nonlinearity of roots and soils. Although the original version of the NTS approach induces ill-convergence problems when it is applied for root-soil contact problems (Dupuy et al., 2008), a novel scheme is successfully introduced to stabilize the NTS approach. The following chapters are devoted to the set of experiments, modeling, and numerical simulations.

In Chapter 2, the outline of the NTS approach with FEM (NTS-FEM) is briefly explained to model root-soil contact interfaces. The chapter presents kinematics of root-soil contact problems, mathematical expressions of the governing equation, the discretization and linearization of the governing equation, and the solution algorithm for numerical simulations. Since the solution algorithm for the numerical simulation necessitates the constitutive modeling of roots, soils, and root-soil interfaces, the chapter also discusses experiments and models for the mechanical characteristics of them.

Chapter 3 proposes a novel pull-out apparatus to measure the cohesion and frictional coefficient of root-soil interfaces, both of which are essential to perform root-soil contact simulations. The pull-out apparatus is validated by measuring the frictional coefficient of a steel-sand interface, which has been measured in previous studies (Uesugi and Kishida., 1986). It is also confirmed that shear zones in experiments are not mainly in the roots or soils, but the root-soil interface through the comparison between the steel-sand tests and the wood-sand tests. Afterward, the shear strength of root-soil interfaces is measured by using a paddy soil, and the apparatus accurately measure a root of barley, which suggests that the Mohr-Coulomb (MC) model well governs the shear stress of root-soil interfaces as well as the frictional coefficients and the cohesion.

Chapter 4 presents a 2-D experiment and a numerical simulation of the lodging problem, which utilizes the apparatus presented in the previous chapter. The chapter contains the implementation of the NTS approach, a novel stabilization scheme of the NTS approach, and the procedure to measure the material parameters of roots, soils, and root-soil interfaces. The chapter also contains numerical simulations for pull-out tests and lodging problems to validate and confirm the accuracy of the present method. The results are highly consistent with both of the experiments and suggested that the present method is capable of reproducing the deformation of rooted soils.

Chapter 5 describes a set of methods to measure, model, and predict the shear strength of root-soil contact interfaces under dynamic suction conditions, the model of which is based on Mohr-Coulomb-Vilar (MCV) model with the NTS approach. The chapter extends the MC model to predict the shear strength of root-soil interfaces under dynamic suction

conditions.

Chapter 6 shows validations and applications of the root-soil contact simulation based on the MCV model. The MCV model is first validated by simulating the suction-controlled pull-out tests and then applied for a numerical experiment of pull-out tests under dynamic suction conditions. The results show that the MCV-NTS approach expresses the root-soil contact behavior under dynamic suction conditions. The numerical experiment of the pull-out behavior of roots is performed, and the effect of wet-dry conditions is reasonably estimated as the pull-out force of roots.

Chapter 7 remarks on the conclusion of the whole thesis and describes future studies.

Chapter 2

Continuum Model for Root-Soil Contact Problem

2.1 Introduction

The root-soil contact problem is challenging from the viewpoint of numerical simulations for two reasons; geometrical and material nonlinearity induced by root-soil contact phenomena. Roots often exist as composite materials with soils in natural conditions, where roots and soils contact each other. Numerous investigations are performed to provide a mechanical model that estimates the root-soil contact problem. Early investigations propose mathematical models of a root-soil contact problem for rooted soils, the contact model of which is implicitly expressed by utilizing the apparent cohesion in terms of Mohr-Coulomb model (Gray and Ohashi 1983; Abe and Ziemmer, 1991; Mickovski et al., 2010, 2011). For instance, Abe and Ziemmer (1991) investigate the relationship between the properties/numbers of roots and the apparent cohesion and propose a new root-induced reinforcement model. Although the contact of root and soil is not directly solved but indirectly considered, the strategies were the possible best ones under the capacity of computers in the past.

Recent advances of computers allow more computationally expensive approaches such as direct stimulation of root-soil contact problems, which call forth more micro-scaled root-soil contact interfaces. Dupuy et al. (2007) and Mickovski et al. (2011) utilize the FEM to model and predict the root-soil contact problems, in which roots and soils are modeled by based on the finite strain theory. They utilized 3-D models of roots and soils directly in the simulations and succeeded in predicting the deformation of the rhizosphere. This novel approach necessitates a novel research question; how the contact, separation, stick, and slip of root-soil contact interfaces can be modeled consistently.

This chapter presents a consistent model, formulations, and computational implementation to predict root-soil contact problems accurately. The general formulations for friction-

cohesion contact problems are introduced in the second section, which gives a series of mathematical expressions of the root-soil contact problems. The third section proposes constitutive models and physical tests to measure the model parameters for root and soil domains suitable for root-soil contact problems. The material tests and modeling of root-soil interfaces are also discussed in the fourth section based on the Computational Contact Mechanics (CCM). The last section summarizes the models and physical tests for roots, soils, and root-soil interfaces and shows how present models are utilized for the following chapters.

2.2 Continuum-based formulation for root-soil contact problem

This section summarizes general formulations for frictional-cohesion contact problems. First, the contact kinematics is described where the schematics of the contact problem and mathematical expression of the deformation and contact, stick, and slip are given based on the CCM. Second, it is also shown that the weak form of contact problems in terms of FEM and the NTS approach. Afterward, the discretization and matrix form of domains and contact surfaces are explained in which friction and cohesion are also modeled and discretized by using contact elements. Lastly, the solution algorithm is discussed.

2.2.1 Formulation of root-soil contact interface

This section reviews the contact kinematics and its formulation in terms of CCM. The formulation of roots and soils were done by using the finite elasto-plasticity and the CCM. This section summarizes the derivation of the governing equation of contact problems and its discretization by using the NTS approach (Wrigger, 2006). Let us consider two deformable bodies, in which one is usually denoted as the master body $\left(\Omega_1, \overline{\Omega}_1\right)$ and another as the slave body $\left(\Omega_2, \overline{\Omega}_2\right)$. Both bodies can undergo deformation through motion during $[0, t]$ and come into contact, where (Ω_1, Ω_2) is identified at the current configuration and $\left(\overline{\Omega}_1, \overline{\Omega}_2\right)$ is in the initial configuration (Fig. 2.1). Further, in the current configuration, boundaries of each body can be divided into three non-overlapping subdivisions: displacement boundaries, traction boundaries, and contact boundaries.

Accordingly, the governing equation for the displacement field is given by a virtual work equation,

$$\begin{aligned} \delta W = &\left(\int_\Omega \sigma_{ij} \frac{\partial \delta u_i}{\partial x_j} d\Omega - \int_\Omega f_i \delta u_i d\Omega - \int_\Gamma t_i \delta u_i d\Gamma \right)^m \\ + &\left(\int_\Omega \sigma_{ij} \frac{\partial \delta u_i}{\partial x_j} d\Omega - \int_\Omega f_i \delta u_i d\Omega - \int_\Gamma t_i \delta u_i d\Gamma \right)^s + \delta W^c = 0, \end{aligned} \tag{2.1}$$

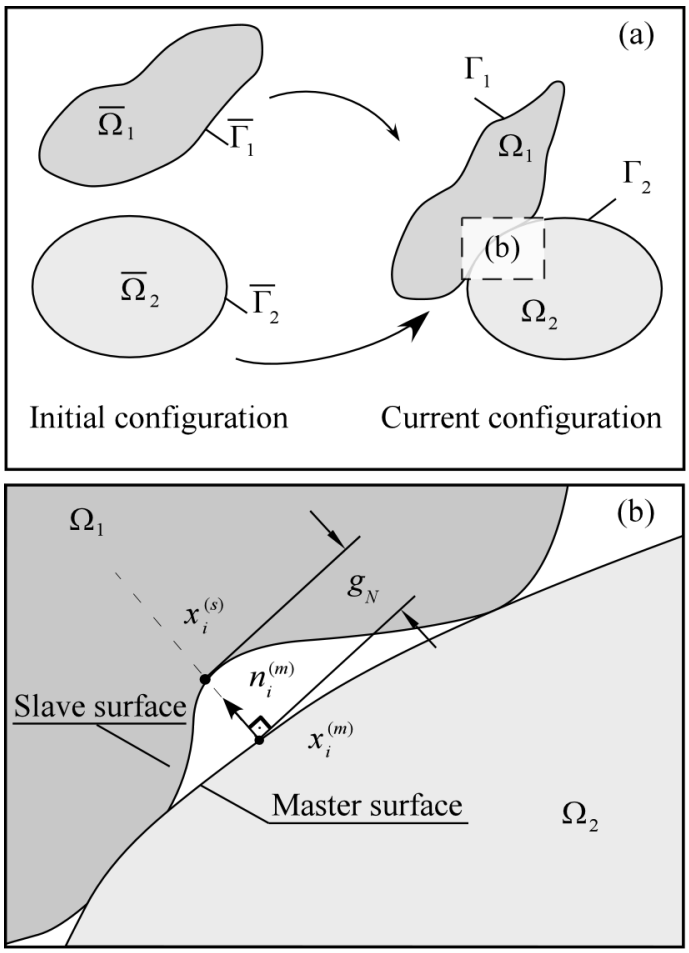

Figure 2.1: Schematic view of contact kinematics.

where i and j are subscripts which have values of 1, 2, 3 in the three-dimensional Euclidean space, δW is the virtual work, superscripts m and s denote the master/slave notations in the current configuration, Γ is the boundary of the domains, σ_{ij} is the Cauchy stress tensor, δu_i is the virtual displacement vector, δ is the variational operator with respect to displacement, f_i is the body force vector, and t_i is the traction vector. The first and second terms are identical to the conventional virtual work for one-body problems (Hashiguchi and Yamakawa, 2013). The last term represents the virtual work for the contact interfaces, which is derived from the constraint conditions such as the non-penetration conditions, friction, and cohesion (Wriggers, 2006). The virtual work of contact interfaces δW^c is generally taking the form of

$$\delta W^c = \int_\Gamma t_{Ni} \delta g_{Ni} d\Gamma + \int_\Gamma t_{Ti} \delta g_{Ti} d\Gamma, \tag{2.2}$$

in which t_{Ni} and t_{Ti} are the normal and the frictional stress, respectively. g_{Ni} is the normal gap and g_{Ni} is the tangential displacement from the initial contact point (Fig. 2.1). Here, the first term enforces the normal contact stress to prevent overlaps between the bodies, and the second term works as the tangential one such as friction and cohesion. This interfacial virtual work δW^c is analogous to the well-known virtual work, and it becomes zero under contactless conditions (Wriggers, 2006).

The first and the second term of the governing equation (Eq. (2.1)) are discretized by using the finite elements, and the last one is discretized by using the NTS elements. The bodies are initially discretized by finite elements, as illustrated in Fig. 2.1. Then, each node on the slave surface is paired with the closest segment on the master surface (Fig. 2.2). Since the contact element mechanically connects a node to a segment, it is called an NTS element. From the geometrical relationship, the normal gap vector g_{Ni}, tangential gap vector g_{Ti} is formulated by using the nodal coordinates. Under the penalty method, a slave node and a master segment are connected by virtual springs, as depicted in Fig. 2.2 (b) and (c), which is the penalty parameter. The frictional stress is relaxed if it is greater than the frictional strength, which is described as the parallel shift of the virtual spring from the initial contact point (Fig. 2.2). Above all, the governing equation is given by

$$\delta W_c = \sum_{A=1}^{ne} \delta {u_i}^{d(A)} {R_i}^{d(A)} + \sum_{A=1}^{nc} \delta {u_i}^{c(A)} {R_i}^{c(A)} \tag{2.3}$$

where A and B denote the identification numbers of nodes in each element, ne and nc are the numbers of finite elements and NTS elements, respectively, $\delta {u_i}^{d(A)}$ and $\delta {u_i}^{c(A)}$ are variations of the nodal displacement vectors for the bodies and the contact interfaces, ${R_i}^{d(A)}$ and ${R_i}^{c(A)}$ are the residual vectors. The detailed derivation of the previous equation is displayed in the next section.

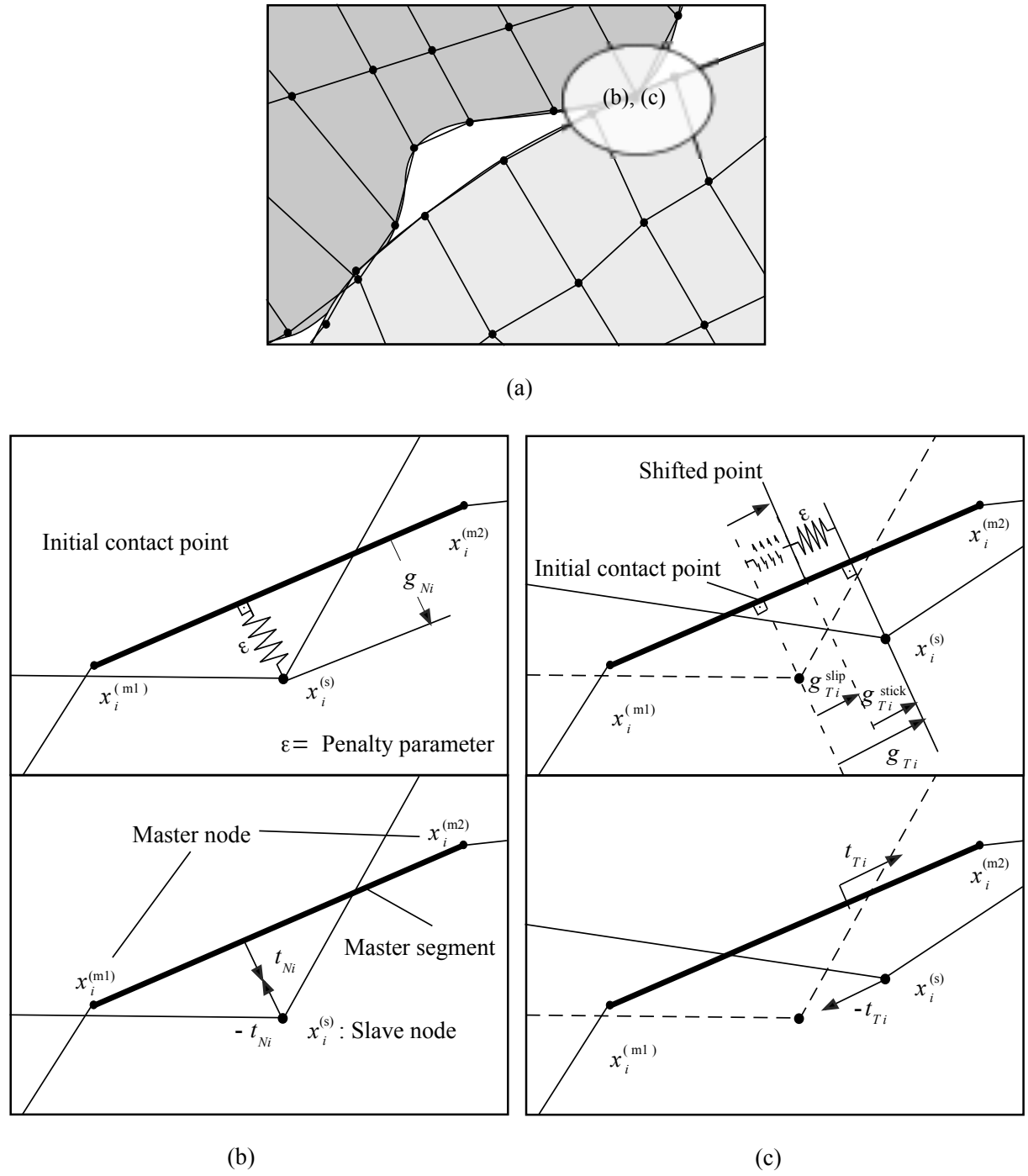

Figure 2.2: Schematic view of NTS contact elements with the penalty method. (a) Contact interfaces formed between two finite element meshes, (b) expression of normal contact, and (c) model of stick-slip phenomenon in terms of the NTS approach.

This section provides the standard contact algorithm based on the penalty method (Wriggers, 2001; Liu et al., 2006) and an implementation of the friction and the cohesion. For solving the discretized equations (Eq. (2.3)), the Newton's method is utilized since the discretized equations have nonlinear relationships with the displacement (Wriggers et al., 2001; Liu et al. 2003; Wriggers, 2006). From Eq. (2.3), the linearized equation is expressed by

$$\begin{aligned}\delta W + \frac{\partial(\delta W)}{\partial u_i}\Delta u_i = &\sum_{A=1}^{ne}\sum_{B=1}^{ne}\delta {u_i}^{d(A)}\left({R_i}^{d(A)} + \left[{K_{ij}}^{d(AB)}\right]\Delta {u_i}^{d(B)}\right) \\ &+ \sum_{C=1}^{nc}\sum_{D=1}^{ne}\delta {u_i}^{c(C)}\left({R_i}^{c(C)} + \left[{K_{ij}}^{c(CD)}\right]\Delta {u_i}^{c(D)}\right),\end{aligned} \tag{2.4}$$

in which Δu_i denotes the displacement increments, u_i is the global displacement vector, $\left[{K_{ij}}^{d(AB)}\right]$ is the stiffness matrix of each finite elements, $\left[{K_{ij}}^{c(CD)}\right]$ is the stiffness matrix of contact elements. As the NTS elements share the nodes with the finite elements as seen in Fig. 2.2, Eq. (2.4) can be assembled into a system of equation

$$\left[K_{\alpha\beta}\right]\Delta u_\beta = -R_\alpha \tag{2.5}$$

$$\left[K_{\alpha\beta}\right] = \cup\langle\left[{K_{ij}}^{d(AB)}\right], \left[{K_{ij}}^{c(CD)}\right]\rangle \tag{2.6}$$

$$R_\alpha = \cup\langle {R_i}^{d(A)}, {R_i}^{c(C)}\rangle \tag{2.7}$$

where $\left[K_{\alpha\beta}\right]$ is the global stiffness matrix, R_α is the global residual vector, and $\cup\langle\cdot,\cdot\rangle$ is the matrix-vector assembly operator, which rearrange a matrix form into a vector form. In every iteration in the Newton's method, the displacement fields are updated by using the solution of Eqs. (2.5), (2.6), and (2.7).

For the sake of stability of the solution algorithm, there are two phases during every time step, which are the first and the second the Newton's loop (Wriggers, 2006). The first Newton's loop is in the trial mode, in which the frictional stress assumed to be proportional to the displacement without any plastic slip. After the convergence, the frictional law is enforced in the second phase, where displacement and frictional stress are updated at every iteration until equilibrium is achieved.

In order to update frictional stress (Fig. 2.2), the return-mapping algorithm is employed. The algorithm is originally proposed by Simo and Taylor (1986) for updating stress in the framework of the elasto-plasticity. The idea has been extended in terms of the CCM as an algorithm for updating the frictional stress (Peric and Owen, 1992; Wriggers et al., 2001). Although the scheme generally is solved by iterative methods, it can be directly solved in case of the Mohr-Coulomb's model,

$$f = \sqrt{t_{Ti} t_{Ti}} - \mu \cdot \epsilon \sqrt{g_{Ni} g_{Ni}} - c \geq 0 \tag{2.8}$$

where f is the yield function, μ is the frictional coefficient and c is the cohesion. The system of equations is given by,

$$t_{Ti}^{n+1} = \epsilon \left(g_{Ti}^{n+1} - \mathbf{g}_{Ti}^{slip,n+1} \right) (f > 0) \tag{2.9}$$

$$t_{Ti}^{n+1} = \left(\mu \sqrt{t_{Ni}^{n+1} t_{Ni}^{n+1}} + c \right) \frac{t_{Ti}^{tr,n+1}}{\sqrt{t_{Ti}^{tr,n+1} t_{Ti}^{tr,n+1}}} \tag{2.10}$$

$$g_{Ti}^{slip,n+1} = g_{Ti}^{slip,n} \, (f < 0) \tag{2.11}$$

$$g_{Ti}^{slip,n+1} = g_{Ti}^{slip,n} + \frac{\left(\sqrt{t_{Ti}^{n+1} t_{Ti}^{n+1}} - \mu \cdot \sqrt{t_{Ni}^{n+1} t_{Ni}^{n+1}} - c \right)}{\epsilon} \cdot \frac{t_{Ti}^{tr,n+1}}{\sqrt{t_{Ti}^{tr,n+1} t_{Ti}^{tr,n+1}}} \, (f \geq 0) \tag{2.12}$$

where $t_{Ti}^{tr,n+1}$ is the frictional trial stress, and these equations are used in the solution algorithm.

In this thesis, a simple modification is proposed for the pairing algorithm of the NTS element, which is explained in detail in Chapter 4. One of the main issues in the NTS formulation is that the pairing between a node and a segment is not unique in some cases (Wriggers, 2006; Zavarise and De Lorenzis, 2009). For instance, there are two possible master segments for single slave node. This phenomenon causes oscillations of the solution and the ill-convergence problem (Zavarise and De Lorenzis, 2009). Extensive research has shown that the problem is avoided by introducing a smooth surface in interfaces. Wriggers et al. (2001) have proposed some interpolations by using the Hermite functions and the cubic Bernstein functions. A more straightforward method has been proposed by Liu et al. (2003). However, these approaches are far more complicated than the original NTS approach due to the nonlinearity of the interpolations. Therefore, in this thesis, a simple algorithm is provided to avoid this problem, as illustrated in Chapter 4, and it is illustrated that the algorithm increases the robustness.

2.2.2 Formulations of root and soil

This section presents the discretization of domains, where two following points are discussed based on the NTS approach. First, the virtual work should be formulated in terms of the current configuration since the momentum balance can be formulated only at the current configuration, and not in the initial configuration within contact problems (Wriggers, 2006). Also, a constitutive equation used in the formulation should satisfy objectivity for rotation. The reason for it is that the frictional contact problem, as presented here, is large-deformation or large-slip problems where domains significantly rotate. A formulation is based on the finite strain theory with the multiplicative decomposition of the deformation gradient tensor to satisfy the objectivity.

The finite strain theory is derived from the momentum balance in the current configuration,

$$\frac{\partial \sigma_{ij}}{\partial x_j} + \rho b_i = \rho \dot{v}_i \tag{2.13}$$

where σ_{ij} is the Cauchy stress tensor, v_i the velocity and $\dot{v}_i$ the acceleration, b_i is the body force, ρ is the bulk density, x_j is the coordinate in terms of current configuration. Eq. (2.13) is solved with Dirichlet boundary condition (displacement boundary)

$$u_i = \bar{u_i} \quad \text{on} \quad \Gamma_u, \tag{2.14}$$

Neumann boundary condition (traction boundary condition)

$$\sigma_{ij} n_j = \bar{t_i} \quad \text{on} \quad \Gamma_t, \tag{2.15}$$

and initial conditions

$$u_i = \bar{u_i} \quad \text{on} \quad t = 0, \tag{2.16}$$

$$\sigma_{ij} = \bar{\sigma_{ij}} \quad \text{on} \quad t = 0, \tag{2.17}$$

where Γ_u is the Dirichlet boundary and $\bar{u_i}$ is the displacement on the boundary, Γ_t is the Neumann boundary and $\bar{t_i}$ is the traction on the boundary, n_j is the normal vector on the boundary, $\bar{u_i}$ and $\bar{\sigma_{ij}}$ are initial values. Consequently, the integral form of Eq. (2.13) is

$$\int_\Omega \frac{\partial \sigma_{ij}}{\partial x_j} d\Omega + \int_\Omega \rho b_i d\Omega = \int_\Omega \rho \dot{v}_i d\Omega \tag{2.18}$$

In case of the formulation based on finite strain theory, Eq. (2.13) and above initial/boundary conditions are pulled back to the initial configuration for convenience. Among the various pull-back operations, following pull-back operation is often used,

$$P_{iJ} = \tau_{ik} F^{-T}_{kJ} = J \sigma_{ij} F^{-T}_{kJ} \tag{2.19}$$

where τ_{ik} is the Kirchhoff stress tensor, P_{iJ} is the first Piola-Kirchhoff stress tensor, F_{iJ} is the deformation gradient tensor which is the two-point tensor and explained in detail in the next section,

$$F_{iJ} = \frac{\partial x_i}{\partial X_J} \tag{2.20}$$

where X_J is the coordinate of initial configuration and J is

$$J = \epsilon_{IJK} F_{1I} F_{2J} F_{3K} \tag{2.21}$$

where ϵ_{IJK} is the Levi Civita symbol.

Based on this pull-back operation, an area is pulled-back as

$$\sigma_{ij} d\Gamma = \frac{\tau_{ik}}{J} F_{kJ}^{-T} N_J J d\bar{\Gamma} = P_{iJ} N_J d\bar{\Gamma} \tag{2.22}$$

where N_J is the normal vector on the initial configuration. From the relationships, the integral form of the Eq. (2.13) is pulled back by using the relationship of Eq. (2.19) as

$$\int_{\bar{\Omega}} \frac{\partial P_{iJ}}{\partial X_J} d\bar{\Omega} + \int_{\bar{\Omega}} \rho_0 b_i d\bar{\Omega} - \int_{\Omega} \rho_0 \dot{v}_i d\bar{\Omega} = 0 \tag{2.23}$$

where $\bar{\Omega}$ and $\bar{\Gamma}$ are the domain and the surface in terms of the initial configuration, respectively, and ρ_0 is the density with respect to the initial configuration. Taking the weak derivative of the equation, the weak form is obtained.

$$\begin{aligned} \delta W^d &= \int_{\bar{\Omega}} \frac{\partial P_{iJ}}{\partial X_J} \delta u_i d\bar{\Omega} + \int_{\bar{\Omega}} \rho_0 b_i d\delta u_i \bar{\Omega} - \int_{\Omega} \rho_0 \dot{v}_i \delta u_i d\bar{\Omega} \\ &= \int_{\bar{\Omega}} P_{iJ} \frac{\partial \delta u_i}{\partial X_J} d\bar{\Omega} + \int_{\bar{\Omega}} \rho_0 b_i d\delta u_i \bar{\Omega} - \int_{\Omega} \rho_0 \dot{v}_i \delta u_i d\bar{\Omega} - \int_{\bar{\Gamma}} \bar{t}_i \delta u_i d\bar{\Gamma} \\ &= 0 \end{aligned} \tag{2.24}$$

where δW^d is the virtual work of domains.

Since Eq. (2.24) is a system of nonlinear equations, it is solved by the Newton's method. The linearized equation is analytically computed by taking the directional derivative of δW for displacement field u in terms of the initial configuration. The linearized equation is given below. The first term of the right-hand side part is discretized by following mathematical operations. First, let us linearize the Eq. (2.24).

$$\frac{\partial \delta W^d}{\partial X_I} \Delta u_I = \frac{\partial}{\partial X_I} \int_{\bar{\Omega}} P_{iJ} \frac{\partial \delta u_i}{\partial X_J} d\bar{\Omega} \Delta u_I \tag{2.25}$$

Here, the first Piola-Kirchhoff stress tensor has the relationship of $P_{iJ} = F_{iK} S_{KJ}$. Substituting this to the Eq. (2.26),

$$\frac{\partial \delta W^d}{\partial X_I}\Delta u_I = \int_{\bar{\Omega}} \frac{\partial F_{iK} S_{KJ}}{\partial X_I}\Delta u_I \frac{\partial \delta u_i}{\partial X_J} d\bar{\Omega} \tag{2.26}$$

noting that the directional derivative is decomposed as

$$\frac{\partial F_{iK} S_{KJ}}{\partial X_I}\Delta u_I = \frac{\partial F_{iK}}{\partial X_I} S_{KJ}\Delta u_I + F_{iK}\frac{\partial S_{KJ}}{\partial X_I}\Delta u_I \tag{2.27}$$

with

$$\frac{\partial F_{iK}}{\partial X_I} S_{KJ}\Delta u_I = \frac{\partial \Delta u_I}{\partial X_J} S_{KJ}, \tag{2.28}$$

and

$$F_{iK}\frac{\partial S_{KJ}}{\partial X_I}\Delta u_I \delta u_i \partial X_J = \delta E_{IJ} C_{IJKL} \Delta E_{KL}. \tag{2.29}$$

Substituting Eqs (2.27) to (2.29) into Eq. (2.26), Eq. (2.30) is obtained.

$$\frac{\partial \delta W^d}{\partial X_I}\Delta u_I = \int_{\bar{\Omega}} \left(\frac{\partial \Delta u_I}{\partial X_J} S_{JK} \frac{\partial \delta u_I}{\partial X_K} + \delta E_{IJ} C_{IJKL} \Delta E_{KL} \right) d\bar{\Omega} \tag{2.30}$$

where C_{IJKL} is the algorithmic stiffness matrix in terms of reference configuration since the contact can only be described with respect to the current configuration. Eq. (2.30) is pushed-forward to the current configuration.

$$\frac{\partial \delta W^d}{\partial X_I}\Delta u_I = \int_{\Omega} \left(\frac{\partial \Delta u_i}{\partial x_j} \sigma_{jk} \frac{\partial \delta u_i}{\partial x_k} + \delta d_{ij} \bar{c}_{ijkl} \Delta d_{kl} \right) d\Omega \tag{2.31}$$

where $\bar{c}_{ijkl}$ is the stiffness matrix with respect to the current configuration,

$$\bar{c}_{ijkl} = \frac{1}{J} F_{iI} F_{jJ} F_{kK} F_{lL} \bar{C}_{IJKL} \tag{2.32}$$

Eq. (2.31) is discretized based on Galerkin's method, thereby, the stiffness matrix $K^{d(IJ)}$ of Eq. (2.4) is obtained.

$$K^{d(IJ)} = K_1^{d(IJ)} + K_2^{d(IJ)} \tag{2.33}$$

where $K_1^{d(IJ)}$ and $K_2^{d(IJ)}$ are

$$K_1^{d(IJ)} = \int_{\Omega_e} \frac{\partial N_I}{\partial x_k} \tau_{kl} \frac{\partial N_J}{\partial x_l} d\Omega_e \tag{2.34}$$

$$K_2^{d(IJ)} = \int_{\Omega_e} B_{Ik} D_{kl} B_{lJ} d\Omega_e \tag{2.35}$$

since the Eq. (2.36) is discretized as below.

$$\frac{\partial \delta W^d}{\partial X_I}\Delta u_I = \int_{\Omega_e} \left(\delta u_I \frac{\partial N_I}{\partial x_k} \tau_{kl} \frac{\partial N_J}{\partial x_l} \Delta u_J + \delta u_I B_{Ik} D_{kl} B_{lJ} \Delta u_J \right) d\Omega_e \tag{2.36}$$

2.2.3 Solution algorithm

This subsection discusses the solution algorithm for root-soil contact simulations. As discussed in the last subsection, the system of equations is nonlinear with respect to the displacement field. Consequently, iterative solver such as the Newton's method is to be employed, where the trial variables of displacement and internal variables (e.g., stress measure, strain measure, and softening/hardening parameters) are updated so that the final solution satisfies the virtual work equation (Eq. (2.24)) and the yield criterions of domains and interfaces. The solution algorithm also updates the pairing of contact elements (Fig. 2.2) within the iterative loops of the Newton's method; this pairings algorithm is also explained in the current subsection.

Chapters 4 and 5 show solution algorithms for friction-cohesion contact problems. The algorithm consists of two parts: a stick part and a slip part. In the stick part, all contact elements are under elastic stick conditions, which indicates no slip is allowed in the interfaces. The stress, internal variables, and displacements are computed as trial values, which are used as the initial trial value of the second part. The second part, afterward, updates the frictional stress where the slip is allowed. The scheme mentioned above is a widely-used technique to reduce the instability of the iterative method, as shown in Wriggers (2006). In each part, the pairing is detected firstly, and then the stiffness matrix and residuals are computed for every solid and contact elements. Then some linear solver is utilized to solve the system of discretized equations, for instance, the iterative method as the Conjugate Gradient (CG) method or direct solver such as the Gauss-Jordan method.

The configurations of domains and contact interfaces are updated based on the stress-updating methods, as seen in the previous subsections. The stress, plastic strain measure, and hardening/softening parameters are updated based on elasto-plasticity, and the shear stress of root-soil interfaces is updated by the stress-updating scheme discussed in Eq. (2.12).

2.3 Constitutive model and material tests of root and soil domains

This section discusses material tests and modeling of the root matrix in terms of continuum mechanics and CCM. The present model based on the CCM necessitates some parameters to solve the system of equations. The parameters are roughly categorized into the material parameters for root domains, soil domains, and ones of root-soil interfaces. This section discusses the physical tests and models for domains of roots and soils, and the next section describes that for root-soil interfaces. The material tests of roots are not standardized; therefore, this section proposes a possible simplest method and an apparatus to measure the stiffness parameters of roots. As for the material tests of soils, there have been many meth-

ods to determine the stiffness parameters, and the method is standardized by, for instance, the JIS and the JGS. Thereby the present section introduces some of the testing methods to measure the stiffness parameters of soils from the standardized methods. The constitutive models for roots and soils are also to be discussed. For these reasons, the current section utilizes some consistent models for roots and soils.

This section firstly provides a summary of the finite strain theory for general cases which include both elastic and plastic behaviors. From the standpoint of finite strain theory, the constitutive model is given as an elastic/plastic potential function; consequently, this section also suggests the possible simplest models of both potential functions.

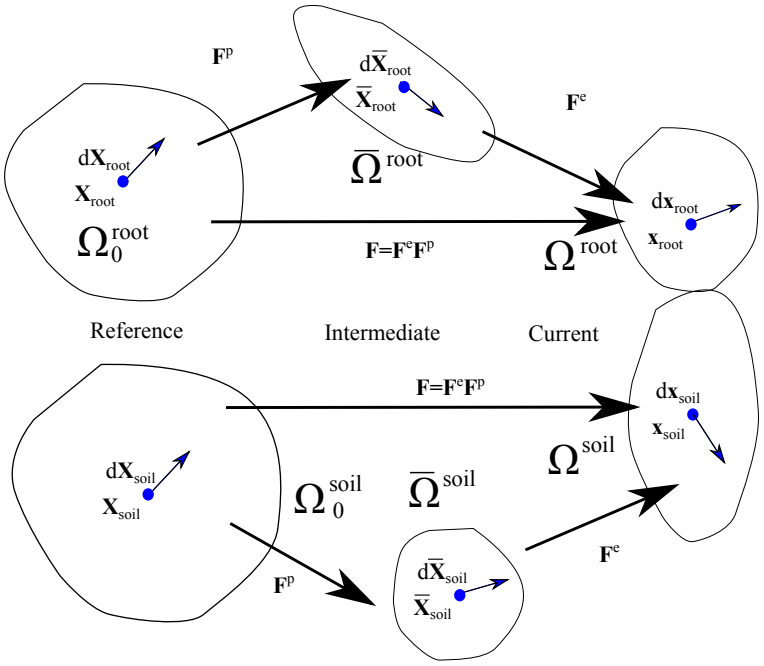

Figure 2.3: Schematic view of kinematics of two elasto-plastic bodies and the kinematic measures.

The contact kinematics with the finite strain theory is shown in Fig. 2.3, whereas the reference configurations Ω_0^{root}, Ω_0^{soil}, and the current configurations Ω^{root}, Ω^{soil} indicate the initial and present control volumes, respectively. Hereby the intermediate configurations $\bar{\Omega}^{root}$, $\bar{\Omega}^{soil}$ are also introduced to describe the virtual stress-free configuration. It is worth noting that the stress-free configuration is purely virtual and not uniquely observed in realistic situations and introduced just for convenience. Thanks to the stress-free intermediate configurations, the constitutive models of elastic/plastic parts are simply expressed as below by using elastic/plastic potential functions, respectively. Under these assumptions, let us project a small vector around a material point in terms of the reference configuration, which is denoted as dX_I into the intermediate/current configurations as shown in the figure, where the superscript ^{root} and ^{soil} denote the amounts of the roots and soils, respectively; the projections are visible as $d\bar{X}_I$ and dx_i. Further, the deformation gradient tensor is intro-

duced as follows;

$$dx_i = \frac{\partial x_i}{\partial X_J} dX_J = F_{iJ} dX_J \tag{2.37}$$

$$dx_i = \frac{\partial x_i}{\partial \bar{X}_{\bar{J}}} d\bar{X}_{\bar{J}} = F_{i\bar{J}}{}^{e} d\bar{X}_{\bar{J}} \tag{2.38}$$

$$d\bar{X}_{\bar{I}} = \frac{\partial \bar{X}_{\bar{J}}}{\partial X_J} dX_J = F_{\bar{I}J}{}^{p} dX_J \tag{2.39}$$

where F_{iJ} is the deformation gradient tensor, $F_{i\bar{J}}{}^{e}$ is the elastic deformation gradient tensor, and $F_{\bar{I}J}{}^{p}$ is the plastic deformation gradient tensor (e.g. Hashiguchi and Yamakawa, 2013). Hence, the three deformation gradient tensors has a relationship of Eq. (2.40)

$$F_{iJ} = \frac{\partial x_i}{\partial X_J} = \frac{\partial x_i}{\partial \bar{X}_{\bar{I}}} \frac{\partial \bar{X}_{\bar{I}}}{\partial X_J} = F_{i\bar{I}}{}^{e} F_{\bar{I}J}{}^{p}. \tag{2.40}$$

As well as vectors, areas and volumes are projected and the mathematical expression of the projections are also given by using deformation gradient tensors. First, areas are projected by

$$da_i = n_i da = J F_{iJ}{}^{-T} N_J dA = J F_{iJ}{}^{-T} dA_J \tag{2.41}$$

where n_i and N_J are the outer normals with respect to the infinitesimal area, which is called the Nanson's formula. The analogous of the Nanson's formula is also given for other two projections for elastic and plastic deformation gradient tensors.

$$da_i = n_i da = J^e F_{i\bar{I}}{}^{e-T} \bar{N}_{\bar{I}} d\bar{A} = J F_{i\bar{I}}{}^{e-T} d\bar{A}_{\bar{I}} \tag{2.42}$$

$$d\bar{A}_{\bar{I}} = \bar{N}_{\bar{I}} d\bar{A} = J^p F_{\bar{I}J}^{p-T} N_J dA = J^p F_{\bar{I}J}{}^{p-T} dA_J, \tag{2.43}$$

where da_i, $d\bar{A}_{\bar{I}}$, and $d\bar{A}_I$ are the area vectors on the current, the intermediate, and the initial configuration, respectively. $\bar{N}_{\bar{I}}$ is the normal vector on the area in the intermediate configuration. The projection of the volumes are described as below.

$$dv = JdV = J^e d\bar{V} = J^e J^p dV \tag{2.44}$$

where $J^e = \epsilon_{I\bar{J}K} F_{\bar{I}}{}^{e} F_{\bar{J}}{}^{e} F_{\bar{K}}{}^{e}$, and $J^p = \epsilon_{IJK} F_I{}^{p} F_J{}^{p} F_K{}^{p}$

The elastic constitutive equations are provided by using the elastic deformation gradient tensor $F_{i\bar{I}}{}^{e}$ and decoupled from the plastic deformation gradient tensor $F_{\bar{I}J}{}^{p}$. Before describing the elastic potential function and constitutive models of roots and soils, both

strain and stress measures are to be defined. Here are the strain measures which is directly computed by using these deformation gradient tensors.

$$C_{IJ} = {F_{Ii}}^T F_{iJ} \tag{2.45}$$

$$C_{\bar{I}\bar{J}}{}^e = {F_{\bar{I}I}}^{eT} F_{I\bar{J}}{}^e \tag{2.46}$$

$$C_{IJ}{}^p = F_{I\bar{I}}{}^{pT} {F_{\bar{I}J}}^p \tag{2.47}$$

where C_{IJ} is called right Cauchy-Green tensor, $C_{\bar{I}\bar{J}}{}^e$ is called elastic right Cauchy-Green tensor, and $C_{IJ}{}^p$ is called plastic right Cauchy-Green tensor. It is worth noting that the elastic right Cauchy-Green tensor $C_{\bar{I}\bar{J}}{}^e$ is defined in the intermediate configuration and the others are defined in the reference configuration. Since the elastic right Cauchy-Green tensor is defined in the intermediate configuration, the elastic potential energy and constitutive models are defined in the intermediate configuration. Further, material-time derivative of the strain measures are necessary for the time-integration of the plastic strain measure, for instance, $C_{IJ}{}^p$, which is given as analogy of the velocity gradient tensor l_{ij},

$$l_{ij} = \frac{\partial v_i}{\partial x_j} = F_{iK} {F_{Kj}}^{-1} \tag{2.48}$$

and given as

$$\bar{L}^p_{\bar{I}\bar{J}} = F^p_{\bar{I}k} F^{p-1}_{k\bar{J}} \tag{2.49}$$

where $\bar{L}^p_{\bar{I}\bar{J}}$ is the plastic velocity gradient tensor. The symmetric part of this tensor is utilized for plastic flow rule.

$$\bar{D}^p_{\bar{I}\bar{J}} = \bar{L}^p_{\bar{I}\bar{J}} + L_{\bar{I}\bar{J}}{}^{pT} \tag{2.50}$$

where $\bar{D}^p_{\bar{I}\bar{J}}$ is the plastic stretch tensor.

The work-conjugate stress tensor of the elastic right Cauchy-Green tensor is the Mandel stress tensor, which is given by push-forward of the second Piola-Kirchhoff stress tensor from the initial configuration to the intermediate configuration and pull-back of the Kirchhoff stress tensor $\tau_{ij} = J\sigma_{ij}$ from the current configuration to the intermediate configuration.

$$\bar{M}_{\bar{I}\bar{J}} = {F_{\bar{I}K}}^{p-T} C_{KL} S_{LM} F_{M\bar{J}}{}^{pT} = {F_{\bar{I}k}}^{eT} \tau_{kl} F_{l\bar{J}}{}^{e-T} \tag{2.51}$$

noting following work-conjugacy.

$$\tau_{ij} : l_{ij} = \bar{M}_{\bar{I}\bar{J}} : \bar{L}_{\bar{I}\bar{J}} \tag{2.52}$$

Finally, elastic potential functions W, which is equivalent to the Gibbs free energy, are given as function of elastic right Cauchy-Green tensor and satisfy the following relationships.

$$\bar{M}_{\bar{I}\bar{J}} = 2\bar{C}^{e}_{\bar{I}\bar{K}} \frac{\partial W}{\partial \bar{C}^{e}_{\bar{I}\bar{J}}} \tag{2.53}$$

On the other hand, plastic potential functions and yield functions are defined in terms of Mandel stress tensor $\bar{M}_{\bar{I}\bar{J}}$. For instance, soil constitutive models often utilizes the Drucker-Prager model or Mohr-Coulomb model as their plastic potential function and/or yield functions (Wu et al., 2017): Both models are modeled in Eqs. (2.54) and (2.55).

$$f\left(\bar{M}\right)^{Drucker-Prager} = \sqrt{(J_2^{\bar{M}})} + \frac{B_c - 1}{\sqrt{3}B_c + 2\sqrt{3}} I_1^{\bar{M}} - \frac{\sqrt{3}}{B_c + 2} f_c \tag{2.54}$$

$$f\left(\bar{M}\right)^{Mohr-Coulomb} = \sqrt{(J_2^{\bar{M}})} + \frac{\left(B_c - 1\right) I_1^{\bar{M}} - 3f_c}{3\left(B_c + 1\right)\cos\theta^{\bar{M}} + \sqrt{3}\left(B_c - 1\right)\sin\theta^{\bar{M}}} \tag{2.55}$$

where $I_1^{\bar{M}}$, $J_2^{\bar{M}}$, and $\theta^{\bar{M}}$ are the first invariant of the Mandel stress tensor, the second invariant of the deviatoric part of the Mandel stress tensor, and the Lode angle in terms of Mandel stress tensor, respectively. B_c and f_c is computed as below.

$$B_c = \frac{1 + sin\phi}{1 - sin\phi}, \tag{2.56}$$

where c is the cohesion of soils.

$$f_c = \frac{2ccos\phi}{1 + sin\phi}. \tag{2.57}$$

The Cauchy stress tensor is often utilized instead of the Mandel stress tensor in case of infinitesimal strain theory. It is worth noting that there is a simple relationship between these invariants of Mandel stress and the Cauchy stress tensors, as seen below. First, the first invariant of the Mandel stress tensor has a relationship of

$$I_1^{\bar{M}} = \bar{M}_{\bar{I}\bar{I}} = JF^{eT}_{\bar{I}i}\sigma_{ij}F^{e-T}_{j\bar{I}} = J\delta_{ji}\sigma_{ij} = J\sigma_{ii} = JI_1^{\sigma}, \tag{2.58}$$

and the second invariant has a relationship of

$$J_2^{\bar{M}} = \frac{1}{2}\left(\bar{M}_{\bar{I}\bar{J}}\bar{M}_{\bar{I}\bar{J}}\right) = J^2 J_2^{\sigma}. \tag{2.59}$$

Further, the Lode angle of the Mandel stress is the same as the one of the Cauchy stress tensor.

$$\theta^{\bar{M}} = \frac{1}{3}sin^{-1}\left(-\frac{3\sqrt{3}}{2}\frac{J_3^{\bar{M}}}{\left(J_2^{\bar{M}}\right)^{\frac{3}{2}}}\right) = \frac{1}{3}sin^{-1}\left(-\frac{3\sqrt{3}}{2}\frac{J_3^{\sigma}}{(J_2^{\sigma})^{\frac{3}{2}}}\right) = \theta^{\sigma} \tag{2.60}$$

where the third invariants of the deviatoric stress tensor $\bar{M}^{'}_{\bar{I}\bar{J}}$ is defined as seen.

$$J_3^{\bar{M}} = \frac{1}{3}\bar{M}^{'}_{\bar{I}\bar{K}}\bar{M}^{'}_{\bar{K}\bar{L}}\bar{M}^{'}_{\bar{L}\bar{I}} = J^3 J_3^{\sigma}. \tag{2.61}$$

where the deviatoric stress tensor is defined as

$$\bar{M}^{'}_{\bar{I}\bar{J}} = \bar{M}_{\bar{I}\bar{J}} - \frac{1}{\bar{M}_{\bar{K}\bar{K}}}\delta_{\bar{I}\bar{J}} \tag{2.62}$$

These indicates that the stress invariants are identical with respect to the rotation and only depends upon the volumetric change; this fact is consistent with the definition of the stress invariants. The plastic strain measure, C^p_{IJ} is updated by integrating the increments $\dot{C}^p_{IJ}$ which is computed by flow rule. The flow rule is also described in terms of the intermediate configuration.

$$\bar{D}^p_{\bar{I}\bar{J}} = \Delta\lambda \left(\sqrt{\frac{\partial f}{\partial \bar{M}_{\bar{K}\bar{L}}}\frac{\partial f}{\partial \bar{M}_{\bar{K}\bar{L}}}} \right)^{-1} \frac{\partial f}{\partial \bar{M}_{\bar{I}\bar{J}}} \tag{2.63}$$

$$\dot{C}^p_{IJ} = 2F^{pT}_{I\bar{K}}\bar{D}^p_{\bar{K}\bar{L}}F^p_{\bar{L}J} = \Xi_{IK}C^p_{KJ}, \tag{2.64}$$

here, a operator Ξ_{IK} is

$$\Xi_{IK} = 2\Delta\lambda \left(\sqrt{\frac{\partial f}{\partial \bar{M}_{\bar{K}\bar{L}}}\frac{\partial f}{\partial \bar{M}_{\bar{K}\bar{L}}}} \right)^{-1} F^{pT}_{I\bar{K}}\frac{\partial f}{\partial \bar{M}_{\bar{K}\bar{L}}}F^{p-T}_{\bar{L}K}. \tag{2.65}$$

The plastic strain measure is integrated by using time-integration scheme such as backward-Euler method; the algorithm to compute this time-integration is called the Return-Mapping (RM) method. Here is a general expression of the RM method.

$$Y_{\mu 1} = C^p_{n+1,\mu} - \Delta t \Xi_{\mu\nu} C^{np}_{\ \nu} = 0 \tag{2.66}$$

$$Y_2 = f^{n+1} = 0 \tag{2.67}$$

where $C^{n+1p}_{\ \mu}$ and $C^{np}_{\ \nu}$ are the plastic right Cauchy-Green tensors in terms of the time-step $n+1$ and n, respectively. $f^{\bar{M}}_{n+1}$ is a yield function with respect to the Mandel stress tensor. The system of non-linear equations are solved by using the Newton's method.

$$Y^{total,k}_{\mu} = \left(Y^{1,k}_{11}, Y^{1,k}_{12}, \cdots, Y^{1,k}_{33}, Y_{2,k} \right)^T = 0 \tag{2.68}$$

$$X^{total,k}_{\mu} = \left(C^{pn+1,k}_{\ 11}, C^{pn+1,k}_{\ 12}, \cdots, C^{pn+1,k}_{\ 33}, \delta\lambda_k \right)^T \tag{2.69}$$

$$X^{total,k+1}_{\mu} = X^{total,k}_{\mu} - J^{-1}_{\mu\nu} Y^{total,k}_{\nu} \tag{2.70}$$

where the matrix $J_{\mu\nu}$ is the Jacobian matrix which is updated in every stress-update process in the global solution algorithm. Following subsections present the concrete formulations.

2.3.1 Constitutive model for root domain

This subsection proposes constitutive models for root domains based on the finite strain theory. In order to determine the constitutive model, bending tests are conducted by utilizing two types of plant roots, which are soybean and barley roots. The results are described in the next subsection, where the material mostly behaves as elastic bodies. Consequently, this subsection utilizes a perfectly elastic model by enforcing a constraint condition,

$$C^{p}_{IJ} = \delta_{IJ} \tag{2.71}$$

where, δ_{IJ} is the identity matrix, which indicates that no plastic strain is computed during simulations. It is worth noting that this assumption sustains only when the loading stress is smaller than the failure stress of the root tissues.

This section utilizes the Neo-Hookean elastic potential function for root material, which has been utilized for living bio-material such as cell-wall (Huang et al., 2012). As mentioned in the previous subsection, the finite strain theory necessitates an elastic potential function to provide constitutive relationships for a material. The elastic potential function should be chosen so that the stress-strain relationship of material is accurately reproduced. This thesis utilizes the Neo-Hookean elastic potential function since it has been employed to express stress-strain relationships of plant bodies (Huang et al., 2012). The elastic potential function is visible in Eqs. (2.73) and (2.74).

$$W = W_1 + W_2 \tag{2.72}$$

with

$$W_1 = \frac{\Lambda}{4}\left(\epsilon_{\bar{I}\bar{J}\bar{K}}\bar{C}^{e}_{\bar{1}\bar{I}}\bar{C}^{e}_{\bar{2}\bar{J}}\bar{C}^{e}_{\bar{3}\bar{K}} - 1 - 2\ln\sqrt{\epsilon_{\bar{I}\bar{J}\bar{K}}\bar{C}^{e}_{\bar{1}\bar{I}}\bar{C}^{e}_{\bar{2}\bar{J}}\bar{C}^{e}_{\bar{3}\bar{K}}}\right) \tag{2.73}$$

$$W_2 = \frac{\mu}{2}\left(\bar{C}^{e}_{\bar{K}\bar{K}} - 3 - 2\ln\sqrt{\epsilon_{\bar{I}\bar{J}\bar{K}}\bar{C}^{e}_{\bar{1}\bar{I}}\bar{C}^{e}_{\bar{2}\bar{J}}\bar{C}^{e}_{\bar{3}\bar{K}}}\right) \tag{2.74}$$

where Λ and μ are the first and second Lame constants, respectively.

2.3.2 Constitutive model for soil domain

This subsection discusses the constitutive models of soil domains. There have been developed numerous constitutive models of soils, and some of them have been utilized in terms of the finite strain theory, for instance, the Cam-clay model (Yamakawa et al., 2010). One of the simplest models of soils is a Mohr-Coulomb Drucker-Prager model, which utilizes the Mohr-Coulomb model as a yield function and Drucker-Prager model as a potential plastic function. Both models are visible in Eqs. (2.55) and (2.54), respectively. Both models also necessitate an elastic model, and hereby, the Neo-Hookean model is utilized since the

model is one of the possible simplest and the widely-used model for elastic behavior ob elasto-plastic models (Hashiguchi and Yamakawa, 2013). Here is the Jacobian matrix of the plastic potential function in terms of return-mapping algorithm.

$$J_{\mu\nu} = \alpha \left[\frac{1}{2} \left(M_{\mu\nu} - \frac{I_1^{\bar{M}}}{3} G_{\mu\nu} \right) + \frac{B_I - 1}{\sqrt{3}B_I + 2\sqrt{3}} G_{\mu\nu} \right] \tag{2.75}$$

where α is

$$\alpha = 4\Delta\lambda \left[M_{KL} : M_{KL} - \frac{\left(I_1^{\bar{M}} \right)^2}{3} + 3 \left(\frac{B_I - 1}{\sqrt{3}B_I + 2\sqrt{3}} \right)^2 \right] \tag{2.76}$$

2.3.3 Material test for root domain

The root matrix necessitates two elastic moduli; the first and the second Lame constant, which are measured by using a simple bending test. Fig. 2.4 illustrates a schematic of the bending test where a root is sampled from a straight-root of a soybean seedling, and set on a bending machine. Thereby the relationship between forces P and displacements u are obtained. From the relationship, Young's modulus is estimated. Further, the Poisson's ratio of 0.3 is utilized according to the previous study (Kim et al., 2008).

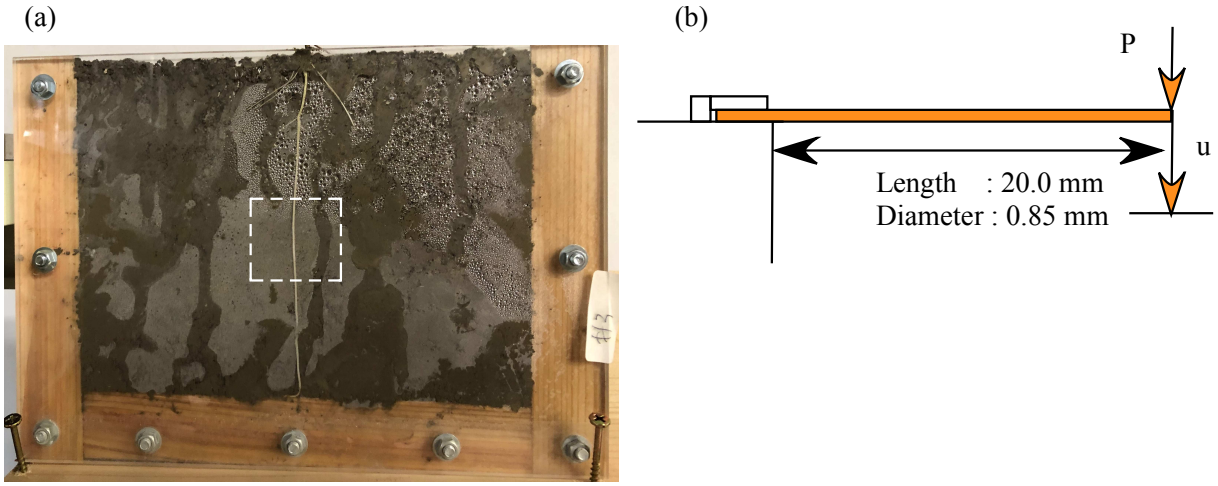

Figure 2.4: The bending test of a soybean root.

2.3.4 Material test for soil domain

This subsection discusses the material tests of soils to determine the parameters of elastic and plastic potential functions. There are two elastic parameters of soil in terms of the MC-DP model; Young's modulus and Poisson's ratio. Young's modulus is measured by using

unconfined compression (UC) tests (JGS-0511-2009), which has been used for measuring the Young's modulus-like E_{50} value. This test is conducted for cylinder-shaped specimens of soils, and the stiffness and yield stress under unconfined condition is measured. Since plant roots exist in the shallow, unconfined condition, the unconfined compression tests can realize similar stress conditions as the realistic conditions. Besides, the Poisson's ratio is measured by using a simple compression apparatus depicted in Fig. 2.5, which is similar to the conventional consolidation tests of clays. The presented apparatus loads the vertical pressure on the top of the soil specimen and measures horizontal soil pressure on the side of the specimen. From these results, the soil pressure coefficient is measured, as shown in the left graph of Fig. 2.5; the Poisson's ratio can be computed from the angle of the regression line.

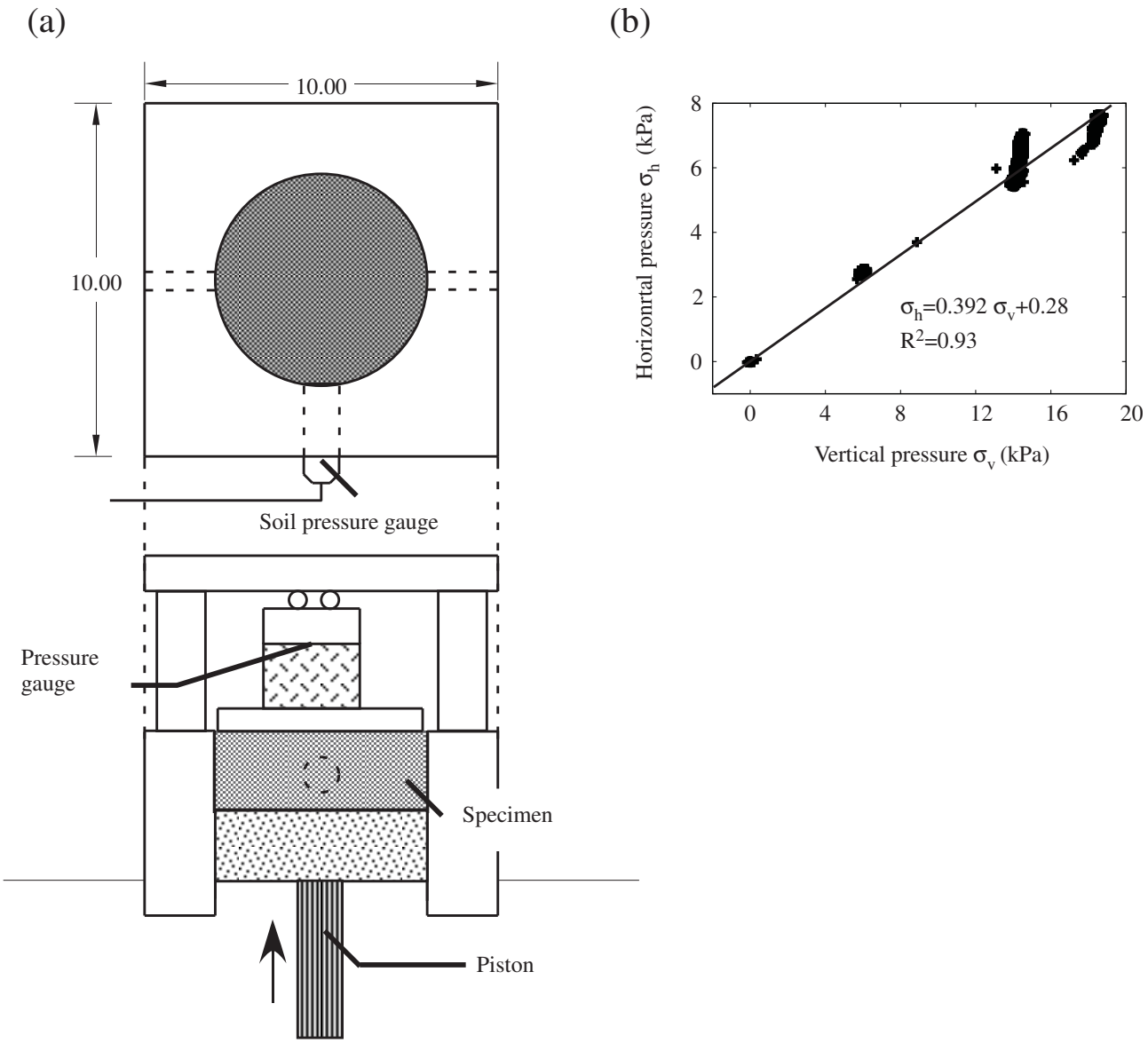

Figure 2.5: The Poisson's ratio test.

By contrast, there are three plastic parameters of the MC-DP model, the cohesion c, the frictional angle ϕ, and the dilatancy angle ψ. These parameters are usually measured by using the Direct Shear (DS) tests (JGS-0560-2009 and JGS-0561-2009) or Triaxial Compression (TC) tests (JGS-0521-2009, JGS-0522-2009, JGS-0523-2009, and JGS-0524-2009). The frictional angle ϕ is used for determining the MC model as a yield criterion, and the dilatancy angle ψ is utilized for plastic flow rule to compute the dilatancy effect; noting that the cohesion is utilized for both of yield function and plastic potential function. The material tests and the results are displayed in Chapters 4 and 5.

2.4 Material test and model of root-soil contact interface

This subsection briefly discusses the numerical model of root-soil interaction for the FE-analysis, which contains novel ideas and approaches, and the detail is presented in Chapters 4 and 6. As can be seen in Fig. 2.1, it is necessary to model the mechanical interaction of the root and soil domains to precisely predict the deformation of the root-soil system. There are two types of contact phenomena observed in generic contact interfaces: normal and tangential contact. The normal contact indicates the collision at the contact interface, the direction of which is identical to the outer normal vector of the contact interfaces. By contrast, the tangential contact is so-called shear, the direction of which is the same as the tangential vectors of the contact interfaces. It is worth noting that it is possible to define a set of the normal/tangential vectors if and only if the two domains are in contact. Otherwise, sets of normal/tangential vectors of possible contact surfaces are not identical. These two normal vectors are to be preliminarily identified before computing the above contact variables, which is essential for the existence and uniqueness of the solution.

By using the NTS approach, the normal contact and elastic stick of the tangential contact are automatically introduced. However, it should be given that the model and parameters of the slip rule of the tangential contact. The detail of the experiment is presented in Chapters 3, 4, and 5.

2.5 Summary

This chapter provides a continuum model for root-soil contact problems based on the finite strain theory and the CCM. The governing equations are derived from the momentum balance, elastic constitutive laws, and plastic flow rules in terms of the finite strain theory, which are essential for root-soil contact problems since both bodies undergo largely deformed processes and often rotate. The CCM is introduced to express root-soil contact interfaces, and the NTS approach is chosen since it is the possible simplest way to express contact, separation, friction, cohesion, and slip in the root-soil interfaces. The NTS ap-

proach is also capable of expressing complex root/soil morphologies, which is vital for the application to the practical problems such as numerical simulation of surface erosions in vegetated slopes and lodging of cereals. The concrete expression and material parameters of the root, soil, and root-soil interfaces are visible in the following chapters.

Chapter 3

Shear Test and Model of Root-Soil Contact Interface by Using Novel Pullout Test

3.1 Introduction

One of the significant difficulties of modeling rooted soils is due to the difficulty of predicting shear behavior of the root-soil interface. Mechanical behavior of rooted soils can be seen as contact problems of roots and soils. From this viewpoint, there are three domains to be modeled: soil domain, root domain, and root-soil interface. The mechanical behavior of soils has been a subject of soil mechanics, where various and reliable models are established in past decades, and some models are available for mechanical behavior of roots. However, few models are available for the shear strength of root-soil interfaces. Since the root-soil interface joints roots and soils, the shear strength of root-soil interfaces are to be modeled for full-understanding of rooted soils.

This chapter aims to measure and model the mechanical behavior of root-soil interfaces, where the mechanical behavior is consists of two characteristics: (1) the relationship between shear displacement and shear stress, and (2) the relationship between normal stress and shear strength. A novel pull-out apparatus is developed to measure the mechanical behavior of root-soil interfaces, which is presented in the next section. The next section also displays material properties and procedures of the pull-out tests. Tests are conducted preliminary for steel-sand interfaces and wood-sand interfaces for validation of both of the apparatus and procedures. Afterward, shear tests of root-soil interfaces are performed to evaluate the relationship between shear stress and displacement. Section 3 shows the results of the three pull-out tests, and the Mohr-Coulomb model models the mechanical behavior of the root-soil interfaces. Section 4 discusses the characteristics of the mechanical behavior of the root-soil interface and proposes continuum modeling based on the Computational Contact Mechanics (CCM). The verification of the model is also demonstrated in the section. Section 5 summarizes the chapter and remarks on the conclusion.

3.2 Shear test of root-soil contact interface

Several pull-out tests are proposed for different scopes, and the objectives are roughly categorized into two types. The first type of pull-out tests are conducted to measure the pull-out resistance of natural fibers such as roots (e.g., Abe and Zimmer, 1991); This type of studies present that the pull-out resistance of roots is closely related to the diameter. The Second type is applied for artificial fibers such as geo-membranes to evaluate the mechanical strength of reinforced soil (Kiyota et al., 2009). It is shown that the natural/artificial fibers increase the tensile strength of the mixtures. Further, this mechanism is directly observed by using microscopes (Hejazi et al., 2012). However, few studies are conducted to measure the shear strength of root-soil interfaces under realistic conditions. Hence, this section proposes a novel pull-out apparatus and the procedure.

3.2.1 Pull-out apparatus

Fig. 3.1 displays the outline of the pull-out apparatus. As can be seen in the center of the figure, a straight root is horizontally set on a steel soil-box (diameter is 6.0 cm, width is 2.0 cm) through a set of holes (diameter is 0.5 cm) and the soil is filled into the soil-box afterward. The weights vertically compress the specimen, and the root is pulled out to the left side of the figure, the speed of which is less than 0.1 mm/min so that it can be seen as a pseudo-static condition. The force gauge measures the reaction force, and the horizontal displacement is measured by displacement gauge attached on the left side of the force gauge. During the pull-out process, horizontal soil pressure is measured by using a soil pressure gauge attached in the side of the soil-box. The soil pressure is used for computing the mean normal stress of root-soil interfaces.

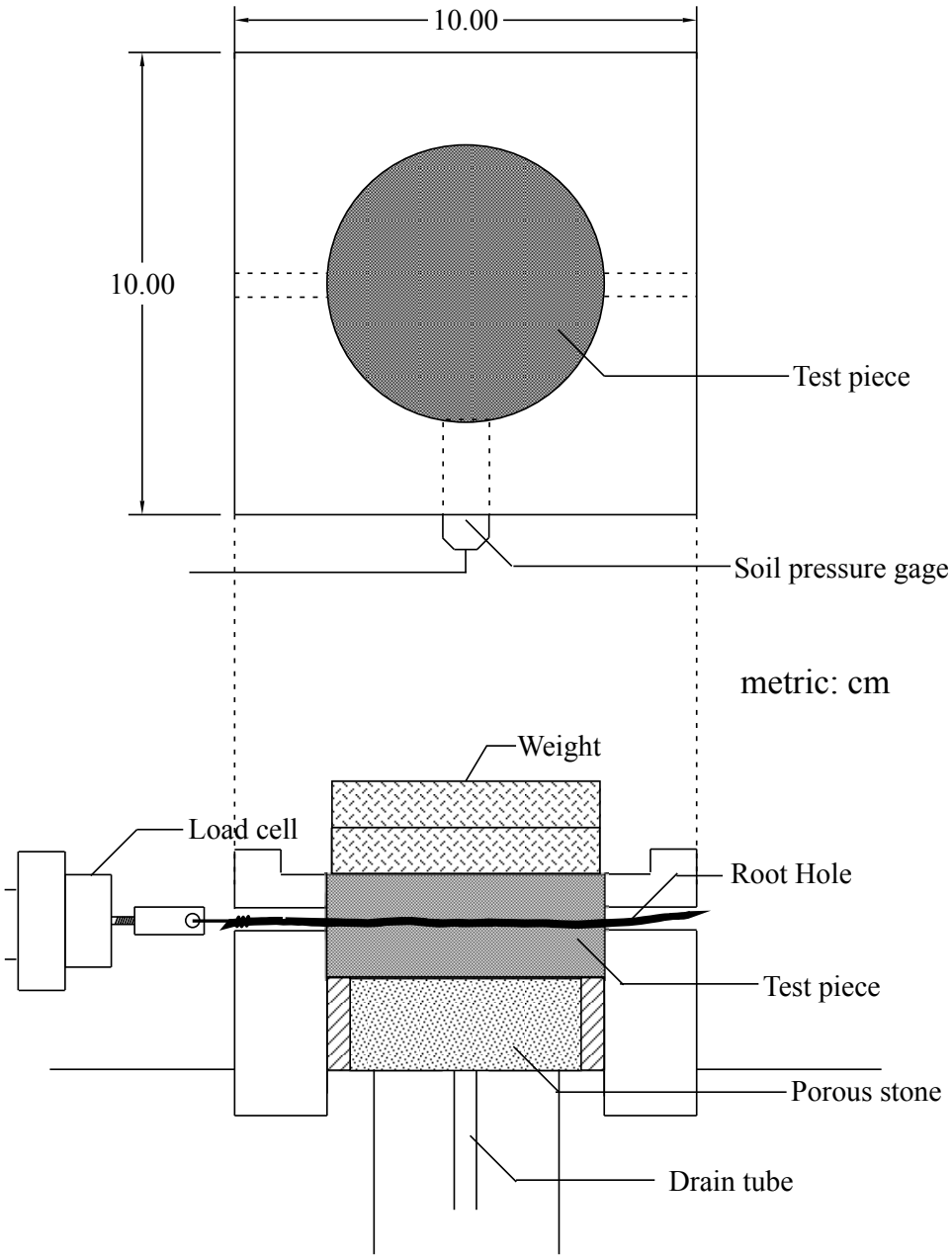

Figure 3.1: Schematic view of pullout apparatus which measures the shear stress in root-soil interfaces for given soil pressures.

3.2.2 Material properties

There are three case of experiments are conducted (indicated as Case 1 to Case 3). As the Case 1, pullout tests of a steel test-piece and silica sand No.7 is performed; this case is for validation of the apparatus and the procedure, thereby, the results are compared with the experiments of previous studies (Uesugi and Kishida 1986a, 1986b). In the Case 2, the same silica sand No. 6 is chosen, and instead of a steel test-piece, the same size (the diameter is about 3.0 mm) of wooden test-piece is utilized to observe the difference of shear behavior due to the difference of pull-out material, where the type of the wood is the balsa. Afterward, Case 3 is presented, where the apparatus is utilized for root-soil interfaces. Prior to the experiment, a root of barley and soil of the paddy field is sampled from the same site. The cite is located at an experimental field of Kyoto University in Sakyo-Ku, Kyoto City, Japan (35 ° 01'56.9"N 135 ° 47'00.4"E). The soil particle density of silica sand No. 6 and paddy soil is 2.67 g/cm^3 and 2.76 g/cm^3, respectively. The particle size distribution curveof the paddy soil is plotted in Fig. 3.2, and the liquid limit, plastic limit, plasticity index are 48.3 %, 35.4 %, and 13.1 %, respectively. Therefore, the soil is categorized as FS according to the standard of JGS 0051 (JGS, 2010). The bulk density of the paddy soil is 1.28 g/cm^3, and the dry density of the soil is 0.97 g/cm^3. The water content of the paddy soil is set as a value of 31.5 %, which is consistent with the water content of the sampling site.

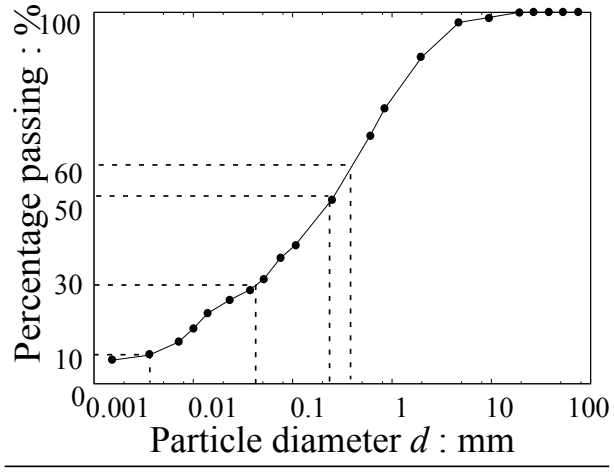

Figure 3.2: Material profiles of paddy soil utilized in experiment.

3.2.3 Procedure of pull-out test

The procedure of the pull-out test is shown below:

1. Dry sand is prepared for Case 1 and Case 2, and the water content of paddy soil used in Case 3 is set as 31.5 %.

2. The height and width of the soil-box are measured, and afterward, the soil pressure gauge is set in the soil-box and calibrated. Since the soil pressure is measured, the soil pressure gauge is started at this timing.

3. The pull-out materials are processed so that the length of the segment is 10.0 cm. The diameter of the materials is measured two times for each end of the materials, and the average of the diameters is used as the diameter of the material. The root segment is sampled from roots of barley; a root without branch roots is chosen for the test. The root is washed and tied to the force gauge by using a cotton string. The edge of the root is covered by wet papers to prevent drying. The steel and the wood are also tied to the force gauge in the same way.

4. Soils are filled into the soil-box. The paddy soil in Case 3 is filled into soil-box so that the bulk density is 1.28 g/cm^3. Here, the soil is divided into four and supplied four separate times. The top of the soil surface is flattened by using a soil knife. The weights are put onto the soil specimen. It is worth noting that the horizontal soil pressure is measured during this time.

5. Vertical displacement of the soil surface is measured by a displacement gauge until the deformation is stopped. It took less than 5 minutes in Case 1 and 2 and took more than 20 minutes in Case 3.

6. After the deformation is stopped, the pull-out material is pulled out with a speed of 0.1 mm/min and over 6.0 mm. During the pull-out process, the profiles of the horizontal soil pressure (kPa), pull-out force (N), horizontal displacement (mm) are measured.

7. The process 1 to 6 is repeated for several weights. In the case of the root-soil interface, the root is worn out when it is used for more than five times; therefore, the tests are repeated four times in Case 3.

After the experiment, water content (%), dry bulk density g/cm^3 is measured. The normal stress and shear stress of interfaces are estimated by $\sigma = (\sigma_1 + \sigma_2)/2$, where σ_1 is vertical soil pressure induced by weights, σ_2 is the horizontal soil pressure measured by the soil pressure gauge. This equation is derived by the following operations. First, Cauchy's stress tensor of the soil is expressed as below.

$$\sigma = \frac{1}{2\pi r L}\int_A \sigma \mathbf{n} \cdot \mathbf{n} dA \tag{3.1}$$

with

$$\sigma = \begin{pmatrix} \sigma_1 & 0 & 0 \\ 0 & \sigma_2 & 0 \\ 0 & 0 & \sigma_2 \\ , & & \end{pmatrix} \tag{3.2}$$

$$\mathbf{n} = \begin{pmatrix} cos\theta \\ sin\theta \\ 0 \end{pmatrix} \tag{3.3}$$

where $\mathbf{n}$ is outer normal on the pull-out material surface, σ is mean is outer normal on the pull-out material surface, σ is mean normal stress on pull-out material, r and L are mean radius and length of pull-out material, respectively, π is circle ratio, A is the interface of pull-out material and soils. From above equations, Eq. (3.4) is derived.

$$\sigma = \frac{1}{2\pi r L}\int_A \begin{pmatrix} \sigma_1 & 0 & 0 \\ 0 & \sigma_2 & 0 \\ 0 & 0 & \sigma_2 \end{pmatrix} \begin{pmatrix} cos\theta \\ sin\theta \\ 0 \end{pmatrix} \cdot \begin{pmatrix} cos\theta \\ sin\theta \\ 0 \end{pmatrix} dA \tag{3.4}$$

is derived. From Eq. (3.4) , Eq. (3.5) is computed.

$$\sigma = \frac{1}{2\pi r L}\int_A \sigma_1 sin^2\theta + \sigma_3 cos^2\theta dA. \tag{3.5}$$

In this chapter, the pull-out materials can be seen as a cylinder, therefore, Eq. (3.5) can be rewritten as Eq. (3.6).

$$\sigma = \frac{1}{2\pi r L}\int_0^{2\pi} \sigma_1 + (\sigma_3 - \sigma_1) cos^2\theta r L d\theta. \tag{3.6}$$

From the relationship of Eq. (3.6), $\sigma = (\sigma_1 + \sigma_2)/2$ is derived. On the other hand, the shear stress of root-soil interface is computed by Eq. (3.7),

$$\tau = \frac{S}{2\pi r L}. \tag{3.7}$$

Here, as shown in Fig. 3.3, a inflection point is appeared in the relationship between displacement and shear stress, which is due to the slack of a cotton string. The similar phenomena is occurred in the unconfined compression tests (JIS A 1216) and a modification of the origin is proposed in the standard; this modification is also applied to the current procedure as shown in Fig. 3.3.

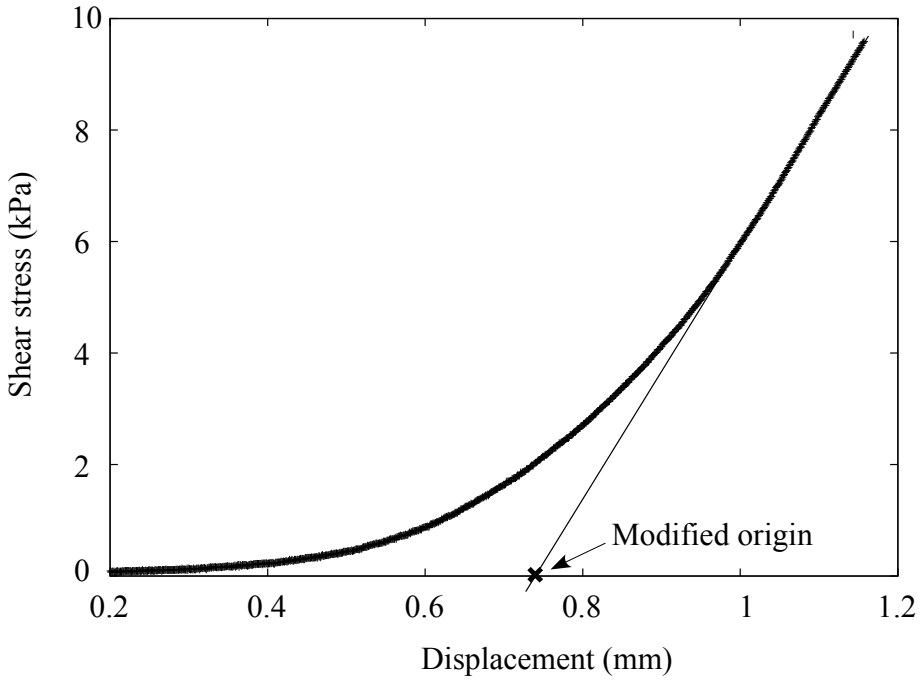

Figure 3.3: Modification of the origin to determine theoretical origin analogous to JGS-0520:2009

3.3 Results and discussion

3.3.1 Shear test of steel-sand interface

The relationship between shear displacement and shear stress for under different normal stress is visible in Fig. 3.4. For all cases, shear stress is proportional to the shear displacement when the shear displacement is less than 0.5 mm. In this section, the gradient of this initial curve is denoted as *shear displacement modulus* in this chapter. The shear stress starts declining as shear displacement reaches around 0.5 mm to 1.5 mm and reaches the maximum shear stress. After the peak shear stress, the shear stress decreases with oscillation, and finally becomes 20% to 50% of the peak shear stress.

The relationship between normal stress and shear displacement modulus is displayed in Fig. 3.5. The results suggest that a shear displacement modulus is proportional to the normal stress of a root-soil interface. This coefficient is used in the constitutive modeling of Section 4.

The relationship between normal stress and maximum shear stress is shown in Fig. 3.6. It is indicated that the maximum shear stress is proportional to the normal stress (R^2 = 0.98). The intercept of the line is around 0 kPa, and the coefficient is around 0.28. This relationship is well-known Coulomb's friction, and the coefficient is consistent with the frictional coefficient. Hence, it shows that the frictional coefficient between steel and silica sand No. 7 is 0.28. The frictional coefficient is almost the same as or a little smaller than

the frictional coefficient reported by previous studies (Uesugi and Kishida, 1986).

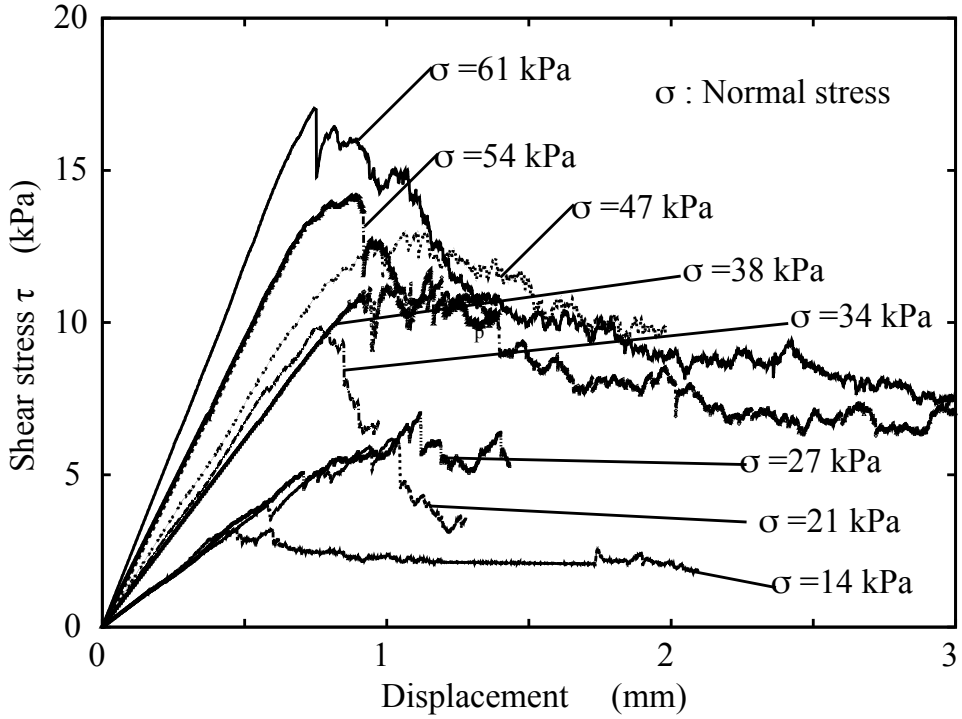

Figure 3.4: Relationship between displacement and shear stress measured by pull-out test of steel and silica sand

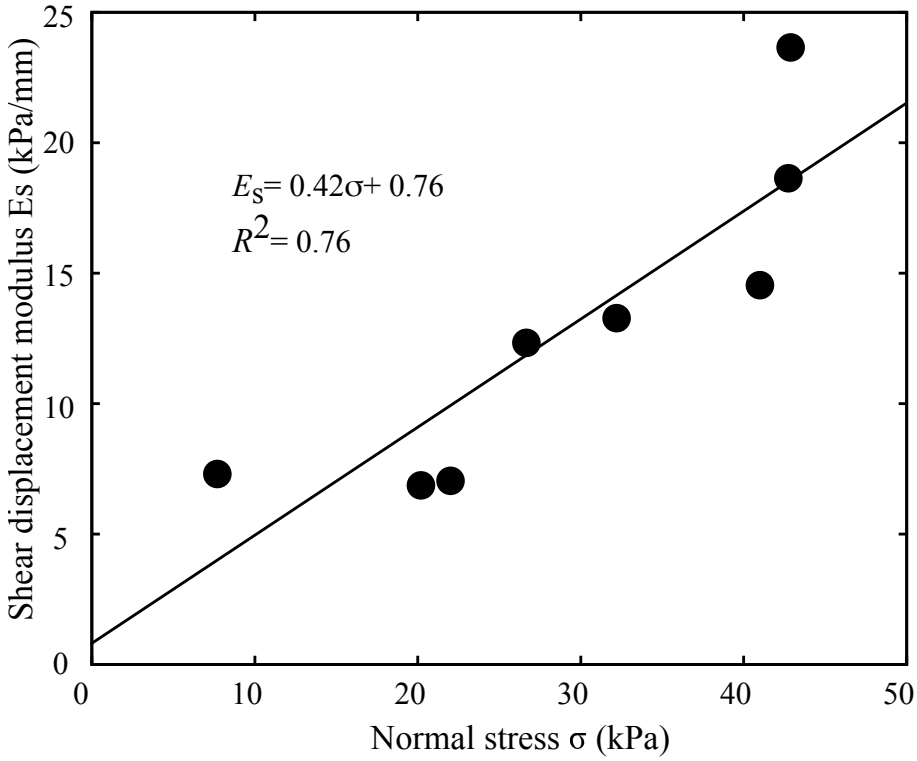

Figure 3.5: Relationship between normal stress and shear displacement modulus measured by pull-out test of steel and silica sand

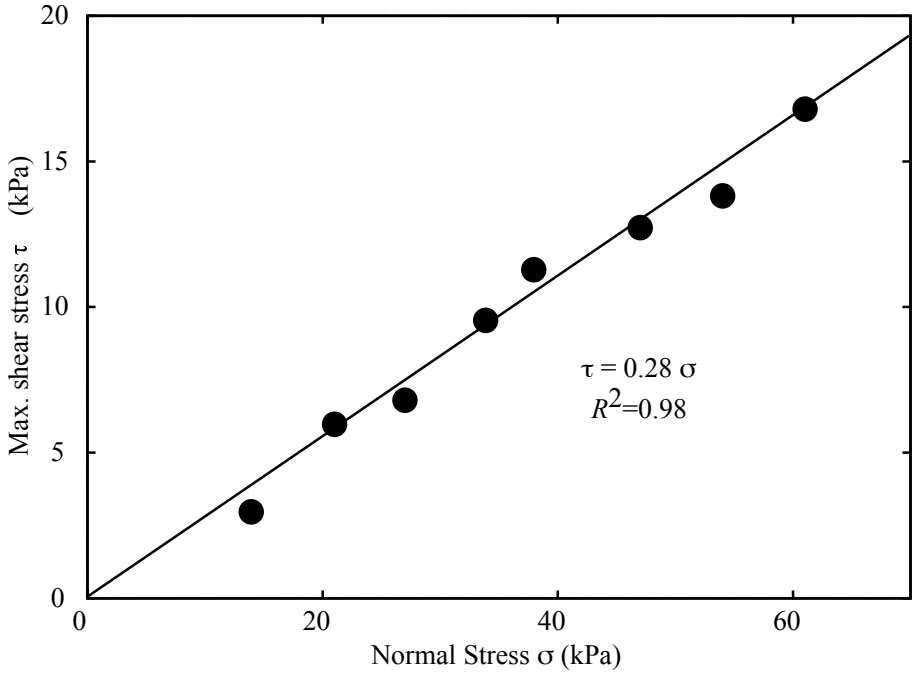

Figure 3.6: Relationship between normal stress and shear stress measured by pull-out test of steel and silica sand

3.3.2 Shear test of wood-sand interface

The relationship between shear displacement and shear stress for under different normal stress is visible in Fig. 3.7. For all cases, shear stress is proportional to the shear displacement when the shear displacement is less than 1.0 mm. The shear stress starts declining as shear displacement reaches around 1.0 mm to 6.0 mm and reaches the maximum shear stress, which is greater than these of the steel-sand case. After the peak shear stress is observed, the shear stress keeps almost the same value over 0.5 mm to 1.0 mm and decreases with oscillation, and the finally becomes 40% to 60% of the peak shear stress.

The relationship between normal stress and shear displacement modulus is displayed in Fig. 3.8. The results suggest that a shear displacement modulus is proportional to the normal stress of a wood-sand interface. This coefficient is also used in the constitutive modeling of Section 4.

The relationship between normal stress and maximum shear stress is shown in Fig. 3.9. It is indicated that the maximum shear stress is proportional to the normal stress ($R^2 = 0.99$). The intercept of the line is 1.81 kPa, and the coefficient is around 0.94. This relationship is well-known Coulomb's friction, and the coefficient is consistent with the frictional coefficient. Hence, it shows that the frictional coefficient between wood and silica sand No. 7 is 0.97: The frictional coefficient is larger than that of the steel-sand case, which indicates that the current method provides a unique frictional coefficient for each combination of materials. Further, a small amount of cohesion is observed. Since it does not appear in the steel-sand test, it is suggested that the cohesion is due to the softness of the wood material.

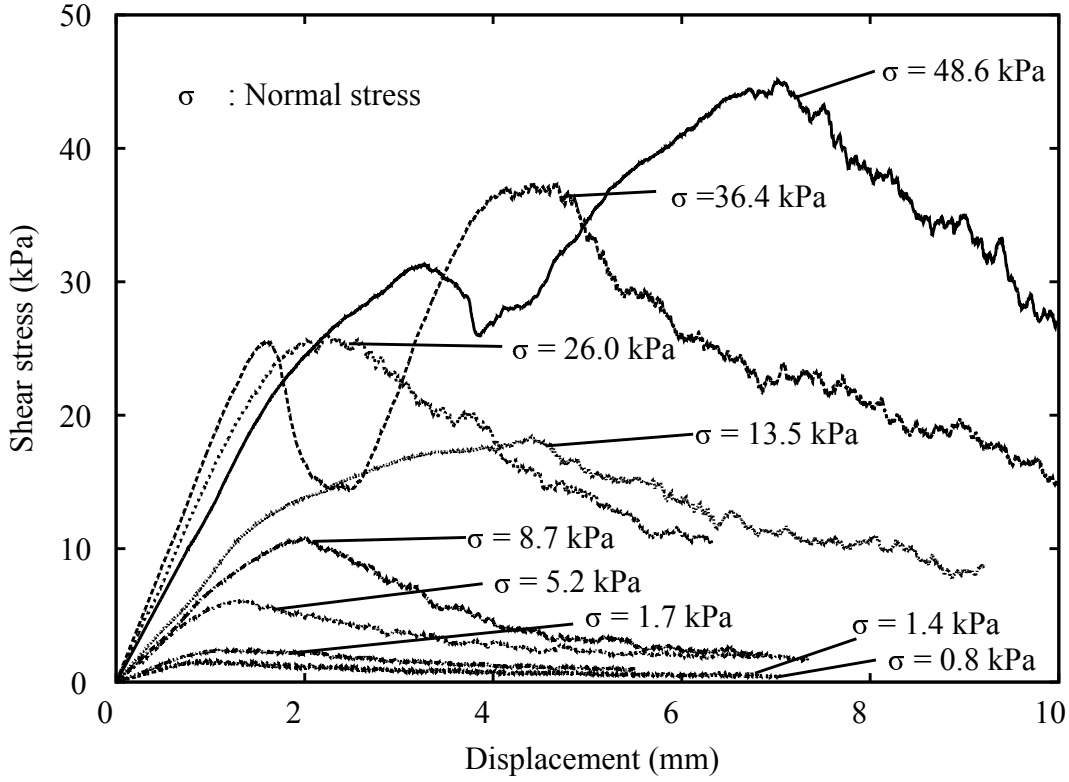

Figure 3.7: Relationship between displacement and shear stress measured by pull-out test of wood specimen and silica sand.

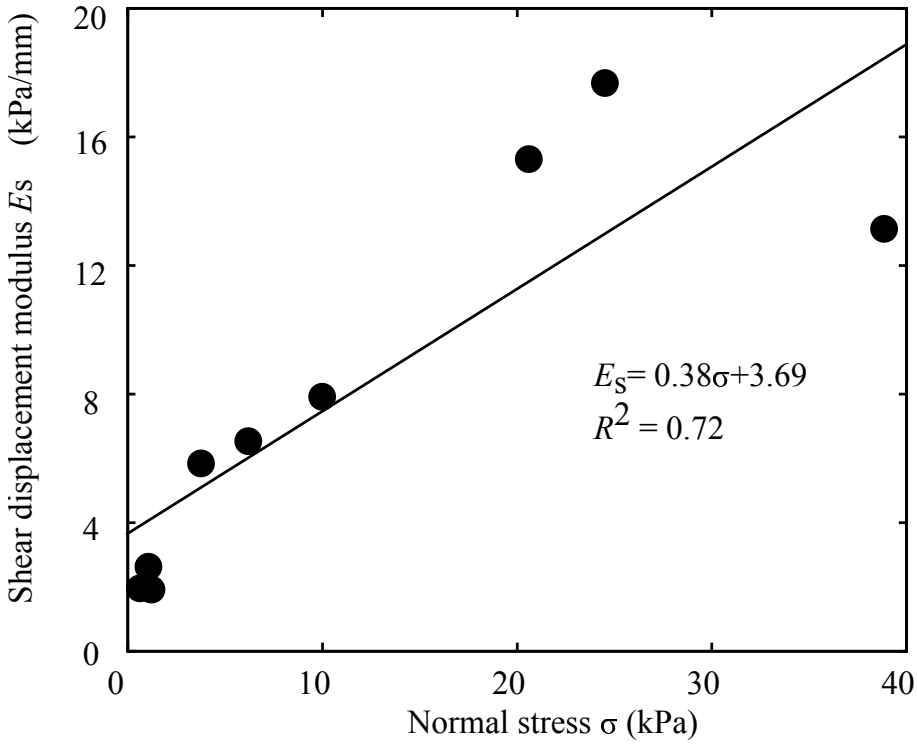

Figure 3.8: Relationship between normal stress and shear displacement modulus measured by pull-out test of wood specimen and silica sand.

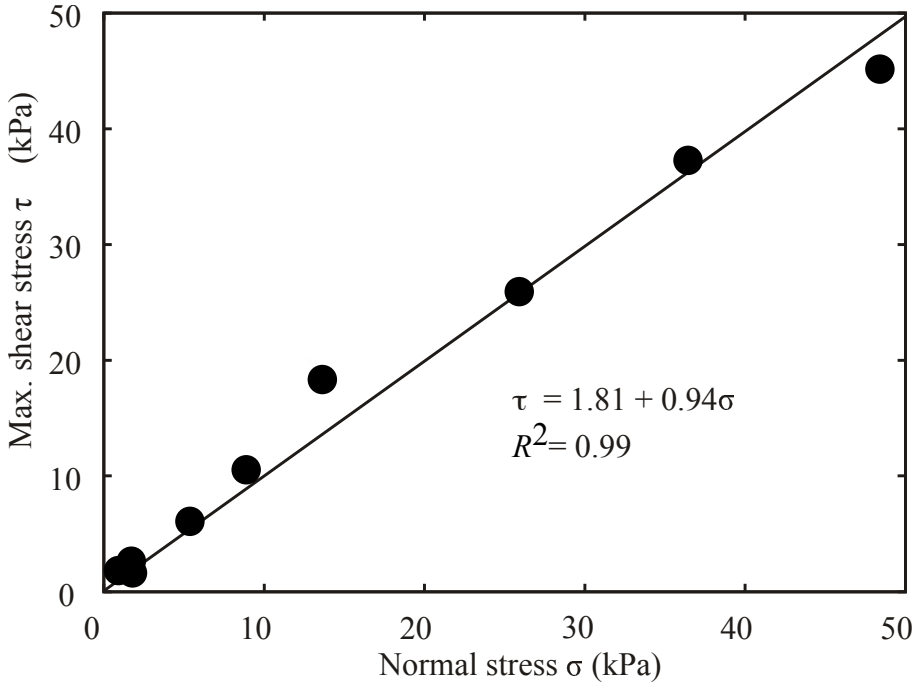

Figure 3.9: Relationship between normal stress and shear stress measured by pull-out test of wood specimen and silica sand.

Table 3.1: Dry density and water content of test pieces.

	Original	1.7 kPa	3.6 kPa	6.1 kPa	8.3 kPa
Dry density g/cm^3	0.97	0.96	0.97	0.96	0.98
Water content %	31.5	32.4	30.8	33.1	29.9

3.3.3 Shear test of root-soil interface

The dry densities of specimens are measured after the experiments Table 3.1. For all cases, the initial dry density is 0.97 g/cm^3, and the water content is 31.5 %. After the experiment, the dry density is 0.96 g/cm^3 to 0.98 g/cm^3, which is almost the same as the original value. The water content also did not change significantly. From these results, the mechanical properties of soils did not changed significantly during the experiment since the soil pressure is extremely small.

The relationship between shear displacement and shear stress for under different normal stress is visible in Fig. 3.10. For all cases, shear stress is proportional to the shear displacement when the shear displacement is less than 2.0 mm. The shear stress starts declining as shear displacement reaches around 2.0 mm to 7.0 mm and reaches the maximum shear stress, which is greater than these of the steel-sand case. After the peak shear stress is observed, the shear stress keeps almost the same value over 2.0 mm to 5.0 mm and decreases with oscillation, and the finally becomes 30% to 50% of the peak shear stress. This figure also shows that the current case is more cohesive than other cases, which should be due to the cohesion of the soil material or softness of the root.

The relationship between normal stress and shear displacement modulus is displayed in Fig. 3.11. The results suggest that a shear displacement modulus is proportional to the normal stress of a root-soil interface. This coefficient is also used in the constitutive modeling of Section 4.

The relationship between normal stress and maximum shear stress is shown in Fig. 3.12. It is clearly indicated that the maximum shear stress is proportional to the normal stress (R^2 = 0.98). The intercept of the line is 3.14 kPa, and the coefficient is around 0.60. This relationship is consistent with the well-known Mohr-Coulomb's model, and the coefficients are consistent with the frictional coefficient; hence, it shows that the frictional coefficient between the root and the soil is 0.60. The frictional coefficient is larger than that of the steel-sand case and less than the wood-sand case. Further, the cohesion is greater than that of the wood-sand case, which characterizes the shear strength of root-soil interfaces out of other cases.

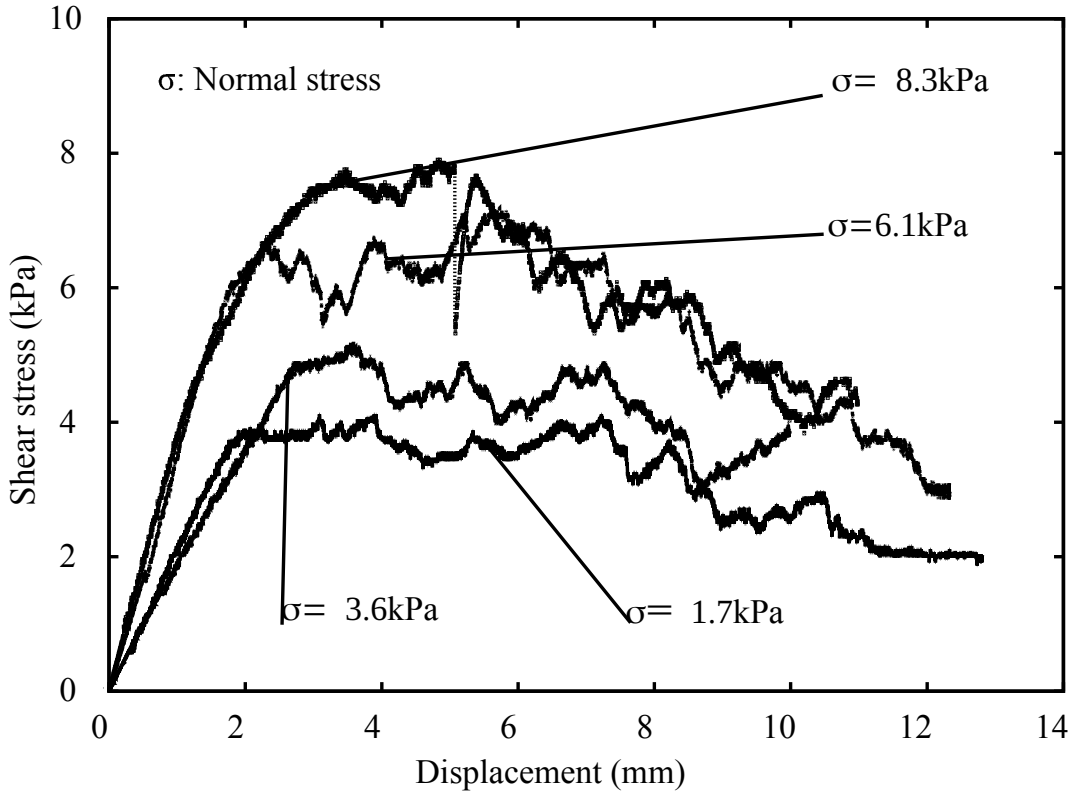

Figure 3.10: between displacement and shear stress measured by pull-out test of root of a barley plant and paddy soil.

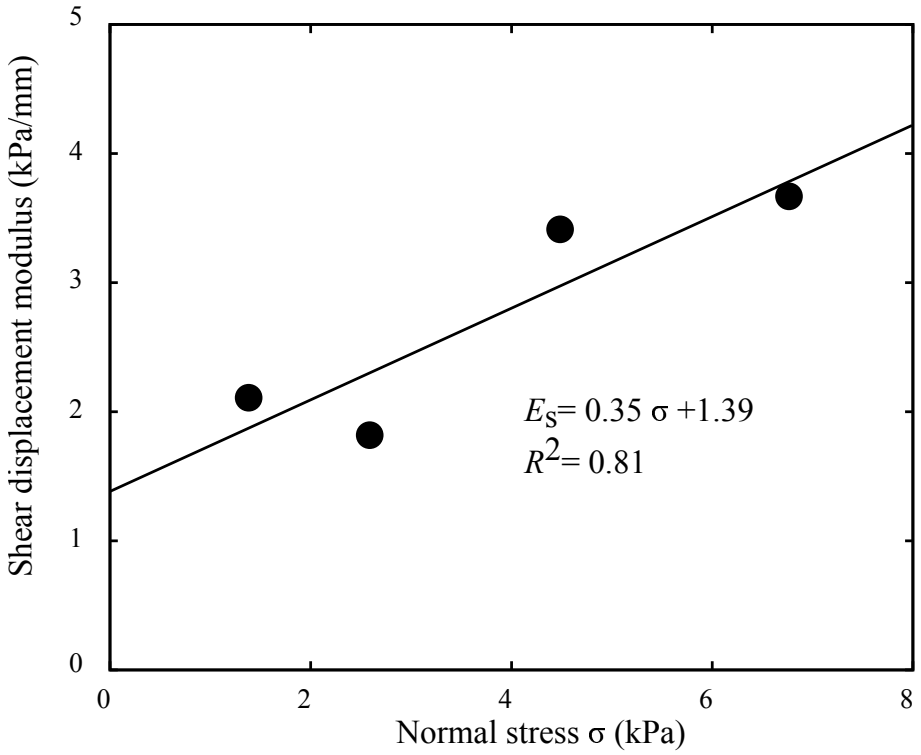

Figure 3.11: Relationship between normal stress and shear displacement modulus measured by pull-out test of root of a barley plant and paddy soil.

3.4 Constitutive model of shear behavior

This section proposes a constitutive model for root-soil interfaces which reproduce the relationship between shear displacement and shear stress. CCM is one of the most widely-used approaches to model the relationship between shear displacement and shear stress (Wriggers, 2006). Simple and typical modeling of the interfacial constitutive model is analogous to the elasto-plasticity theory(Wriggers, 2006). When the shear displacement is small, the shear stress is proportional to the shear displacement, and after the shear stress reaches the shear strength, the shear stress keeps the same value as the shear strength even if the shear displacement is increased. Further, if the shear displacement is decreased, the shear stress proportionally decreases, and the shear stress increases when the shear displacement is increased again. The stress-displacement relationship is analogous to the stress-strain relationship of elastoplastic constitutive relationship; hence, the mathematical expression is also similar to the elastoplastic constitutive models (Wriggers, 2006). The elastic part of the interfaces are called stick, and the plastic part is called slip. the displacement with the stick is called elastic displacement u^e, and the displacement with the slip is called plastic displacement u^p. Further, the yield function of interfaces is called slip criterion, which governs the shear strength of interfaces. The above-mentioned relationships are mathematically expressed as below. The total displacement of interfaces are decomposed as (3.8).

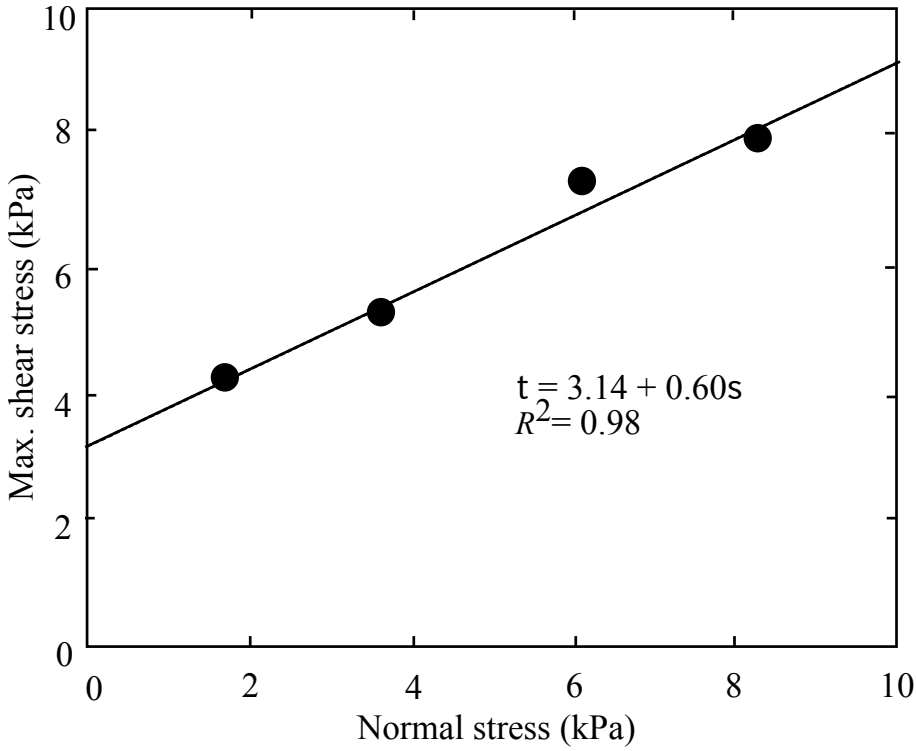

Figure 3.12: Relationship between normal stress and shear stress measured by pull-out test of root of a barley plant and paddy soil.

$$u_i = u_i^e + u_i^p \tag{3.8}$$

where u_i^p is the total relative displacement, u_i^e is the plastic part of the displacement, and u_i^p is the plastic part. The elastic and the plastic part is governed by following rules seen in the following subsections.

3.4.1 Constitutive model of elastic stick

The shear stress and the shear displacement of an interface are represented by vectors as Eq. (3.9)

$$\tau_i = \begin{pmatrix} \tau_1 \\ \tau_2 \end{pmatrix}, u_i = \begin{pmatrix} u_1 \\ u_2 \end{pmatrix}. \tag{3.9}$$

The shear stress is proportional to the shear displacement in case of stick phase. The relationship is generally written as Eq. (3.10)

$$\tau_i = C_{ij} u_j^e \tag{3.10}$$

where C_{ij} is a elastic modulus tensor. Here, it is reasonable to assume isotropy of the shear behavior, hence, the Eq. (3.10) is rewritten by using shear displacement modulus E_s as Eq. (3.10)

$$\tau_i = E_s \delta_i j u_i^e, \tag{3.11}$$

where $\delta_i j$ is unit tensor. The results of pull-out tests of root-soil case indicates that the shear displacement modulus E_s is proportional to the stress σ, which is expressed by Eq. (3.12)

$$E_s = \alpha\sigma + \beta \tag{3.12}$$

where α and β are model parameters. On the other hand, slip criterion is expressed based on Mohr-Coulomb model

$$f_s = \|\tau\| - c - \sigma \tan\phi = 0 \tag{3.13}$$

where c and ϕ are cohesion and frictional angle, respectively. In case of $f_s < 0$, the state is in stick, and slip occurs when $f_s = 0$; the process is visualized by using a space of σ, τ_1 and τ_2 in Fig. 3.14. If the stress-state is in the cone, the state is stick; if the stress-state is on the cone, the state is slip.

3.4.2 Constitutive model of plastic slip

From Eqs. (3.8), (3.10) and (3.13), constitutive model of the root-soil interface is expressed as Eq. (3.14)

$$\tau_i = E_s \dot{u}_i^e \tag{3.14}$$

substituting Eq. (3.8) into Eq. (3.14),

$$\dot{\tau}_i = E_s \left(\dot{u}_i - \dot{u_i^p} \right) \tag{3.15}$$

is given. Now, assuming the associated flow rule, the plastic velocity is given as Eq. (3.16),

$$\dot{u_i^p} = \gamma \left(\frac{\partial f_s}{\partial \tau_i} \right)^T = \gamma \frac{1}{\sqrt{\tau_k \tau_k}} \tau_i \tag{3.16}$$

where γ is slip multiplier which indicate the degree of plastic velocity. It is worth noting that the Eq. (3.16) says that the direction of the shear stress is consistent with the direction of slip, which is natural assumption. By taking total derivative of the Eq. (3.13),

$$df_s = \frac{\partial f_s}{\partial \tau_i} \dot{\tau}_i + \frac{\partial f_s}{\partial \sigma} \dot{\sigma} = 0 \tag{3.17}$$

the multiplier γ is determined below.

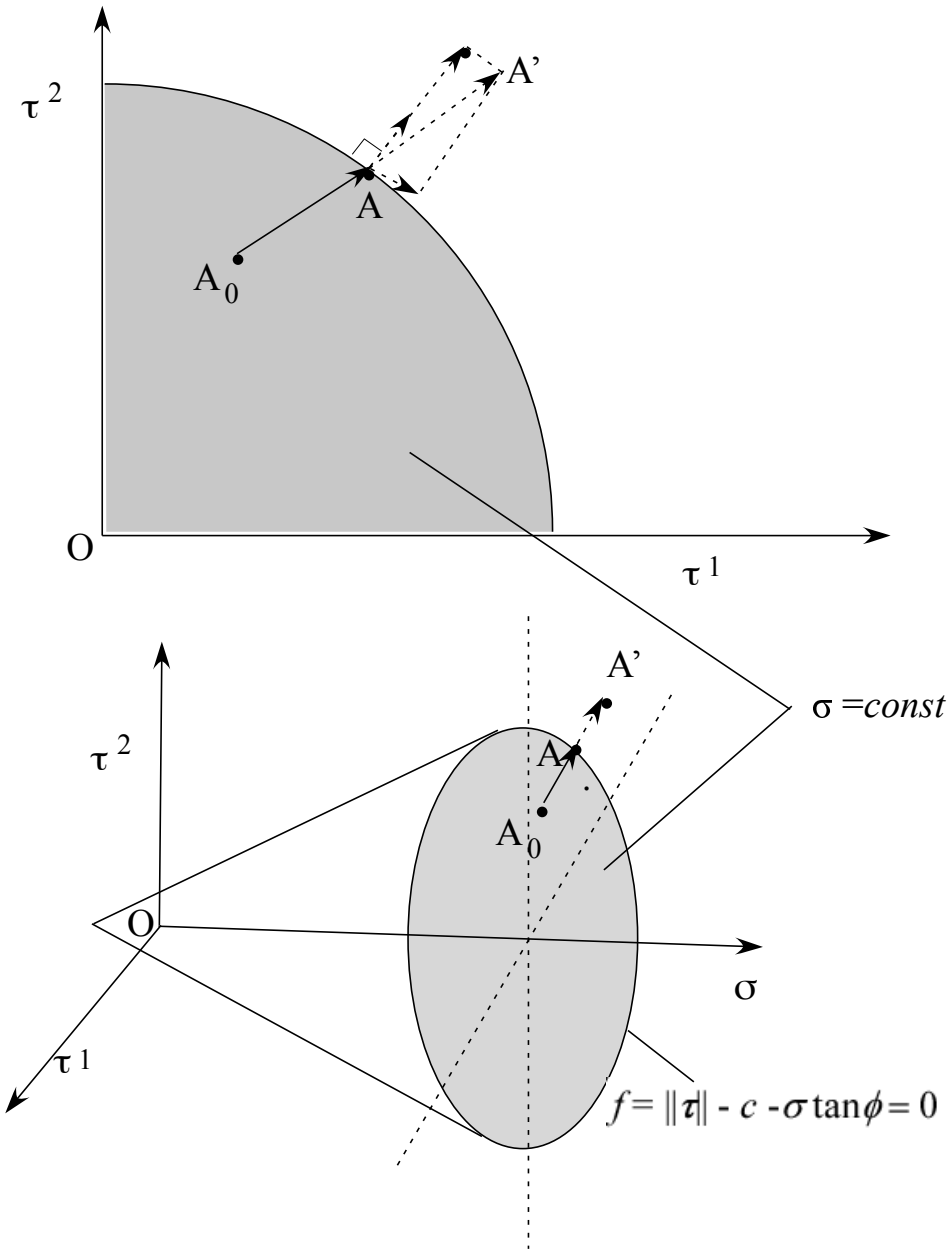

Figure 3.13: Schematics of slip criterion.

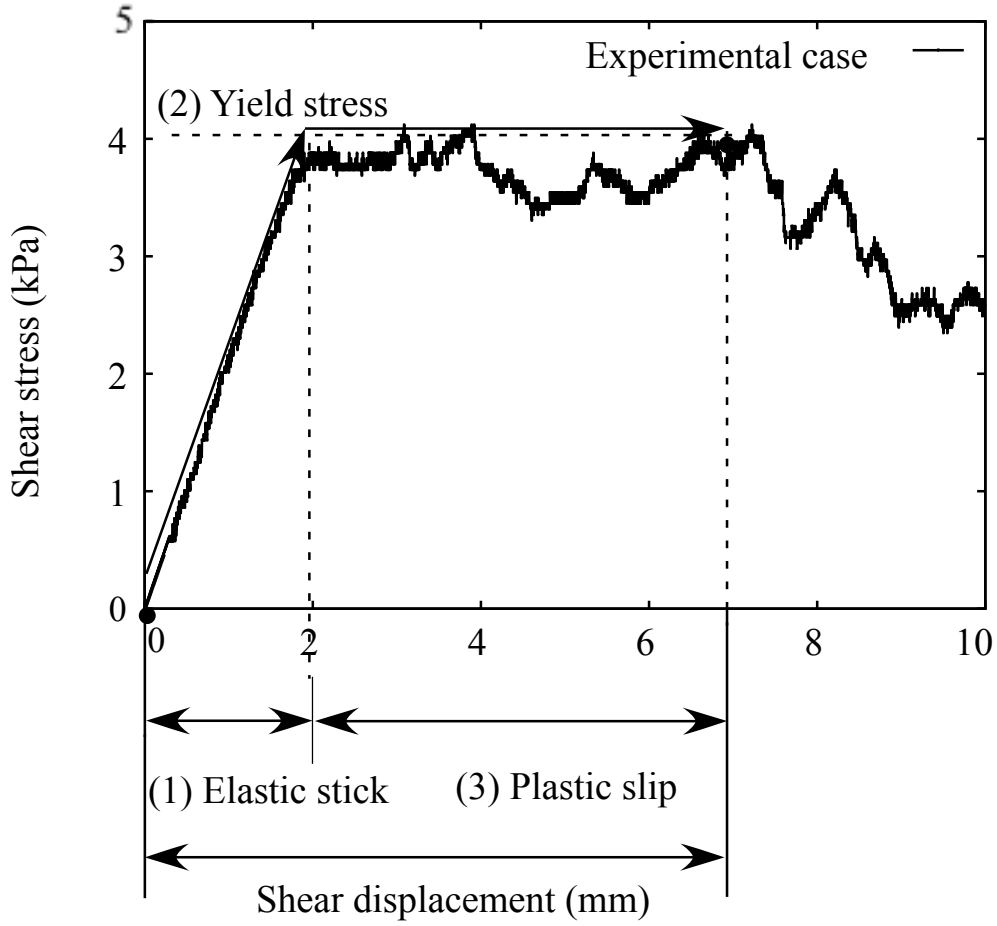

Figure 3.14: Additive decomposition of displacement and shear stress vs. displacement by elastio-perfectly-plastic model.

$$\gamma = \frac{E_s \frac{\partial f_s}{\partial \tau_i} \dot{u}_i + \frac{\partial f_s}{\partial \sigma} \dot{\sigma}}{\frac{\partial f_s}{\partial \tau_k} \frac{\partial f_s}{\partial \tau_k}^T} \tag{3.18}$$

Here, $\dot{\sigma}$ is time derivative of normal stress. The constitutive relationship is obtained by substituting Eqs. (3.16) and (3.18) into Eq. (3.15).

$$\dot{\tau}_i = E_s \left(\delta_{ij} - \frac{1}{\sqrt{\tau_k \tau_k}} \tau_i \tau_j \right) \dot{u}_j - \frac{\dot{\sigma} tan\phi}{\sqrt{\tau_k \tau_k}} \tau_i \, (\gamma \geq 0) \tag{3.19}$$

$$\dot{\tau}_i = E_s \tau_i \, (\gamma \geq 0) \, . \tag{3.20}$$

Fig. 3.15 displays an example of computation of strain for a slip case. The momentum balance is achieved in τ_i and the shear stress increases $\dot{\tau}_i$ and trial stress state is shifted to **A**'. In this case, the stress state remains on the slip criterion as **A**, and slip is increased, the amount of which is computed by the Eq. (3.20).

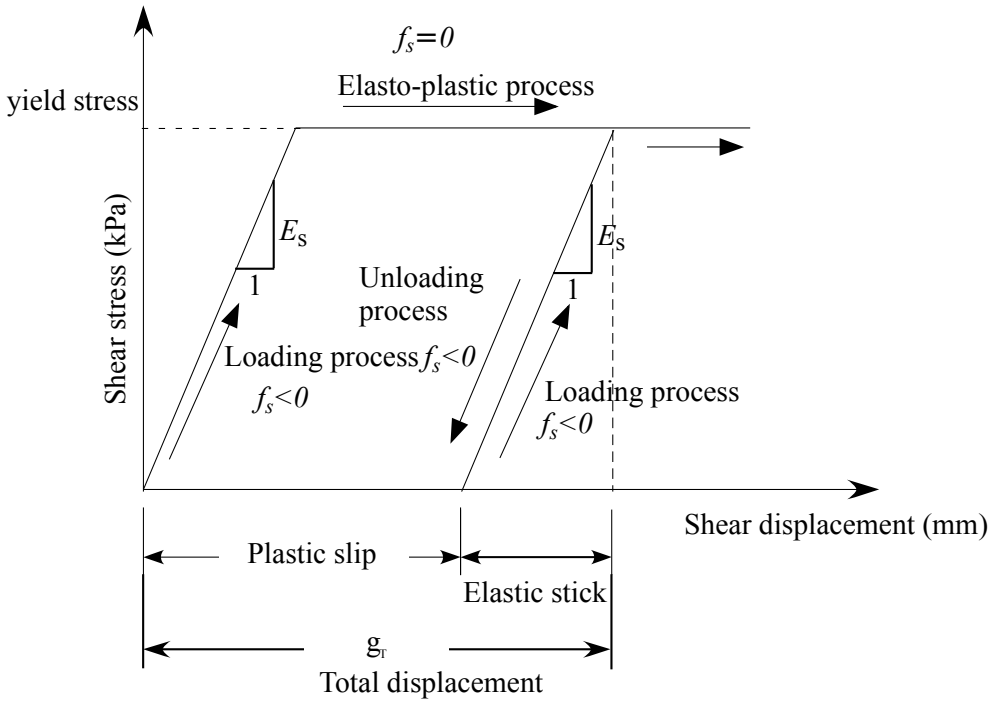

Figure 3.15: Schematic view of loading-unloading process modeled by the Computational Contact Mechanics.

3.4.3 Parameter fitting and validation

The results of parameter fitting are shown in Figs. 3.16, 3.17 and 3.18. The presented model is similar to the experiment from the stick state to the slip state. The presented model and the experiment are almost identical when the shear stress is smaller than the slip criterion, which indicates that the elasticity model of the present model is capable of reproducing stick behavior. For each case, the estimated shear strength of interfaces is also consistent with the experiment. Therefore, it is indicated that the Mohr-Coulomb model is applicable to contact problems. Although the shear stress of the model is not identical to the experiment as the displacement is increased, the softening can be expressed by using the more complex models in future studies.

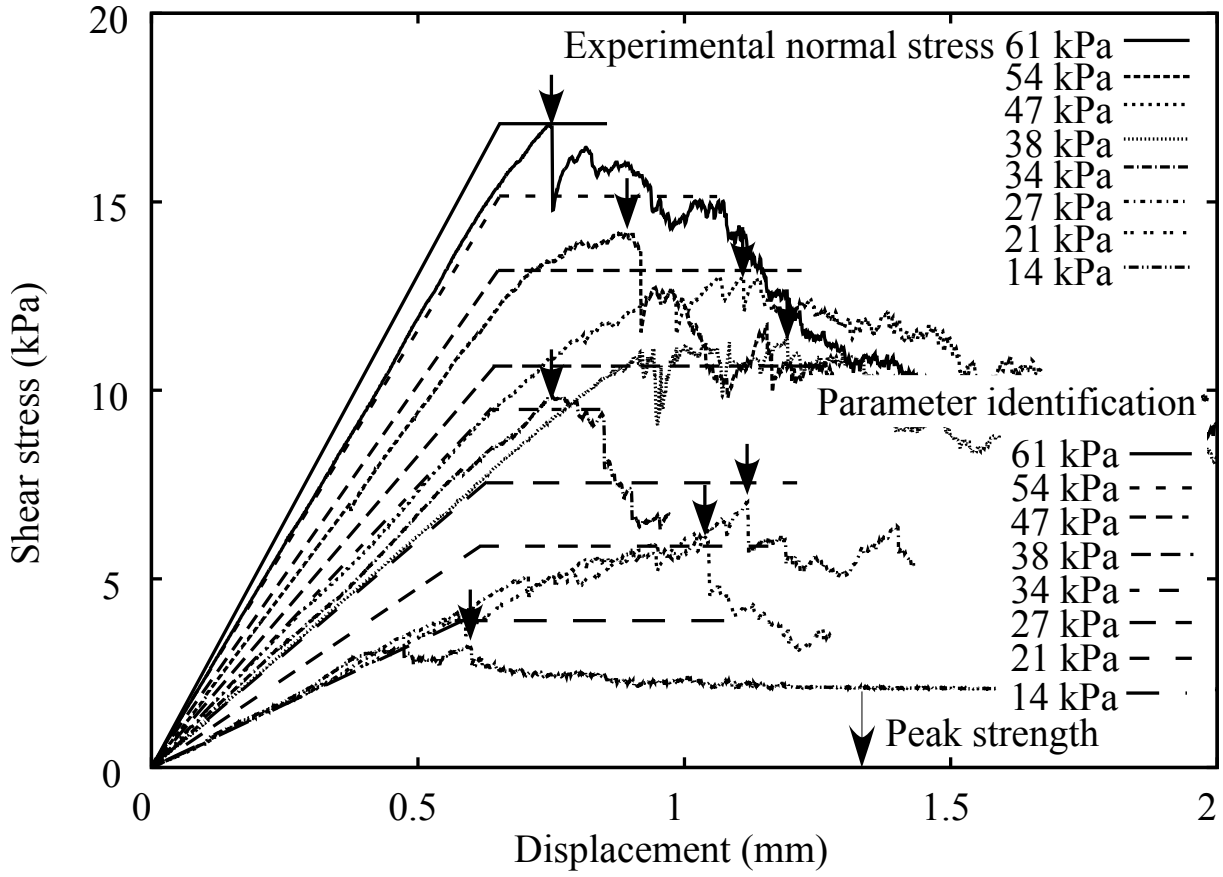

Figure 3.16: Relationship between shear stress and displacement and results of fitting based on the present model in case of steel-sand tests.

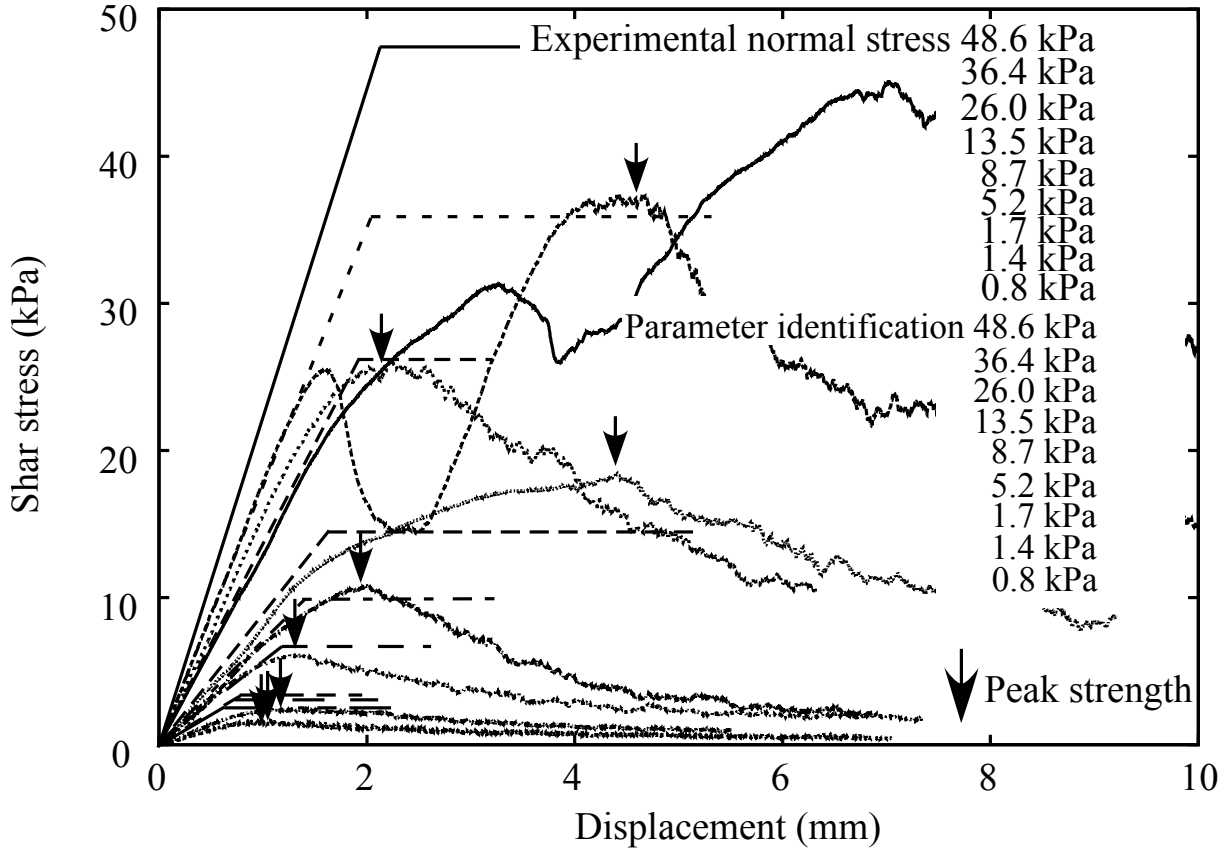

Figure 3.17: Relationship between shear stress and displacement and results of fitting based on the present model in case of wood-sand tests.

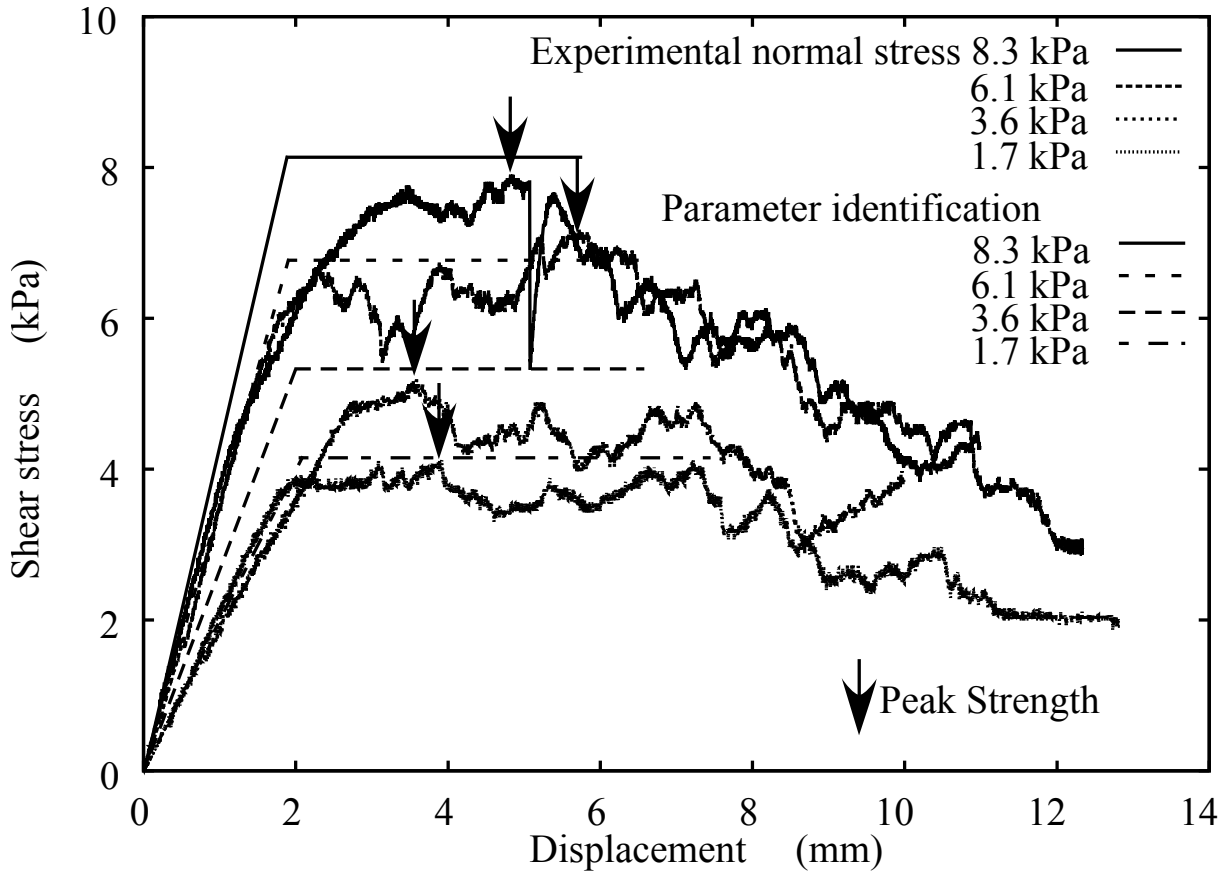

Figure 3.18: Relationship between shear stress and displacement and results of fitting based on the present model in case of root-soil tests.

3.5 Summary

According to the results of pull-out tests, the proposed apparatus and method can measure the relationship between displacement and shear stress of the root-soil interface. For all cases, shear stress is proportional to the shear displacement when the displacement is relatively small and becomes constant after the peak shear stress. The peak shear stress can be used as the shear strength of root-soil interfaces, and the shear strength is clearly proportional to the normal stress for all cases. The Mohr-Coulomb model can model the critical state line, and the cohesion and the frictional coefficient is precisely measured. The cohesions are greater in the following order: root-soil case > wood-sand case > steel-sand case. The frictional coefficient is larger in the following order: wood-sand case > root-soil case > steel-sand case. It is also suggested that the relationship between shear displacement and shear displacement coefficient is proportional. These properties are modeled based on CCM, which is analogous to the elasto-plasticity theory of soils. The result of parameter fitting shows that the current model can reproduce the profile of shear stress of the experiments. Although the current model cannot express the softening of the root-soil interface, this point will be overcome by introducing more flexible and modern models in future studies. The future study also targets the application of the current model with a numerical method such as the FEM to simulate more realistic problems for root lodging of cereals and slope stability problems of vegetated slopes.

Chapter 4

Experiments and FE-Analysis of 2-D Root-Soil Contact Problems Based on Node-To-Segment Approach

4.1 Introduction

The roots of plants play an essential role in the mechanical stability of both slopes and plants. It has been reported that through the reinforcement of soil masses, roots reduce the risk of disasters such as landslides and surface erosions (Abe and Ziemer, 1991; Freer, 1991; Dupuy et al., 2007; Bischetti et al., 2010; Mickovski et al., 2011). Field investigations have revealed that the failure and erosion of soils are often induced by the loss of shear strength in the shallow parts of slopes, where roots can reinforce their strength (Perry, 1989; Mickovski et al., 2010). The mechanism of root reinforcement is of interest in terms of developing low-cost techniques for slope stabilization using vegetation (Schwarz et al., 2011; Hejazi et al., 2012). Further, it has been confirmed that roots also contribute to sustaining the productivity of agriculture and forestry because roots resist the lodging of trees and crops (Shimada et al., 2002; Wu and Ma, 2016). Severe lodging is frequently caused by the failure of root zones under heavy rains and/or strong winds. It damages the yield of cereals and impedes the growth of trees (Berry et al., 2004; Mickovski et al., 2011). To mitigate the risks of lodging, the mechanical response of root zones is of increasing significance.

Historically, the mechanical response of rooted soils has been investigated while considering the root-soil system to be a homogeneous system (Endo, 1980; Abe and Ziemer, 1991; Schwarz et al., 2011; Muir Wood et al., 2016). In these studies, the Mohr-Coulomb model was used to model the inelastic deformation of rooted soils, and the effects of root reinforcement were modeled by increasing the apparent cohesion term. In this context, Abe and Ziemer (1991) and Freer (1991) proposed some empirical models to explain the amount of the apparent cohesion. Such empirical approach shows that the apparent cohesion can be

roughly explained by such quantities as the root content per unit soil volume, the diameter of the roots, and the material properties of the roots and the soils. The main challenge faced by researchers is the trade-off between accuracy and the cost of the experiments. This is due to the fact that, in the homogeneous approach, the apparent cohesion of rooted soils is measured by direct shear tests. Hence, in order to conduct accurate simulations, it is desirable that a unique and a consistent value of cohesion is given for each material by the direct shear test. However, the specimens do not deform uniformly during the material tests and the results are disturbed by the existence of plant segments since rooted soils often contain large segments of plant roots and trunks. This inevitably necessitates the use of a large number of large-size undisturbed samples to obtain reliable results. The trade-off between the accuracy of such experiments and the cost of performing them to obtain the model parameters limits the applicability of the model.

Recently, novel numerical approaches have been proposed to investigate the detailed mechanism of root-soil contact interaction. Dupuy et al. (2007) and Mickovski et al. (2011) applied the Finite Element Method (FEM) with contact elements developed in computational contact mechanics to the deformation analysis of rooted soils. These studies are innovative for two points: First, the deformation of rooted soils is seen as a contact problem between roots and soils, and it visualizes the stress fields and deformation of root-soil systems. It has also been difficult to observe the slip and separation in the root-soil interfaces. These visualizations help us to understand the deformation behavior of rooted soils and improve homogeneous models. Second, High-resolution morphological data, such as scanning data or X-ray CT data, are directly available in the simulation. Since the morphology of roots characterizes the mobility of rooted soils (Hudek et al., 2017), this kind of recent approaches are useful to obtain precise and repeatable predictions of deformation of rooted soils. Previous studies have roughly modeled the constitutive relationship of the root-soil interfaces. Initially, the Node-To-Node (NTN) approach was used to express the root-soil interaction (Dupuy et al., 2007), where slip and separation were not allowed. Mickovski et al. (2011) overcame this limitation by using three-node Line Elements (LE) that can express the friction, and the friction was modeled using the Mohr-Coulomb model which has been validated through experimental studies (Schwarz et al., 2011; Tomobe et al., 2016; Ji et al., 2018). However, NTN approach is available only when the slip and the separation in the root-soil interfaces are not significantly large or can be ignored. Further, since LE approach approximates roots by fibers, it is difficult to directly input the root morphology and it limits the accuracy. To provide more accurate predictions, it is necessary that both problem is avoided to the model of the root-soil interfaces. The objective of this chapter is to apply the Node-To-Segment (NTS) approach (Zavarise et al., 2009) within the framework of the FEM to precisely simulate the contact phenomena of roots and soils with high-resolution morphological data of rhizosphere. In recent decades, this scheme has been the most widely used technique for various contact problems since it is simple and

can be adapted to geometrically nonlinear problems (Wriggers, 2006). Furthermore, the technique is capable of expressing complex and realistic geometries: it is flexible enough that high-resolution morphological data of roots which are scanned by cameras or X-ray CT technology (Hudek et al., 2017) can be input directly into the analysis. Although the NTS can overcome the problems mentioned above of NTN and LE methods, the robustness of it is lower than them, and it prevents researches from using it for root-soil contact problems (Dupuy et al., 2007), hence the current chapter challenges this point. One of the reason is the non-uniqueness of solutions. It appears especially when the method is used for geometrically complex problems like the root-soil system. Thereby, this chapter proposes a simple algorithm to avoid the non-uniqueness problem of the solutions with the NTS approach. This chapter is also focusing on measuring and using reliable material parameters and high-resolution geometrical data for roots, soils and root-soil interfaces to perform accurate simulations. Material properties of soils are measured mainly based on the laboratory testing standards of Japanese Geotechnical Society, the root parameters are measured by using bending tests, and the parameters of root-soil interfaces are measured by using pull-out tests (Tomobe et al., 2016). The morphological data is taken by digital camera and converted into a mesh data by using Python Imaging Library (PIL) and Gmsh (Geuzaine et al., 2009) that is an open-source pre-processing software to obtain a fine mesh. This chapter is organized as follows: The derivations of the governing equation, the discretization, and the solution algorithm are summarized in Sections 2 and 3. In Sections 2 and 3, a novel pairing algorithm is implemented in the NTS approach to solve the non-uniqueness problem of NTS pairing due to the geometrical nonlinearity of root-soil interfaces. The simulation code is firstly validated under geometrically linear condition by re-analyzing pullout tests in Section 4. Section 5 provides an experiment and a simulation of a lodging test, which is a horizontal loading test for a root planted in a soil-box to measure the bearing capacity of the rhizosphere. Lodging is a falling down of the plant bodies on grounds and it damages productivity and the quality of cereal crops such as rice, wheat, maize and soybean (Berry et al, 2003). The accurate prediction of the lodging has been required to find best agricultural practice and select the lodging-resistant varieties for decades. It also includes a novel technique for mesh-generation of roots and soils from a scanned image of the root architecture. Section 6 concludes all sections and future works.

4.2 Implementation of NTS approach

4.2.1 Implementation of NTS approach in root-soil contact problems

This section briefly discuss the implementation of contact/separation and stick/slip in root-soil interfaces based on the Node-To-Segment (NTS) approach, which allows contact and separation between two finite elements and also stick and slip is consistently expressed.

NTS approach utilizes Node-To-Segment elements, which are consists of a finite element node on one body and a surface element on the other domain. This section focuses on two points; (1) judgment and computation of the contact/separation, and (2) the constitutive law and its implementation which governs stick/slip.

Fig. 4.1 describes schematics of how to judge and compute the contact/separation in NTS elements. The gap is computed in the current configuration by the dot product between the outer normal vector of the segment and the position vector from the virtual contact point on the segment to the node. In case that the gap is positive, the NTS element is ignored since the node and the segment is separated; in case that the gap is negative, the NTS element is activated contact force is given as, by using penalty method, it is given by;

$$\mathbf{t}_N = \epsilon \mathbf{g}_N \tag{4.1}$$

where $\mathbf{t}_N$ is contact force in normal direction and ϵ is a penalty parameter which takes large value so that the overlaps between meshes are minimized. If the contact element is activated, it starts to update shear stress on the interface, as seen in Fig. 4.1. Here the penalty parameter is also employed to compute the shear stress as,

$$\mathbf{t}_T = \epsilon g_T^{stick} = \epsilon \left(\mathbf{g}_T - \mathbf{g}_T^{slip} \right) \tag{4.2}$$

where $\mathbf{t}_T$ is tangential stress and $\mathbf{g}_T^{stick}$ is an elastic tangential gap from a virtual contact point, which is like an anchor and the shear stress is computed by multiplication of the penalty parameter and the gap vector from the anchor point.

Once the shear stress violates a friction law, the virtual contact point shifts according to the slip rule, which is analogous to flow rule in terms of elasto-plasticity theory. This paper utilizes Mohr-Coulombs criterion since previous studies present that the criterion is applicable to the slip criterion for root-soil interfaces (Mickovski et al., 2011; Schwarz et al., 2011; Tomobe et al., 2016; Ji et al., 2018). The model can be expressed as an inequality constraint within the framework of the penalty method.

$$f = ||\mathbf{t}_T|| - \mu \cdot \epsilon \, ||\mathbf{g}_N|| - c < 0, \tag{4.3}$$

where f is the yield function, μ is the frictional coefficient, ϵ is the penalty parameter, and c is the cohesion. To update the frictional stress (Fig. 4.2), the return-mapping algorithm is applied. The algorithm was initially proposed by Simo and Taylor (1986) for updating stress. in the theory of elastoplasticity. The idea has been extended to computational contact mechanics as an algorithm for updating the frictional stress (Wriggers et al., 1990; Peric and Owen, 1992). Although the scheme is generally solved by iterative methods, it can be directly solved in the case of the Mohr-Coulomb model. The shear stress and the slip is explicitly updated by following equations.

$$\mathbf{t}_{Tn+1}^{tr} = \epsilon \left(\mathbf{g}_{Tn+1} - \mathbf{g}_{Tn}^{slip} \right) \ (f < 0) \tag{4.4}$$

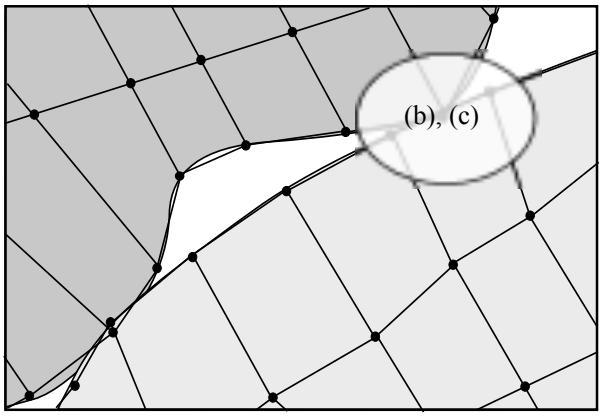

(a)

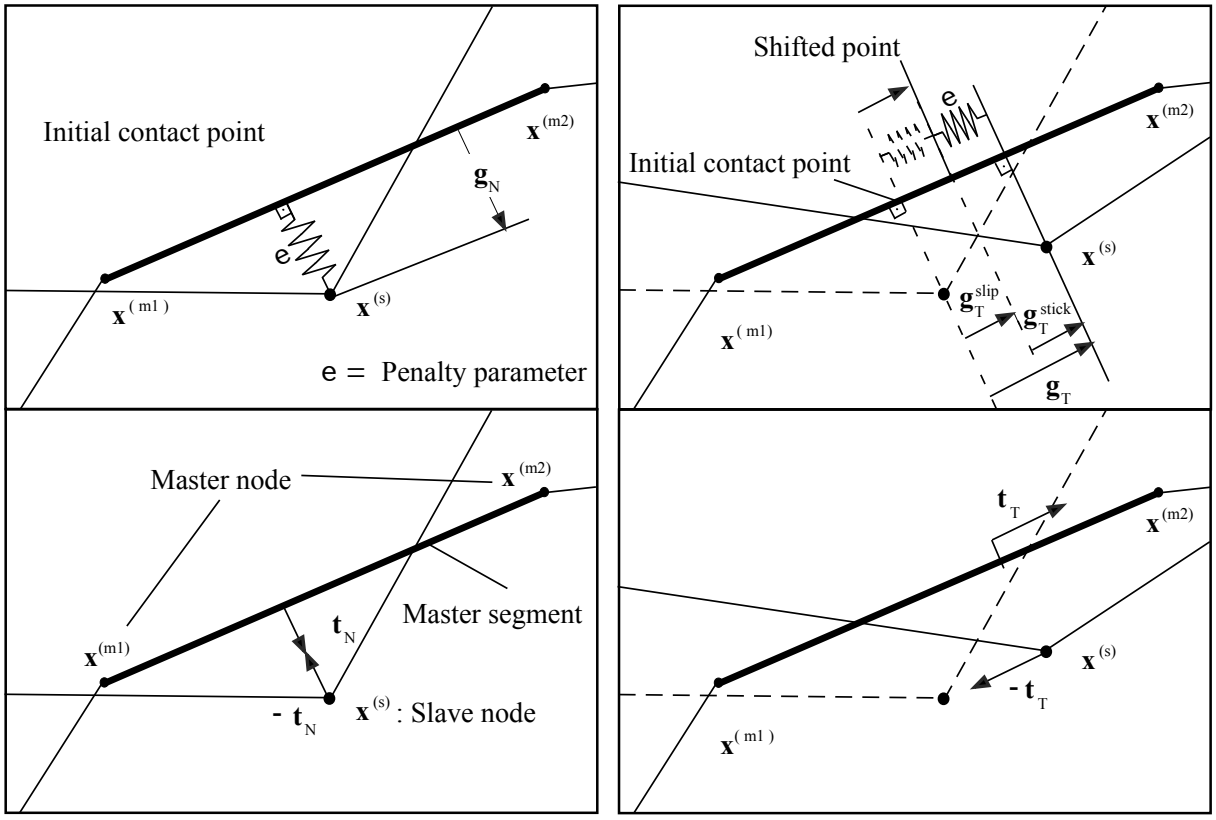

(b) (c)

Figure 4.1: Computation of contact/separation and stick/slip (a) Description of contact interfaces between two mesh objects, (b) Judgement of contact/separation and computation of contact stress towards normal direction, and (c) Schematics of stick/slip based on penalty method.

$$\mathbf{t}_{Tn+1}^{tr} = (\mu \cdot ||\mathbf{t}_{Tn+1}|| + c) \frac{\mathbf{t}_{Tn+1}^{tr}}{|\mathbf{t}_{Tn+1}^{tr}|} \; (f > 0) \tag{4.5}$$

$$\mathbf{g}_{Tn+1}^{slip} = \mathbf{g}_{Tn} \; (f < 0) \tag{4.6}$$

$$\mathbf{g}_{Tn+1}^{slip} = \mathbf{g}_{Tn} + (||\mathbf{t}_{Tn+1}|| - \mu \cdot ||\mathbf{t}_{Nn+1}|| - c) \cdot \frac{\mathbf{t}_{Tn+1}}{\epsilon \, ||\mathbf{t}_{Tn+1}||} \; (f > 0) \tag{4.7}$$

Here, $\mathbf{t}_{Tn+1}$ and $\mathbf{t}_{Nn+1}$ are the shear/normal stress at the time-step $n+1$, $\mathbf{g}_{Tn}^{slip}$ and $\mathbf{g}_{Tn+1}^{slip}$ are slips at time-step n and $n+1$, respectively; these equations are used in the flow chart in Fig. 4.2. The linearized equations are derived from momentum balance of the multi-body system, which is briefly reviewed in Wriggers (2006). The real problems are to mostly be modeled and simulated as a purely 3-D problem. The NTS formulation can also be applicable to the 3-D by pairing a node on one surface with a surface element on the other surface. The only difference is that the dimension of the surface is changed from 1 (line element) to the 2 (surface element). The basic formulations of the 3-D NTS formulation is also similar to the current formulation and visible in Wriggers (2006)

4.2.2 Avoidance of non-uniqueness problem for the NTS pairing in root-soil contact problems

Non-uniqueness problem of the pairing between a node and a segment is a critical problem for applying NTS approach to root-soil contact problems. It has been mentioned that a NTS element is not uniquely determined under some special cases as seen in the Fig. (4.3) (Wriggers, 2006; Zavarise and De Lorenzis, 2009): In this circumstance, there are two possible pairing for a node. It results in non-uniqueness of the gap, the contact force and shear stress, hence causes non-uniqueness of the solution for one simulation. This problem disturbs the solution especially in root-soil contact problems since root-soil interfaces are geometrically complex and, therefore, this circumstance is frequently appears. Further, there are a huge number of contact elements utilized in single problem, it means the number of possible solutions also diverges.

A simple and novel algorithm is introduced to guarantee the uniqueness of the NTS pairing as illustrated in Fig. 4.3, which was inspired by the base-line concept of Lius method(Liu et al., 2003). As the first step, for each slave node, the closest master node is detected. Then, the base-line is drawn between the neighboring nodes, as depicted in the figure. In Lius method, the base-line is utilized to compute the smooth virtual surface. In contrast, the current approach uses the base-line to draw another line that is perpendicular to the base-line and lies on the master node. This new line is denoted as a border-line which divides the master surface into two sides. Thus, a master segment on the same partition is

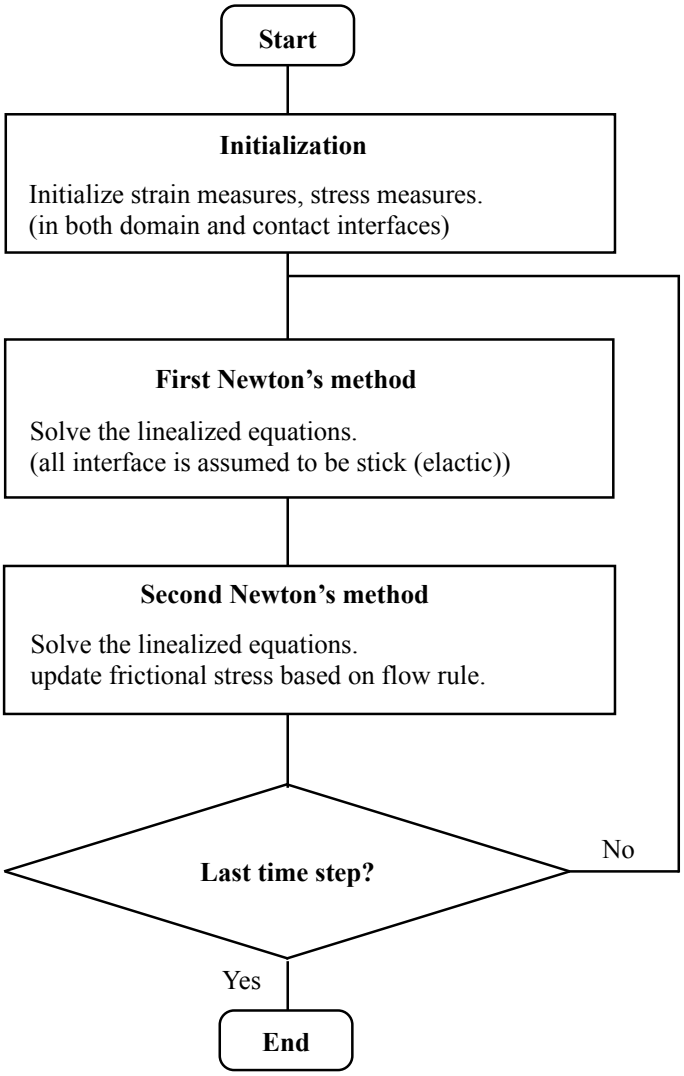

Figure 4.2: Algorithm of contact analysis: First Newton's method solves momentum balance by assuming that all interfaces are stick and no slips happen and second Newton's method updates the shear stress by using flow rules.

adopted as the master segment, as depicted. This process is numerically given by employing the following judgement function:

$$\alpha = \mathbf{b} \times \frac{\left(\mathbf{x}^s - \mathbf{x}^{m1}\right)}{||\mathbf{x}^s - \mathbf{x}^{m1}||} \tag{4.8}$$

where $\mathbf{b}$ is defined as a unit vector which is perpendicular to the base-line, $\times$ means the cross product operator, $\mathbf{x}^{m1}$ and $\mathbf{x}^s$ are a master and a slave node, respectively, and α is the judgement function. If α is zero or positive, the master segment on the right side is adopted; otherwise, the one on the left side is adopted. This algorithm increases the robustness in some cases, as will be demonstrated in the next subsection.

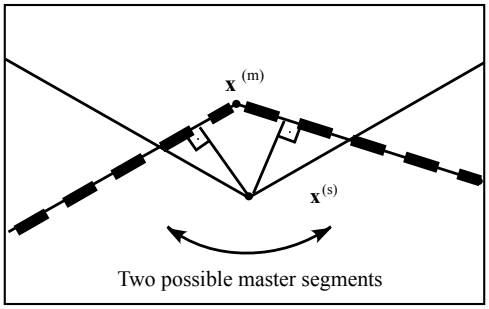

(a)

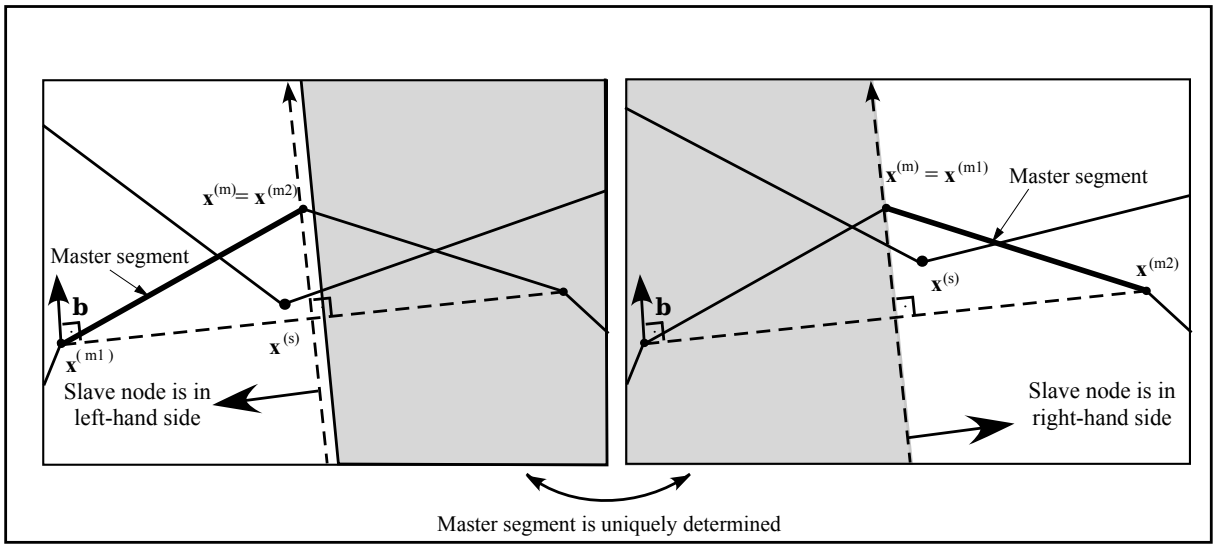

(b)

Figure 4.3: Schematic of proposed method to determine unique pairing: (a) Typical non-uniqueness problem of NTS elements and (b) Proposed method to avoid non-uniqueness of pairing, where master segment is determined for every slave node using base-line.

4.2.3 Validation of simulation code by press-fit problem

The stabilization algorithm presented in the previous subsection is compared with the original NTS algorithms to evaluate the effect of the stabilization scheme. The stabilization scheme in the last subsection is examined through the press-fit problem which is a widely-known benchmark of its kind. The problem simulates the extrusion process of an elastic block as shown in Fig. 4.4. The solution oscillates or diverges during the elastic body pass through an extraction die (Fig. 4.4). Wriggers et al. (2001) present that the problem can be robustly solved by using the C1-interpolation scheme which introduces smooth virtual surfaces in the master body, and Liu et al. (2003) utilized the problem to demonstrate the effect of the algorithmic stabilization. This subsection evaluated the effect of the current modification through the comparison with these studies. In the press-fit problem, a rubber plug is pushed into a steel channel as illustrated in Fig. 4.4. Due to symmetricly about the vertical axis of both geometry and boundary conditions, this section utilizes the lower half of the system. The mesh model and the boundary conditions are depicted in Fig. 4.5, which is discretized by using four-node elements. The force-displacement relationship on the left side of the rubber is plotted for the comparison among ones of the previous cases. The constitutive model of the materials is supposed to be the modified neo-Hookean model proposed by Vladimirov et al. (2008, 2010), which have been applied for rubbers and metals (Wriggers, 2006; Hashiguchi and Yamakawa, 2013). This constitutive model is almost the same as the neo-Hookean model which is used in Wriggers et al. (2001) and the St. Venant model in Liu et al. (2003). The material parameters are identical with these cases.

The deformed mesh is depicted in Fig. 4.6, which is consistent with the results of the previous results. As can be seen in the interface of the rubber and the steel channel, the overlap between those domains is successfully minimized. This result indicates that the non-penetration condition between the two bodies is precisely implemented.

Fig. 4.7 shows the force-displacement relationships of the current and the previous approaches, in which the rubber block contacts the edge of the steel channel during the displacement is 30.0 mm to 90.0 mm. The oscillating behavior is appeared in the process, which is induced by the non-smoothness of the NTS approach. The oscillation in the current results are more moderate than one of the non-stabilized NTS approach of Liu et al. (2003), and the profile is almost the same as one of Wriggers et al. (2001). Hence, it is indicated that the non-uniqueness problem of the master-slave pairing can disturb the convergence of the NTS approach and that the current method can improve the robustness by avoiding the problem. However, the current approach is less smooth than other stabilizing approaches, which confirms that the smooth interpolations are more powerful.

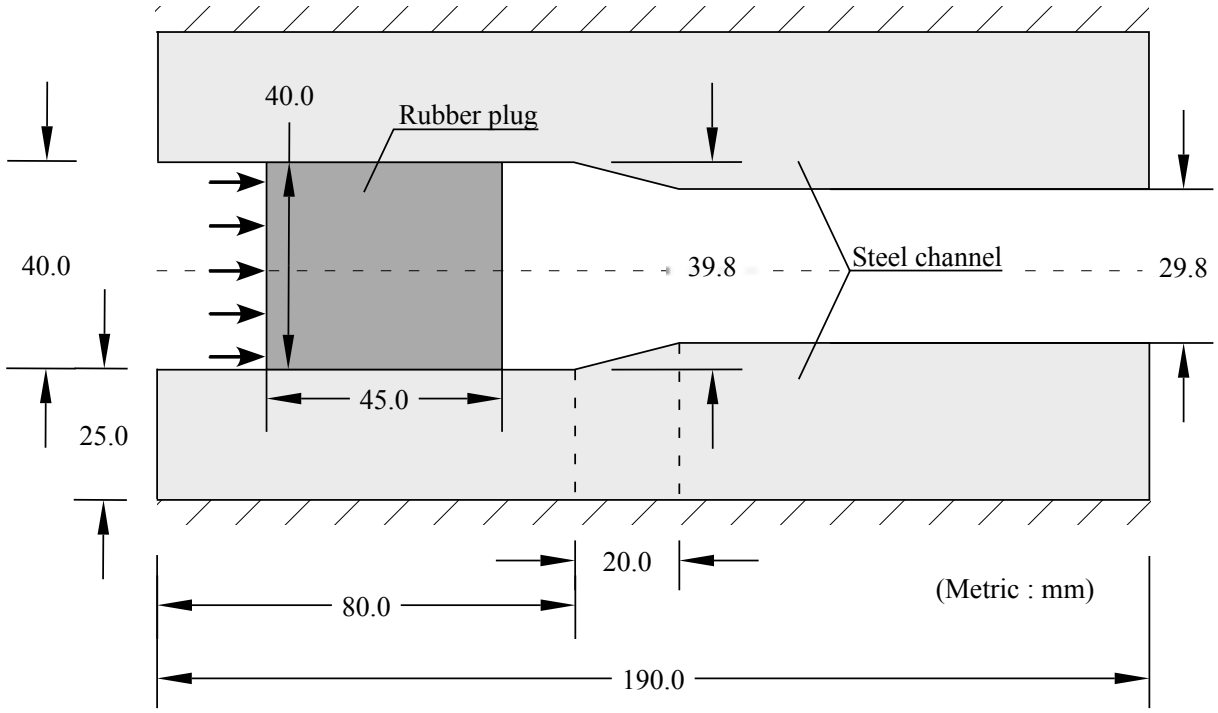

Figure 4.4: Schematics of the press-fit problem (Wriggers, 2006) in which a rubber plug is passing through a steel channel.

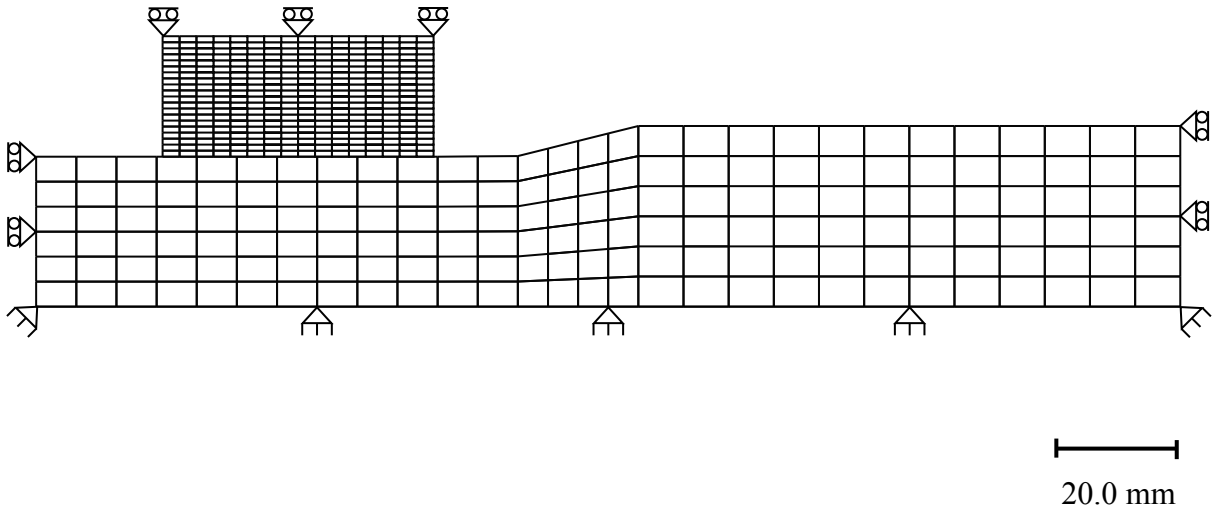

Figure 4.5: Mesh and initial condition of the press-fit problem.

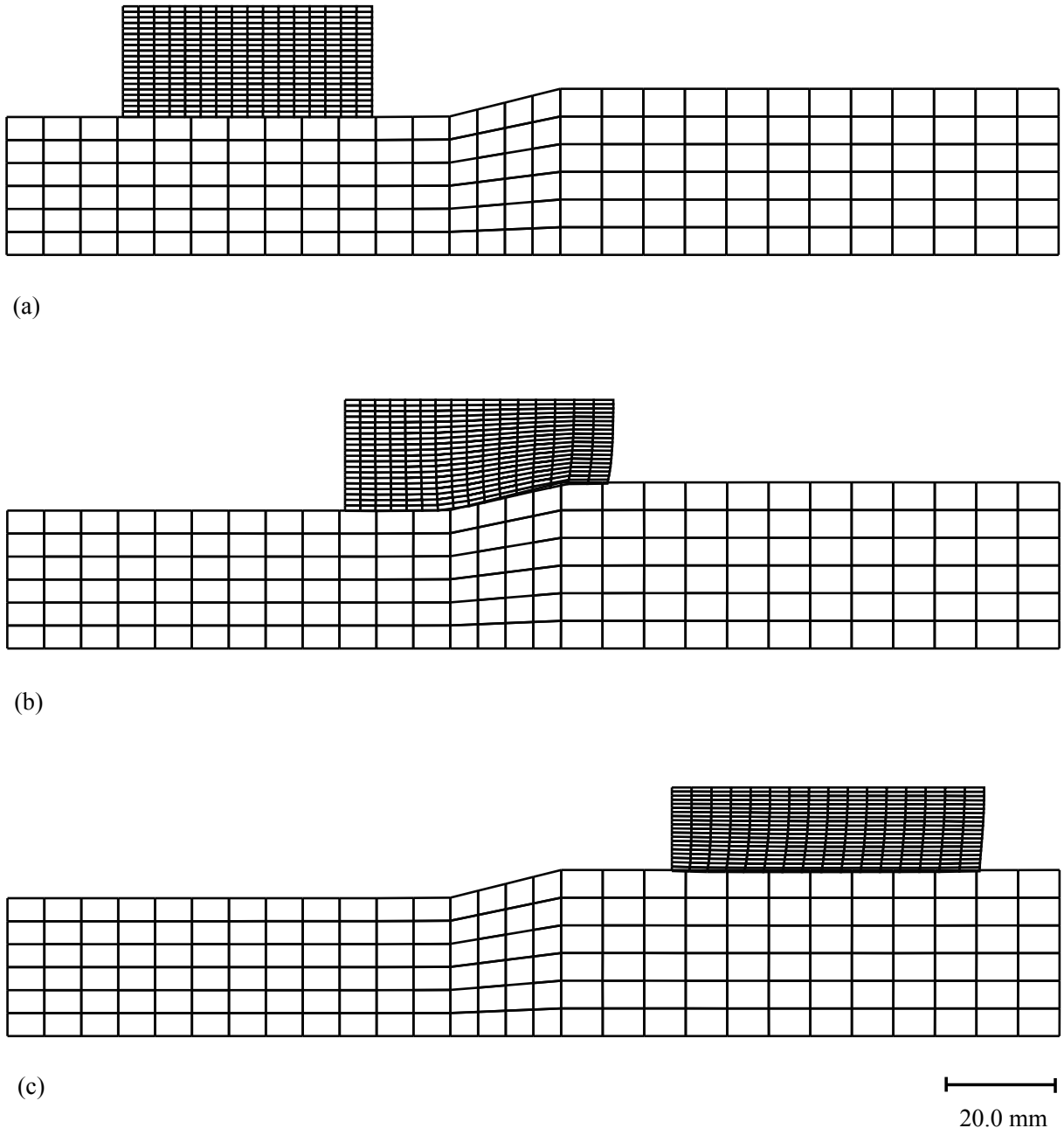

Figure 4.6: Deformed mesh simulated by the modified NTS approach in which the total displacement is (a) 0.0 mm, (b) 5.0 mm, and (c) 100.0 mm.

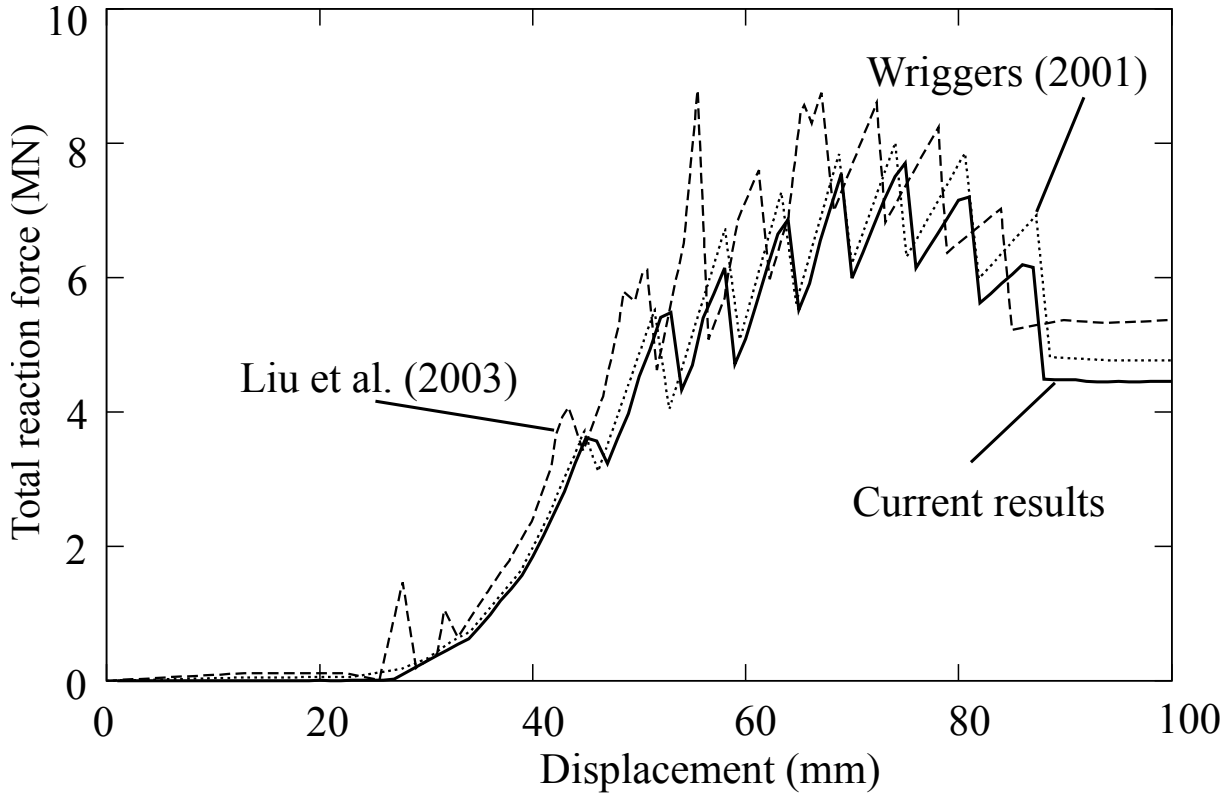

Figure 4.7: Relationship between displacement and total reaction force on the left side of the rubber plug in cases of Wriggers (2001), Liu et al. (2003), and the current result.

4.3 Material model and mechanical tests for root, soil and interface

4.3.1 Model and parameters of soil

The neo-Hookean hyperelastic model (Vladiminov, 2008, 2010) is utilized in terms of finite strain theory, and material parameters of soils which are used in this simulation are measured based on the method of unconfined compression test of soils. The constitutive model and the soil test are chosen for two reasons

- The soil is in low-confining pressure condition, and it is challenging to measure and model rheological properties of soils under the conditions. Hence, this paper does not focus on this point and employs the possible simplest constitutive model
- The neo-Hookean hyperelastic model only necessitates the measurement of two material parameters, Youngs modulus, and Poissons rate. Youngs modulus under low-confining pressure can well be measured by using the unconfined compression test of soils.

On the other hand, Poissons rate is measured by using a compression test described below. Preliminary, the Mohr Coulomb Drucker-Prugger (MC-DP) constitutive equation are implemented within the framework of Finite Strain theory based on the multiplicative decomposition of deformation gradient tensor (Hashiguch and Yamakawa, 2011). Although the model can simulate the shear behavior of both roots and soils, it is difficult to get numerical solution when it is combined with Node-To-Segment Approach and applied for root-soil contact problems presented in this paper. This ill-convergence problem in root-soil contact problems is also reported by Dupuy et al. (2007) and in order to get convergence, they used rigid root-soil interfaces. Since this paper focuses on providing accurate implementation of root-soil interfaces, the application of the NTS scheme with the elasto-plasticity model for root-soil contact problem is remained for future studies.

Prior to the mechanical tests, the soil is sampled from a paddy field located in Maibara City, Shiga Prefecture, JAPAN in 2018, and the natural density and the water content of the soil are measured. The sampling is conducted for the top soil layer (0 to 30.0 cm depth) and put through a 2.0 mm sieve. By using the soil, the natural density, the water content, soil particle density, sand fraction content and fine fraction content are measured. The properties of the soil is visible in Table 4.1 and the soil is classified as FS (JGS-0051-2009).

The material parameters, Youngs modulus and Poissons ratio are measured by unconfined compression tests (JGS-0511-2009) and consolidation tests. The specimen for the unconfined compression test is made by following procedure. First, the disturbed soil is hydrated so that the water content of the soil specimen is 29.99 % which is same as one

Table 4.1: Properties of soil.

	Protocol	Value
Soil particle density (g/cm^3)	JGS 0111-2009	2.79
Bulk density (g/cm^3)	JGS 0191-2009	1.73
Water content (%)	JGS 0121-2009	29.99
Sand fraction content (%)	JGS 0135-2009	24.37
Fine fraction content(%)	JGS 0135-2009	75.63
Classification	JGS 0051-2009	FS
E50 (kPa)	JGS 0511-2009	1618.8

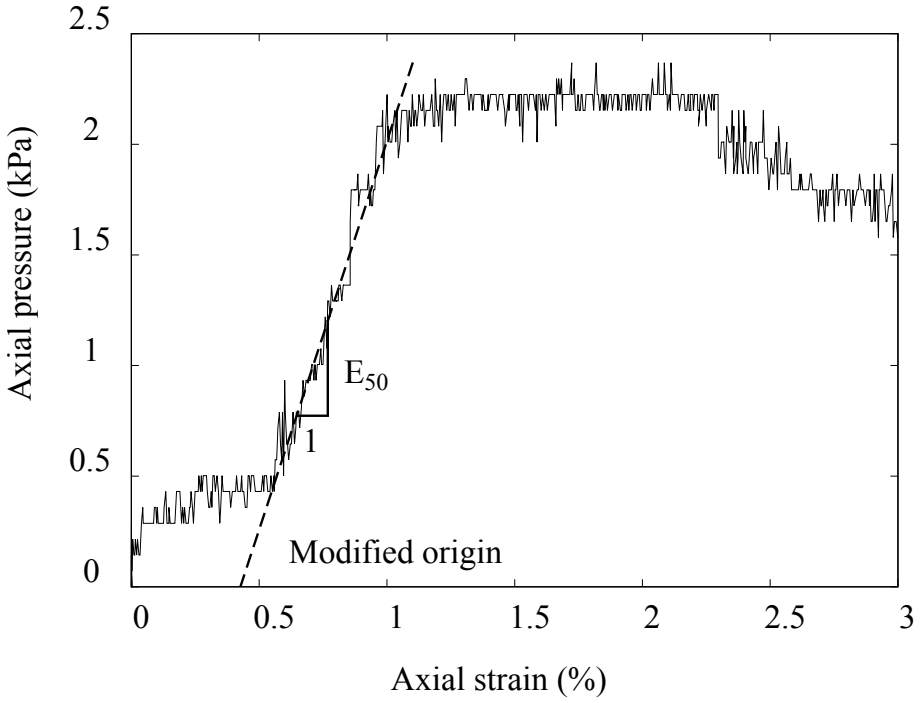

Figure 4.8: Results of the unconfined compression test.

measured by the sampling. Then the soil is put into a mold and compressed so that the water content and the natural density of the specimen is same as ones of the field condition. The stress-strain relationship of the unconfined compression test of soils are shown in Fig 4.8. Conforming to the standard, the value (1,618.8 kPa) is obtained by the relationship. This section utilize the value as a Youngs modulus of the soil since the value can be seen as Youngs modulus during the axial strain is small (less than 1.0 %). Utilizing the same soil, the Poissons ratio of the soil are measured by using equipment described as Fig. 4.9. The equipment loads stress on the axial direction and measures horizontal pressure by using a soil pressure gauge, and the Poissons rate is estimated by the relationship,

$$\frac{\sigma_h}{\sigma_v} = \frac{\nu}{1-\nu} \tag{4.9}$$

where ν is the Poissons rate, σ_v and σ_h are vertical/horizontal stresses, respectively. The relationship between vertical/horizontal stresses of which is presented in Fig 4.9. The result shows that the Poissons rate is estimated as 0.28.

4.3.2 Model and parameters of root

The Neo-Hookean model is also used for the root domain, and bending tests measure Young's modulus of the root. The root is sampled from a soybean plant grown under an artificial environment, the variety of which is UA4805. The soybean is firstly germinated on a wet tissue under 25 degrees, and planted onto a soil-box and grown under LED lights for 96 hours. The root of the soybean plant is shown in Fig. 4.10. The primary root surrounded by a rectangular is cut off, and a segment of a root is obtained with no branches and the diameter of which is the almost constant. The schematics of the bending tests are visible in Fig. 4.10, where the left side of the root segment is fixed, and weights are loaded at the right side. The tests were repeated under four different weight and, from the displacement-force relationship, Youngs modulus is given by the following equation.

$$E = \frac{PL^3}{3uI} \tag{4.10}$$

where, E is Youngs modulus, u and P are the displacement and the force loaded on the right end, I is the second moment of area, L is the length of the root segment. As a result, Youngs modulus is 34,920 kPa. As for the Poissons ratio of the root, few references are available and it is difficult to measure, hence the Poissons ratio of the fresh tissue of apples measured by Kim et al., (2008) is referred. They presented that the Poissons ratio of it is 0.23 to 0.28, then, for simplicity, the 0.28 is chosen. It is worth noting that few change is observed in following results due to the choice of the Poissons ratio of roots in the range of 0.23 to 0.28.

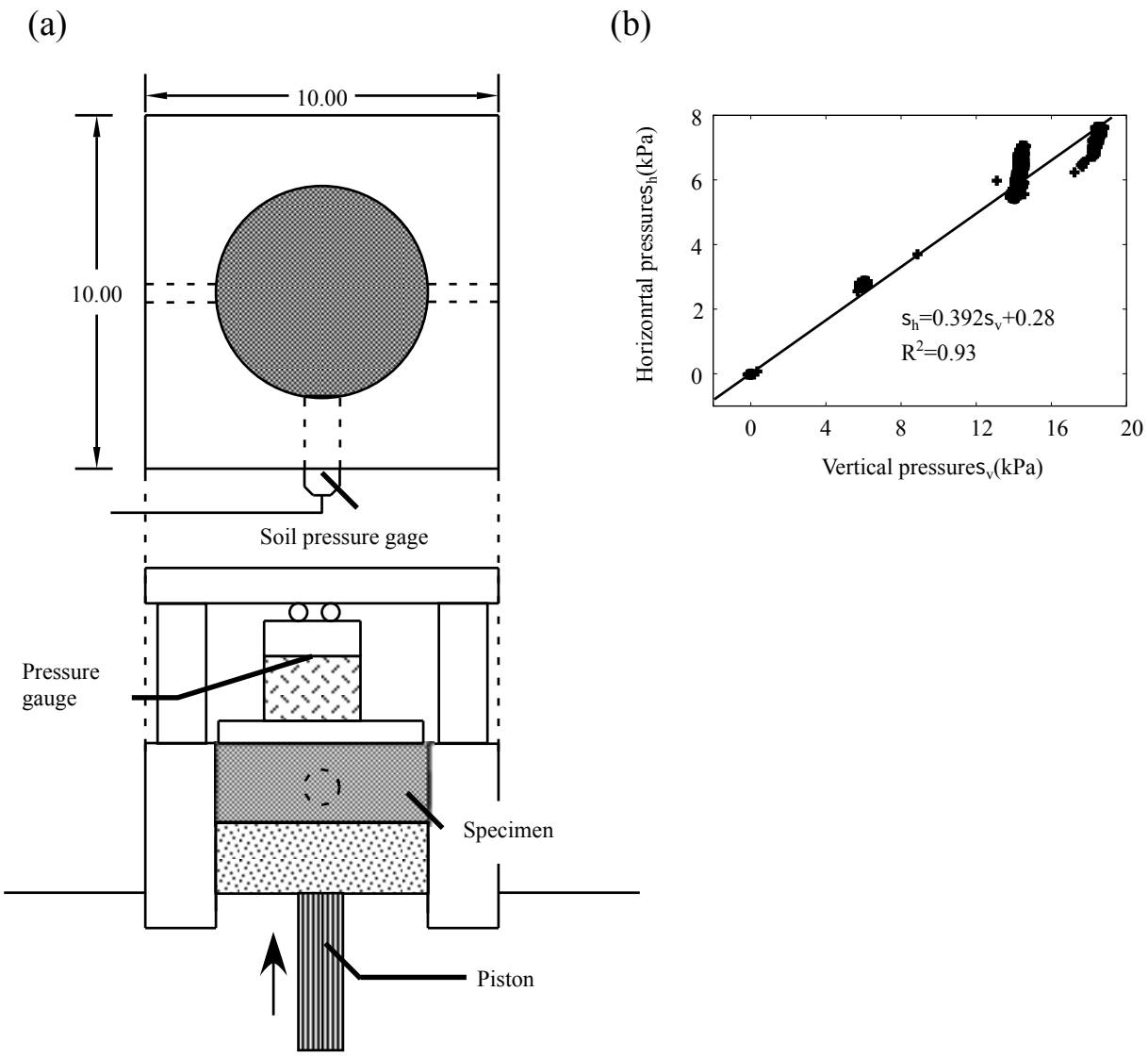

Figure 4.9: Apparatus for measurement of Poisson's ratio and the results.

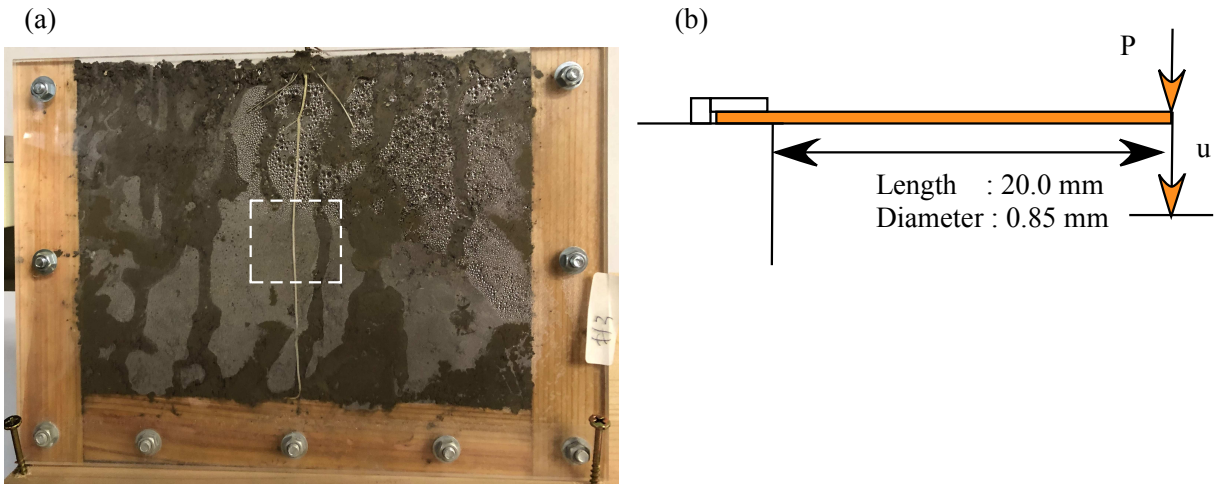

Figure 4.10: Schematics of bending test to measure Young's modulus of a root: (a) Image of soil-box and root used in bending test and (b) Schematic of bending test and properties of root segment.

Table 4.2: Material parameters of roots, soils and root-soil interfaces utilized in simulation.

	Young's modulus (kPa)	Poisson's ratio	Penalty parameter (kPa/m)	Frictional coefficient	Cohesion (kPa)
Root	34920.0	0.28	-	-	-
Soil	1618.0	0.28	-	-	-
Root-soil interface	-	-	300000.0	0.4716	0.767

4.3.3 Cohesion and frictional angle of root-soil interface

The interfacial parameter, cohesion and frictional angle, are determined according to Tomobes pull-out tests (2016). The method is chosen since it can measure the friction coefficient and cohesion of root-soil interfaces under unconfined condition. The detail of methods and results of the test is described with its numerical simulation in the next section and the friction coefficient and cohesion are shown in Table 4.2.

4.4 Experiment and simulation of pullout test

Prior to simulate the real-scale problem, the current approach is validated under simple geometrical condition by simulating pullout tests of root from soil. The simulation is compared with the experiment of Tomobe et al. (2016) since the current approach can measure the exact friction coefficient and cohesion by using the pullout tests.

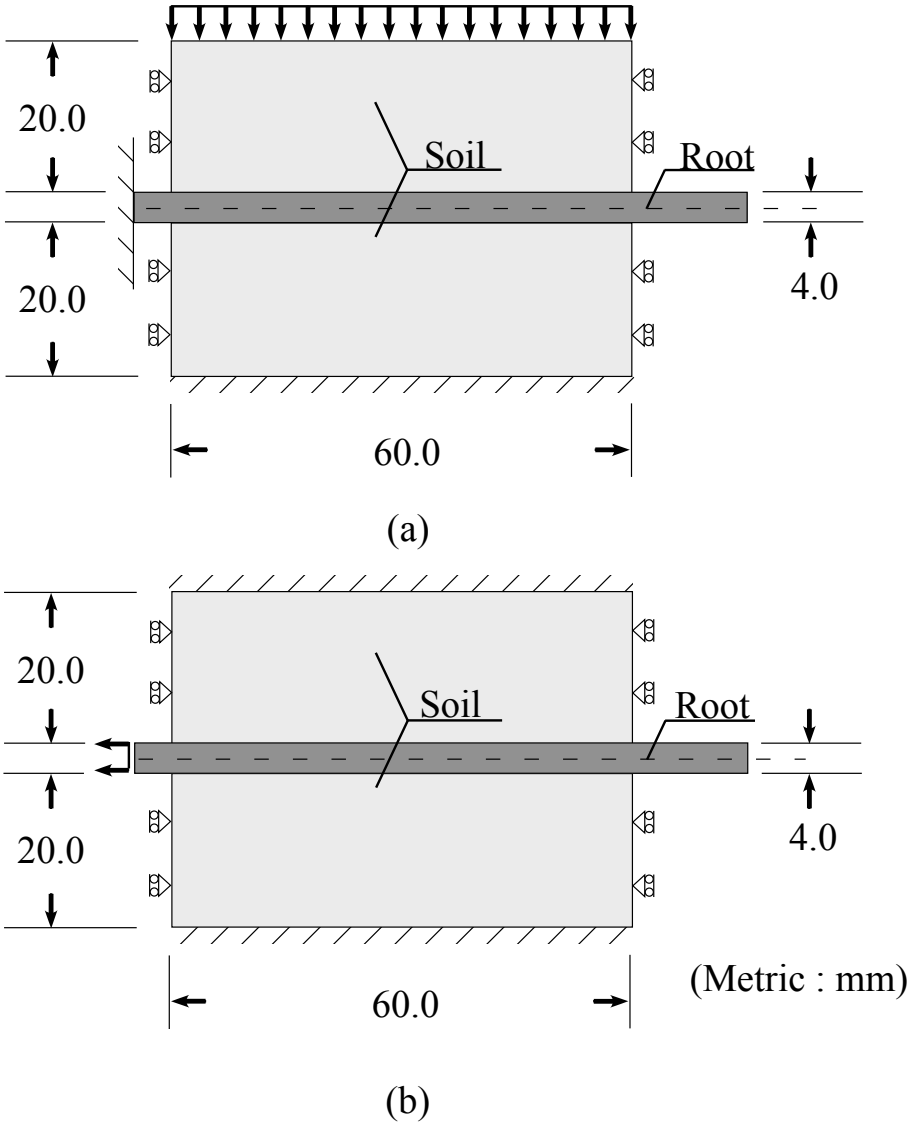

Figure 4.11: Plan view of pull-out tests: (a) soil is vertically compressed prior to the simulation, and (b) root is pulled out towards left side, and during pull-out process, top and bottom surfaces are fixed.

The pullout problem measures the shear strength of the root-soil interfaces by pulling out a root segment from a soil specimen under constant normal pressure, a brief description of which is given in Fig. 4.11. At the beginning of the experiment, a soil specimen is

set in a steel column, and the root is horizontally penetrated through the soil. Then, a prescribed pressure is loaded by pushing down on the upper wall and the root is statically pulled out from the specimen until the displacement reaches more than 10 % of the width of the specimen. During the pullout stage, the displacement (mm), the horizontal reaction force (N), and the horizontal soil pressure (kPa) are recorded, and the normal and frictional stresses on the root-soil interfaces (kPa) are estimated from these data using the equation of Tomobe et al. (2016). The tests are repeated under four different vertical pressures; for four cases, the vertical pressures are 0.5 kPa, 1.0 kPa, 1.4 kPa, and 2.3 kPa.

4.4.1 Material and method of pullout test

Fig. 4.12 illustrates the mesh and the boundary conditions of the numerical simulation. The experiment is actually carried out under contact boundary condition, which indicates that a rigid wall is pressed by constant stress. In order to realize the condition in the numerical simulation, the boundary condition is given as displacement boundary condition where equivalent horizontal displacement is loaded. As can be seen, four-node elements discretize the model and only a half system is modeled, as depicted, due to the symmetry about the horizontal line. The root segment has approximately the same length (80.0 mm) and radius (2.0 mm) as the tests. The left side of the root is displaced until the displacement is more than 10 % of the width of the specimen (Fig. 4.12). The pullout process is divided into 200 time steps and is supposed to be in the pseudo-static condition. In each time step, the displacement and the total reaction forces on the left side of the root and the top of the soil are recorded, and the average of the stresses is computed by dividing the total forces by the contact area.

In order to verify the frictional behavior of the numerical simulation, the constitutive models and the material parameters for the interfaces and the bodies are selected in the following way. The Mohr-Coulomb model is employed for implementing the friction and the cohesion at the interfaces, and the material parameters are installed from the experimental results seen in Table 4.2. Therefore, it is expected that the root-soil interfaces slip when the shear stress exceeds the criterion of the Mohr-Coulomb model. Through the numerical simulation, the overlapping of the root and the soil is minimized, as presented in Fig. 4.13. Here, deviatoric stress q is computed for each Gaussian point using Eq. (4.11).

$$q = \sqrt{\frac{3}{2}\left(\sigma_{ij} - p\delta_{ij}\right)\left(\sigma_{ij} - p\delta_{ij}\right)} \tag{4.11}$$

In the equation, σ_{ij} is the Cauchy stress tensor and δ_{ij} is the unit tensor. The contour plot of the distribution of deviatoric stresses is mostly static during the test, which is consistent with the friction law. Fig. 4.13 shows the distribution of deviatoric stresses; the values on and around the root-soil interfaces are relatively large compared with the other parts, which qualitatively suggests that both friction and cohesion resist the pullout force.

4.4.2 Comparison between experiment and simulation

The relationship between displacements and frictional stress during the pullout process is illustrated in Fig. 4.14, which shows that the simulations are similar to the experimental results. At the start, the frictional stress increases along with the increase in displacement at an almost constant rate. After the frictional stress reaches the frictional strength, the global slip starts and the frictional stress maintains an almost constant value for each case. The result also shows that the shear stress during the slip phase are similar to the experimental

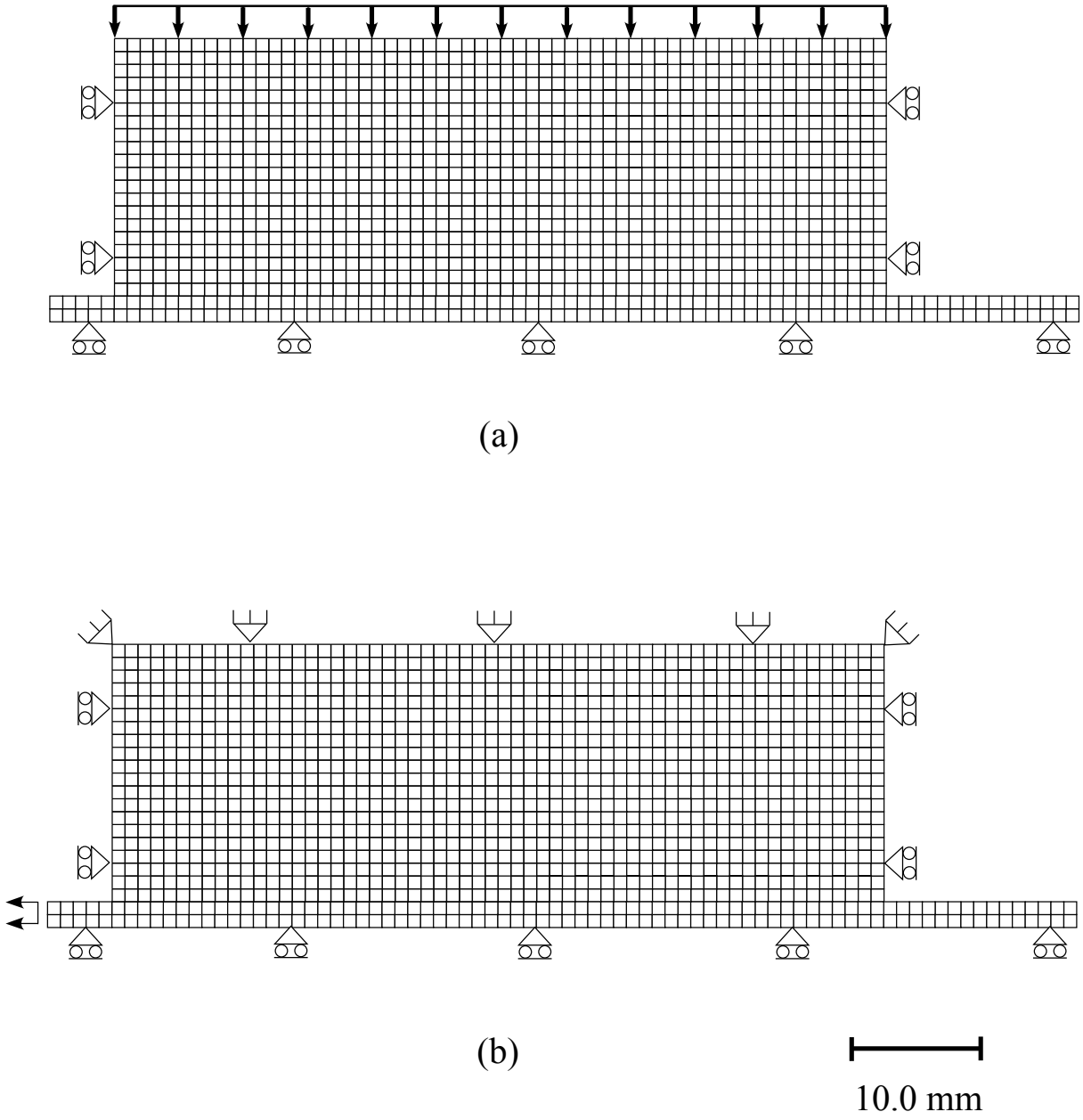

Figure 4.12: Mesh and boundary conditions of pullout tests: (a) prior to simulation, initial stress is loaded to reproduce experimental conditions. (b) The topsoil is vertically fixed during the pullout simulation.

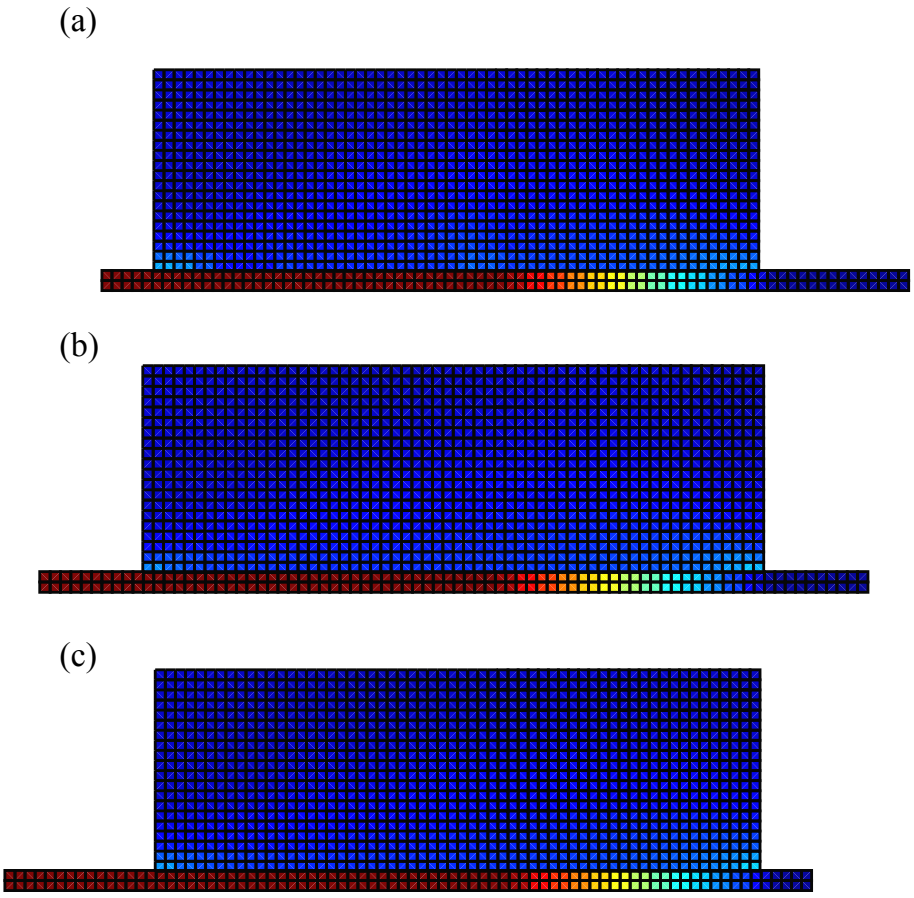

Figure 4.13: Contour plots of deviatoric stress when horizontal displacement is (a) 0.1 mm, (b) 5.0 mm, and (c) 10.00 mm.

data. Although the angle of the initial curve is different, the difference is un-controllable since it is governed by the penalty parameter which is not material parameters. On the other hand, the simulated behavior is too stiff compared with the experimental results when the displacement is small (stick), which cannot be controlled as material parameter since the value should be enough large: The limitation is determined by the penalty formulation. In addition, since the Mohr-Coulomb model cannot model softening, the simulation is stiffer than the experiment at the post-slip part.

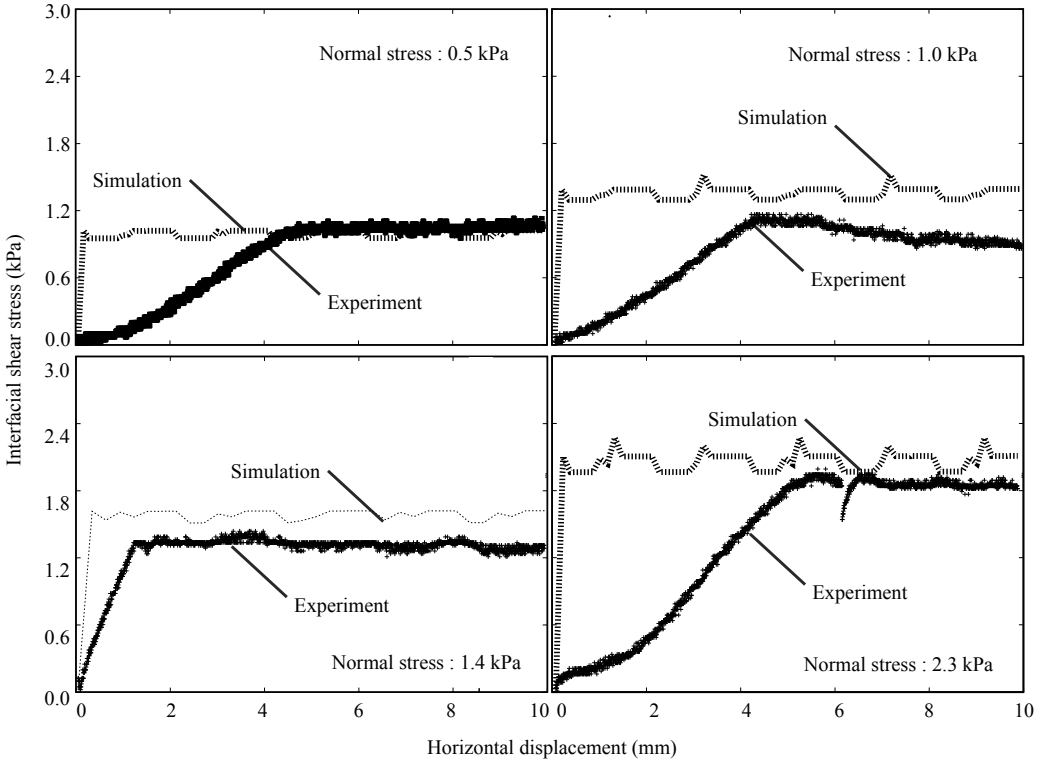

Figure 4.14: Relationship between horizontal displacement of root and interfacial shear stress for each stress condition.

The Mohr-Coulomb model is precisely satisfied as illustrated in the relationship between the normal and the frictional stresses in Fig. 4.15, since the stress point lies on the criterion while the root slips. Furthermore, the maximum frictional stresses are also identical to those of the experiments. Hence, it is indicated that the friction and the cohesion of root-soil interfaces can be consistently expressed through the use of the NTS approach. Overall, the above results indicate that the numerical method can accurately predict the cohesion and the friction of root-soil interfaces and that the predicted stress-displacement curves are similar to the experimental results. Therefore, the current approach is capable of estimating the mechanical behavior and the shear strength of root-soil interfaces in, at least, geometrically

simple cases.

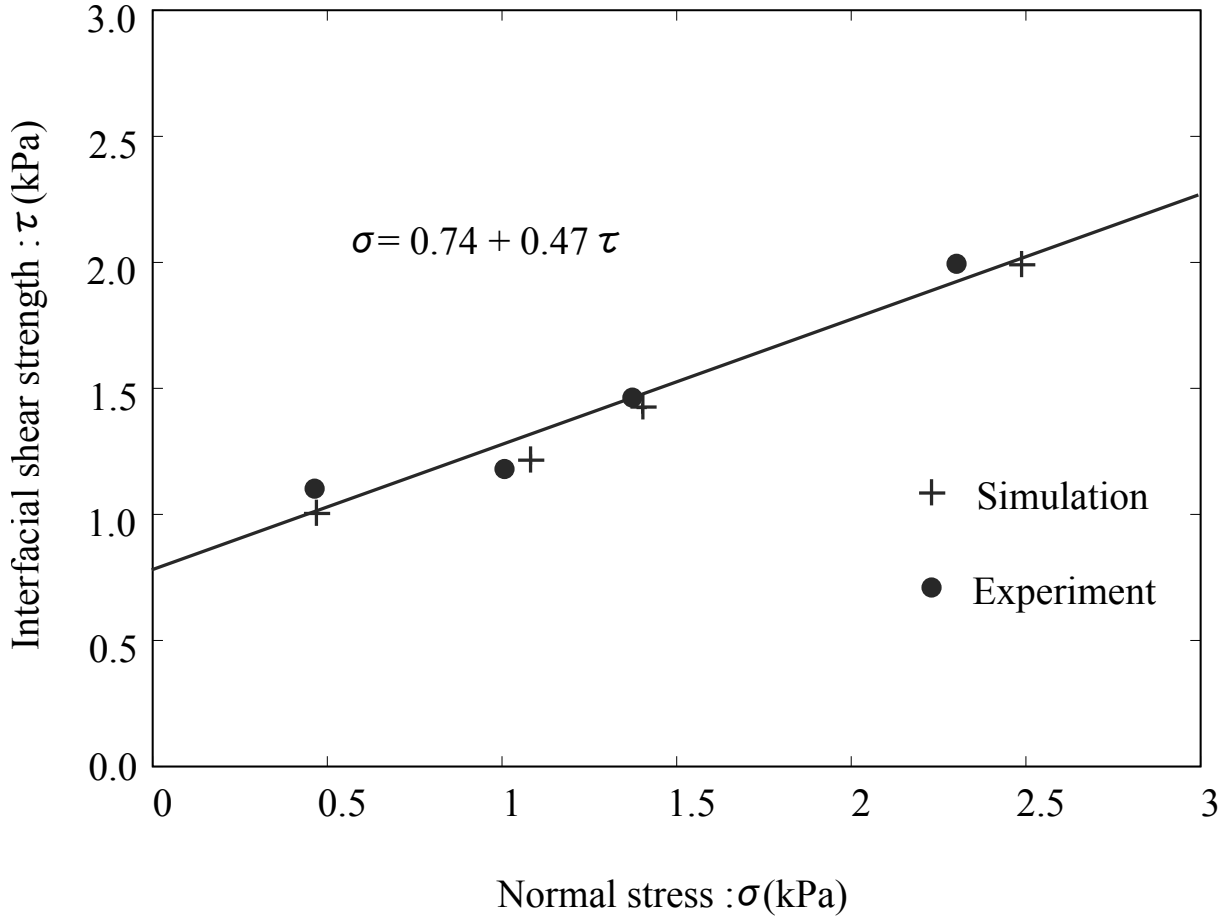

Figure 4.15: Relationship between normal stresses on root-soil interfaces and interfacial shear stress of experiment and current simulation.

4.5 Experiment and simulation of 2-D lodging problem

4.5.1 Motivation and background

This section simulates the 2-D lodging problem, which is a pile-loading tests for roots under 2-D condition. The lodging tests are usually conducted under 3-D condition as presented by Berry et al. (2003) and utilized for many cases (Berry et al., 2004; Baker et al., 2014), however, for simplicitys sake, this section conducts similar tests under a 2-D condition by using a thin soil box.

4.5.2 In-situ lodging experiment

There are two reasons to use the 2-D approximation in the present section. It is worth noting that the current experiment is not perfectly 2-D condition since the shape of roots is not rectangular but a round shape. Although the 2-D simulation is approximation of 3-D simulations it has some important benefits. The primary benefit is that the computational and experimental cost is far littler than 3-D simulations, thereby, more investigations can be done. Such the results of 2-D simulation will also contribute to understand root-soil mechanical interactions. Another reason of using 2-D simulation is that it is conventional that the 2-D simulation is used for validating the fundamental behavior of numerical simulation when the simulation is applied for unconventional use. For instance, numerous numerical simulation of root-soil interaction are modeled in terms of 2-D (Baker et al., 2014). Since the present thesis focuses on the applicability of the NTS scheme for root-soil interactions, the 3-D investigation is remained for future studies.

The soil is filled into the thin soil box as shown in Fig. 4.16. The soil box is consists of front/back acrylic panels and wood spacers. The width of the gap between the two panels is 1.0 mm, which is almost the same as the diameter of the primary roots of soybean as mentioned below. Therefore, the growth of the roots can be observed without disturbing soils. The soil is filled as following procedure: Before putting the soil into the soil box, the box is laid down, and the front panel is detached. Then, the soil is uniformly pasted on the back panel, the thickness of which is also 1.0 mm. It is worth noting that the acrylic panels are so smooth that the soil can easily slips on them and the friction between the soil and the panel is very small. After that, the front panel is attached, and the soil box is erected. A Germplasm of soybean is planted on the soil box and is grown for 96 hours under 25 Celsius degrees as seen in Fig. 4.16. A variety of the soybean used in the test, UA4805, is the same variety as the previous experiments and the diameter of the primary root of that variety is about 1.0 mm, which is almost the same as the gap of the soil box. The seed is germinated on a wet tissue for 48 hours under 25 Celsius degrees until the length of the primary root reaches 5.0 mm. After the germination, the soybean is planted on the upper and middle side of the soil box. The soybean is grown for 96 hours until the primary leaf expands and, during that, the wood spacer is kept wet to prevent drying of the soil.

Description of setup of presented 2-D lodging experiment: (a) Soybean plant is grown under artificial condition for 96 h and (b) Root is pulled from left side and reaction force is recorded by load-cell.

The soybean root is pulled to the left side of Fig. 4.16 and both displacement (mm) and reaction force (N) is recorded during the test. Prior to the test, the shoot of the soybean plant is cut off before the loading test to measure the pure reaction force of root. The loading speed is 0.1 mm/min and the total displacement is 2.0 mm, at which slip and separation in the root-soil interfaces are appeared and the rhizosphere is globally deformed. In order to

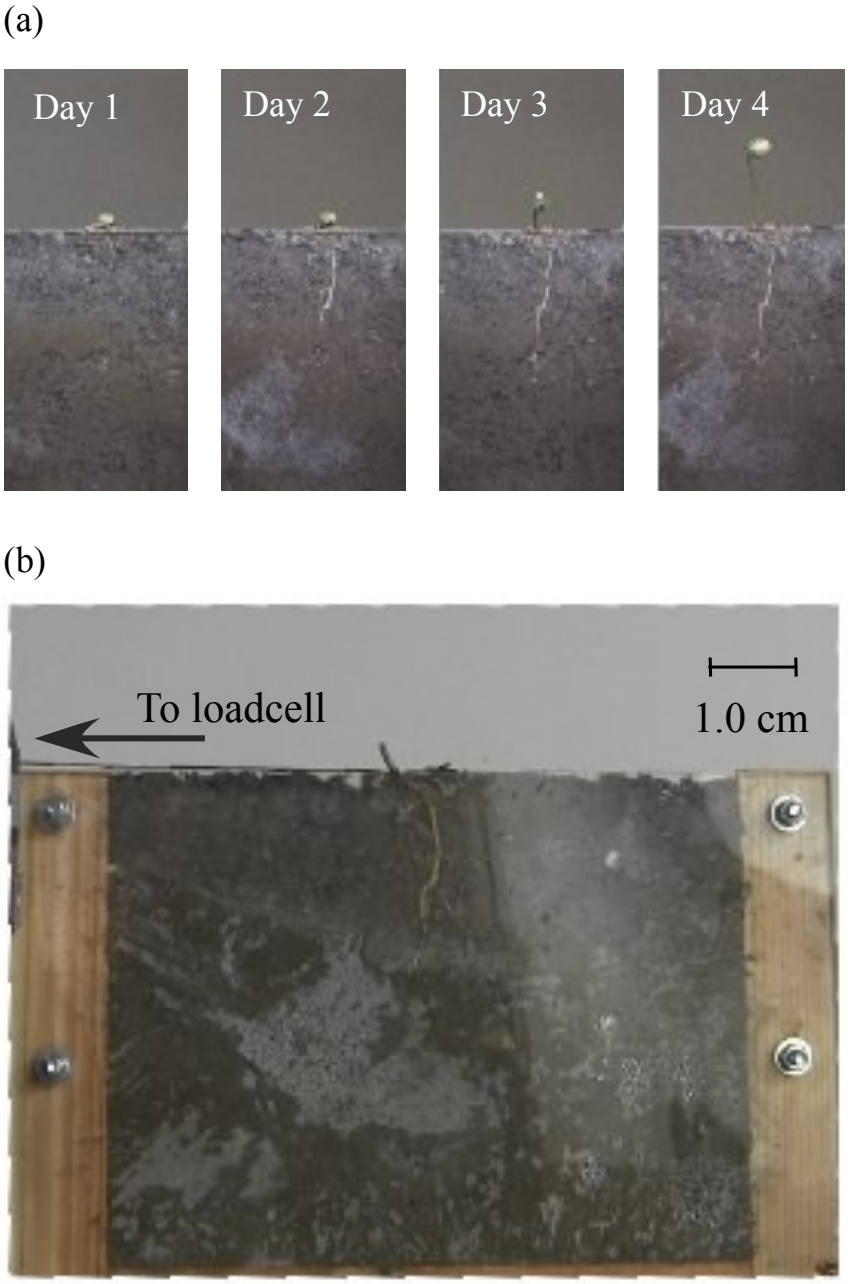

Figure 4.16: Description of setup of presented 2-D lodging experiment: (a) Soybean plant is grown under artificial condition for 96 h and (b) Root is pulled from left side and reaction force is recorded by load-cell.

measure the reaction force, an extremely sensitive force gauge (LUX-B-50N-ID, KYOWA) is adopted since the reaction force are supposed to be very small, less than 50.0 N.

After the test, the root is carefully put back to its initial position and softly washed out by using a spray and the root morphology is scanned by using a digital camera (Fig. 4.17). It is difficult to accurately scan the root morphology before the experiment since fine soil particles covers considerable part of the root. Thereby, the root morphology is scanned after the loading process as following: First, the soil box is raid and front panel is detached. Second, the impression of the root on the soil is traced to figure out the initial position. Third, the root is softly and slowly put back to its initial position, sprayed to wash out the soil particles and scanned by using a camera.

4.5.3 Mesh generation and boundary conditions for simulation

The mesh for the FE analysis is generated by using Python Imaging Library (PIL) and Gmsh as following way. First, the scanned data (Fig. 4.17) is painted in different color for the root and the soil as shown in Fig. 4.17. Then the posterized image is filtered by using a Laplacian filter implemented by PIL to get pixels on the outlines of both the root and the soil. The outline of the root and the soil is traced by connecting these pixels and unnecessary pixels are cut out to reduce the data-size. This outline is exported as .geo format of Gmsh that is an open-source software for pre-post-processing for FEM analysis. Gmesh generates mesh for FEM analysis from .geo format as can be seen in Fig. 4.17, where the Delauney triangulation algorithm is utilized in this case. The mesh of the root and the soil are generated separately as this figure, and put into same field as shown in Fig. 4.17. As can be seen in Fig. 4.17, the root architecture is precisely reconstructed into a 2-D root model for the simulation: The number of nodes are 10,348, the number of elements are 10,000 and the number of NTS elements are about 500. Compared to the LE approach, the current approach is more accurately expressing the root morphology by using such the high-resolution mesh. Furthermore, the separation and slip are evaluated in 500 locations, which cannot be performed by using NTN approach. Boundary conditions are seen in Fig. 4.17. The left and right sides of the soil domain is fixed for the horizontal direction and the bottom of the soil domain is fixed for the vertical direction to realize the similar conditions as experiment. On the root domain, a horizontal displacement is loaded towards left sides over 2.0 mm, which is the same condition as the experiment. The total displacement is loaded over 50 time-steps to get accurate solutions. For both of the root and the soil domain, the material parameters are given as mentioned in the previous section.

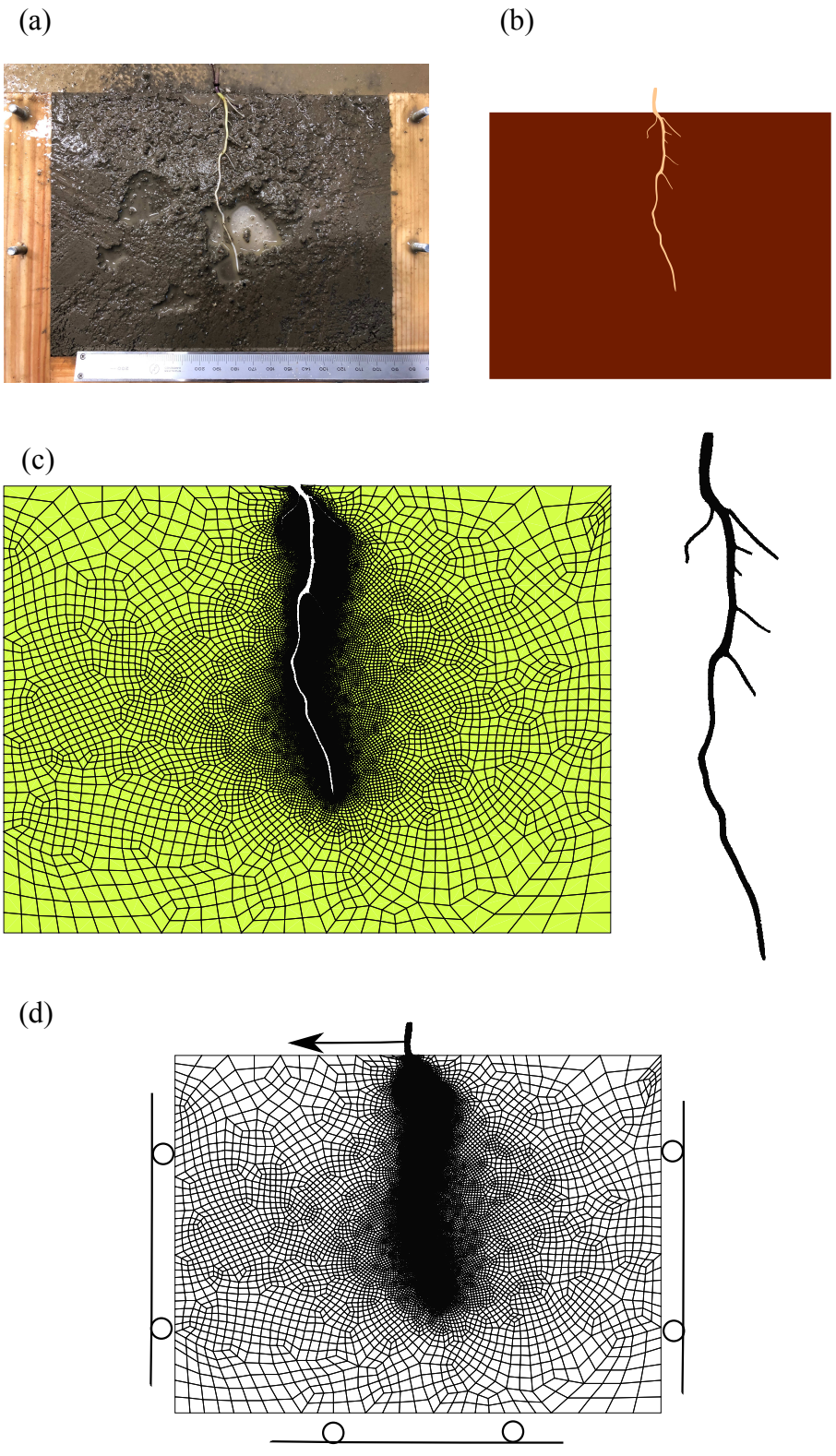

Figure 4.17: Proposed technique to generate high-quality mesh from image data using Python Imaging Library (PIL) and Gmsh: (a) Scanned image of root system, (b) Postarized image of (a), (c) Mesh obtained using PIL and Gmsh, and (d) Mesh of root-soil system where root/soil meshes are merged into a field.

4.5.4 Results of 2-D lodging simulation

The relationship between displacement and reaction force is plotted in Fig. 4.18, where the simulation is quantitatively similar to the experiment. The horizontal axis is the horizontal displacement of the root and the vertical axis is the reaction force at each time. The profiles of simulation is the almost same as the experimental one when the displacement is less than 1.3 mm. The gap between the simulation and the experiment opens at the displacement is 1.0 mm, however, the difference is still no more than 15 %. This results suggests that the NTS approach can simulate 2-D root-soil contact problem with high accuracy. Fig. 4.19 and Fig. 4.20 show contour plots of deviatoric stress and deformation, respectively, during the analysis. It visualizes that the propagation of deviatoric stress from the root to the soil and shows that the deviatoric stress firstly propagates to top-left of the soil and secondary goes to the bottom sides along the primary and the secondary root. It indicates that the morphology of the root, in this case, especially primary roots, affect the direction and attitude of the propagation. Above all, the NTS approach with FEM is successfully applied to simulate the 2-D lodging problem and visualize the stress field and deformation of rooted soil.

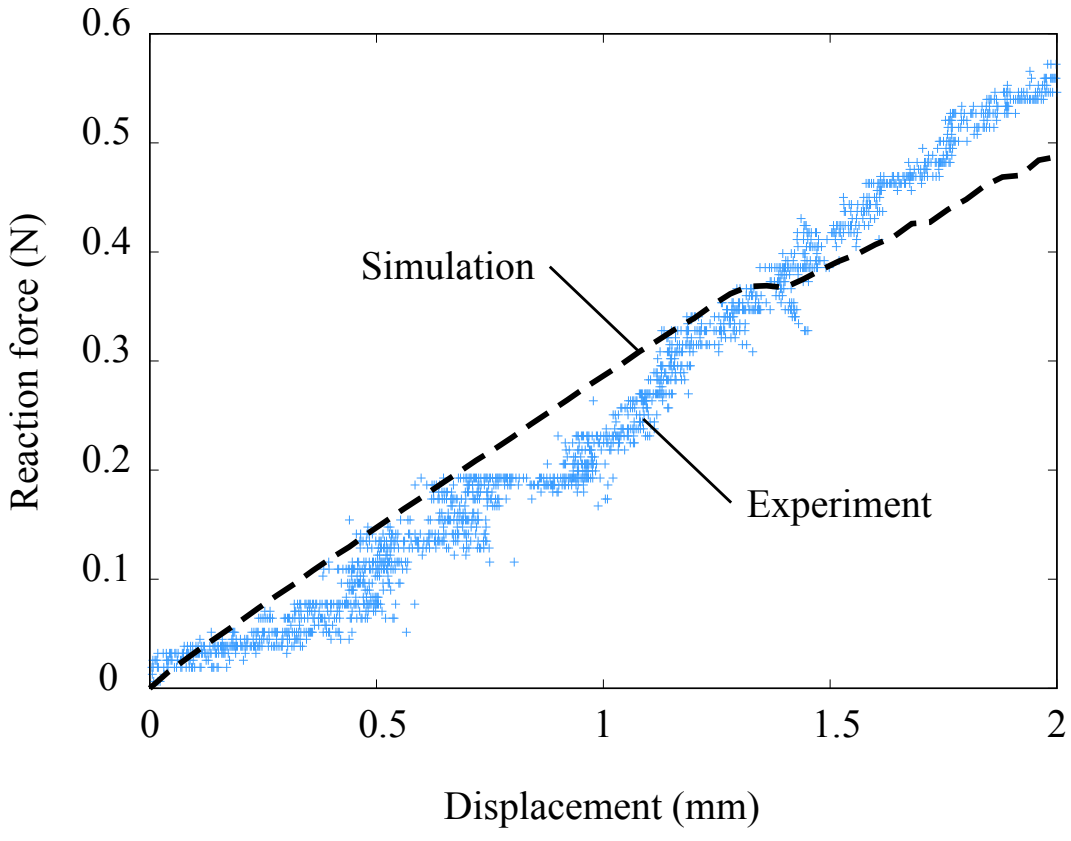

Figure 4.18: Comparison of experiment and simulation in relationship between horizontal displacement and reaction force.

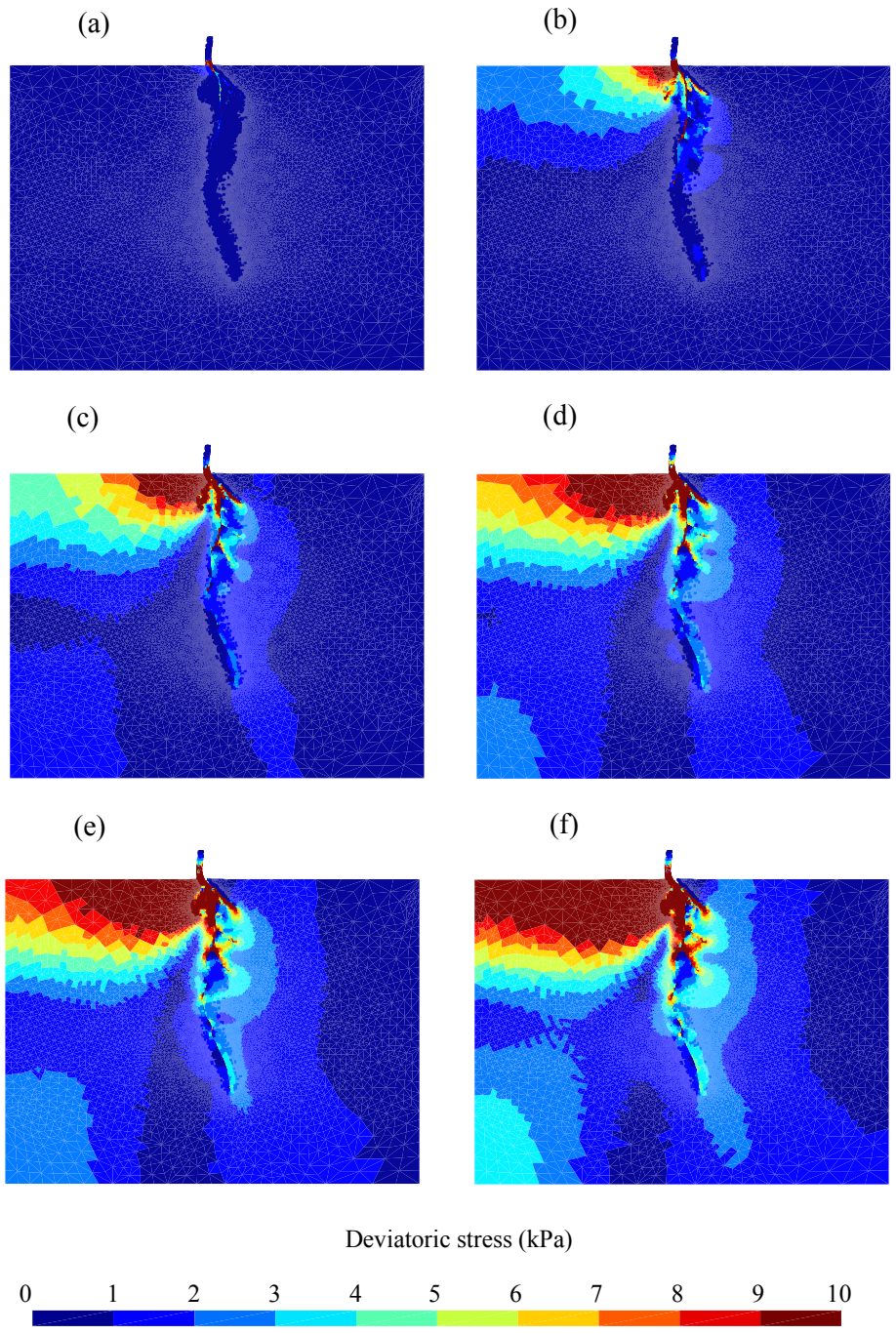

Figure 4.19: Contour plot of deviatoric stress when displacement is (a) 0.04 mm, (b) 0.4 mm, (c) 0.8 mm, (d) 1.2 mm, (e) 1.6 mm, and (f) 2.0 mm

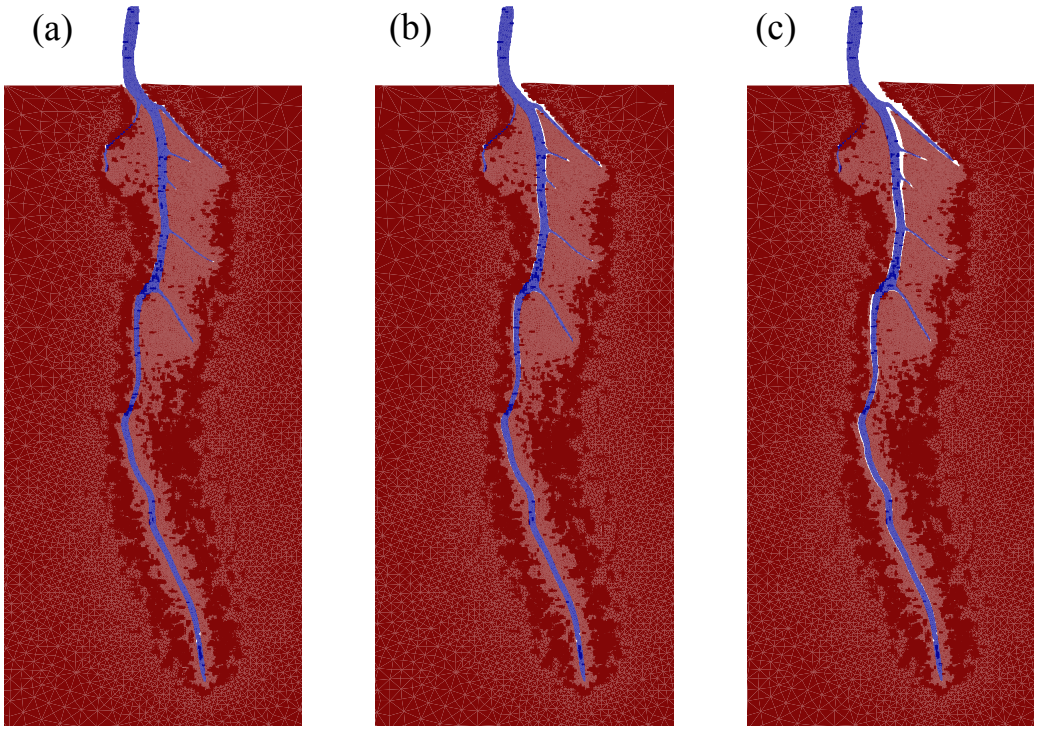

Figure 4.20: Deformation when displacement is (a) 0.0 mm, (b) 1.0 mm, and (c) 2.0 mm.

4.6 Summary

This chapter presents an implementation and applications of NTS approach to solve 2-D deformation problem for root-soil systems. According to the results and discussions, following conclusions have been drawn.

1. Contact/separation are implemented based on NTS approach and stick/slip are implemented by carefully-chosen model for root-soil contact problems. As for the slip criterion the Mohr-Coulomb model is adopted for slip criterion, which has been experimentally validated by current investigations (Tomobe et al., 2016, Ji et al., 2018). The slip is integrated over time-steps and the backward Euler scheme is used, which is analogous to the return-mapping algorithm of the plasticity theory.

2. A simple and novel pairing algorithm for NTS elements are presented to avoid the non-uniqueness problem for NTS pairing, which is necessitated by the geometrical non-linearity of the root-soil contact problems. The problem is a critical issue in the root-soil contact problems since it often causes non-uniqueness of the solution for geometrically complex contact problems.

3. The analysis of a pullout problem examined the applicability of the current approach for practical problems on root-soil contacts. The simulation was compared with the experiment of Tomobe et al. (2016) since the current approach utilized the Mohr-Coulomb model to implement the friction and the cohesion and it is compatible with their modeling. In particular, the following points were considered in this problem: (1) the cohesion is taken into account, whereas it is ignored in the press-fit problem, and (2) the root undergoes large sliding along the soil mass, and the stress profiles are compared the experimental values. The results showed that the current method can provide reasonable predictions for the profiles of the pullout response. Furthermore, the shear strength on the root-soil interfaces is precisely predicted, which indicates that both the friction and the cohesion are appropriately calculated in the current scheme.

4. A novel pre-processing technique for 2-D root-soil systems is also presented for generating high-quality mesh of roots and soils by using PIL and Gmsh. This technique generates meshes from scanned data of roots and soils by using PIL, which is image-processing library of python and Gmsh, which is an open-source software for modeling and meshing for FEM

5. A 2-D lodging problem is numerically simulated to demonstrate the application of the current approach to lodging problems, which are examples of plant-scale problems. The results were compared with those measured by a lodging experiment. The experiment was conducted using the protocol that was developed by Shimada et al.

(2002) and Berry et al. (2003) and utilized for many cases (Berry et al., 2004; Berry et al., 2014; Wu and Ma, 2016). The results indicate that the numerical method can provide realistic and detailed stress mapping of lodging problems and that such interfacial behavior as the separation, the contact, and the sliding are observed. This information will aid in the understanding of the mechanical interaction between roots and soils. As for the accuracy of the prediction, the numerical simulation is consistent with the experiment, while the horizontal displacement is relatively small. Although the prediction is not quantitatively identical to the experiment, in cases where the deformation is relatively large, it is suggested that the error can be reduced by utilizing more detailed constitutive models or mesh models for soils and roots. Further studies are to be performed to increase the accuracy in largely deformed cases and to apply the current method to large-scale problems like landslides and surface erosions.

Chapter 5

Constitutive Model for Shear Strength of Root-Soil Interface Under Dynamic Suction Condition

5.1 Introduction

The wet-dry conditions are the primary factor determining the shear strength of rooted soils, therefore, the hydro-mechanical properties of rooted soils have been investigated for decades. Earlier researches focus on the shear strength of rooted soils by using in-situ direct shear tests (Endo, 1980; Abe and Ziemer, 1991) conducted in vegetated slopes. The results suggest that the Mohr-Coulomb (MC) model can describe the shear strength of rooted soils and the root reinforcement appears in the apparent cohesion. For instance, Fan et al. (2009) and Ni et al. (2018) report that the increase of the suction can enhance the apparent cohesion of rooted soils; they explain that the soil domains are divided and covered by root fibers and the roots protect soil domains from water penetration. Although these experimental observations provide some simple mechanical models of shear strength of rooted soils under changing hydro-mechanical conditions, further investigations are to be conducted to provide an accurate prediction of the shear strength of rooted soils, which can be used for design and maintenance of vegetated slopes. (Giadrossich et al., 2017).

Previous investigations assume that the decline of shear strength of rooted soil due to high water content is mainly caused by the loss of shear strength of soil domains, and not by that of roots or root-soil interfaces (Ng et al., 2013; Song et al., 2017): Thereby, the effect of wet-dry conditions for shear strength of root-soil interfaces are ignored. As presented by Ng et al. (2013), the plant-induced suction caused by evapotranspiration and water-absorption of plants is the primary cause of root reinforcement. Such the plant activities decrease the water content of soils and hence increases the shear strength of soils. The other well-known factor is that the root changes hydraulic conductivity of soils and it can keep water content

of soils low; Song et al. (2017) present that this factor is also critical. Both discussions are based on the hypothesis that the decline of shear strength of rooted soil due to high water content is mainly caused by the loss of shear strength of soil domains in rooted soils. Here, a question remains whether the effect of wet-dry conditions for shear strength of root-soil interfaces can also be the critical factor or not; since roots have large interface areas between soils.

Since rooted soils consist of roots and soils, the hydro-mechanical response of the root-soil interfaces, especially the shear strength of root-soil interfaces and suction, can also have a significant role for bulk shear strength of rooted soils under changing hydraulic conditions. It has been quite challenging to evaluate the shear strength of root-soil interfaces by using existing methods, but recent studies have proposed novel methodology to measure the friction and the cohesion of the interfaces and achieved the modeling. Mickovski et al. (2010), Schwarz at al. (2011) and Tomobe et al. (2016, 2019) develop pullout tests to estimate the shear strength of the root-soil interfaces and show that the Mohr-Coulomb model can be utilized to model the shear strength of root-soil interfaces. However, few models are still presented that models that predict the shear strength of root-soil interfaces under different soil pressure with dynamic suction conditions.

Table 5.1: Structure and overview of the chapters 5 and 6

	Soil Pressure	Suction	Both
Experiment and model	Tomobe et al. (2016; 2019) : Chapter 5	Novel apparatus :Chapter 5	MCV model : Chapter 5
Simulation	MCV-NTS approach : Chapter 6		MCV-NTS for dynamic suction condition : Chapter 6

This chapter and the next chapter aims to propose a series of a consistent method to measure, model, and predict the shear strength of root-soil interfaces under changing soil-pressure and changing suction based on the pullout tests of Tomobe et al., (2016, 2019), Mohr-Coulomb model, and Vilar model (Vilar, 2006). Fig. 5.1 visualizes major driving factors of shear strength of root-soil interfaces; soil pressure and suction. Friction increases as the increase of soil pressure and cohesion of root-soil interfaces are increased under high-suction conditions. The soil-pressure-induced friction is measured and modeled by Tomobe et al., (2016; 2019), however, the suction-induced cohesion is not measured nor modeled (Table 5.1). Further, few models are proposed to predict both of the friction and cohesion. In this chapter, Sections 2 and 3 shows experiments to measure the friction and suction-induced cohesion, respectively; Although Section 2 just summarizes and introduces the pullout tests of Tomobe et al., (2016), it is explained in detail since the chapter is closely related to a proposed experiment of Section 3 and numerical simulation of Section 5. Section 3 proposes a novel pullout test to measure the suction-induced cohesion of root-soil interfaces. From the results of Sections 2 and 3, the shear strength of root-soil interfaces are consists of friction and cohesion; friction is modeled by the MC model as seen in Section 2 and cohesion is modeled by the Vilar model which is visible in Section 3. Section 4 combines the Mohr-Coulomb (MC) model and Vilar model as Mohr-Coulomb-Vilar (MCV) model, and the MCV model is implemented into numerical simulation based on the Node-To-Segment (NTS) method which can accurately model the geometry of the root-soil interfaces within the framework of Finite Element Method (FEM). Afterward, the conclusion is stated in Section 5.

5.1.1 Summary of the materials and methodology

The tested soil and roots are sampled at experimental field of Kyoto University in Sakyo-ku, Kyoto City, Japan (35°01′56.9”N 135°47′00.4”E).Two types of pullout tests are conducted; pressure-controlled tests and suction-controlled tests.The pressure-controlled test is conducted for measuring the relationship between shear displacement and shear stress under

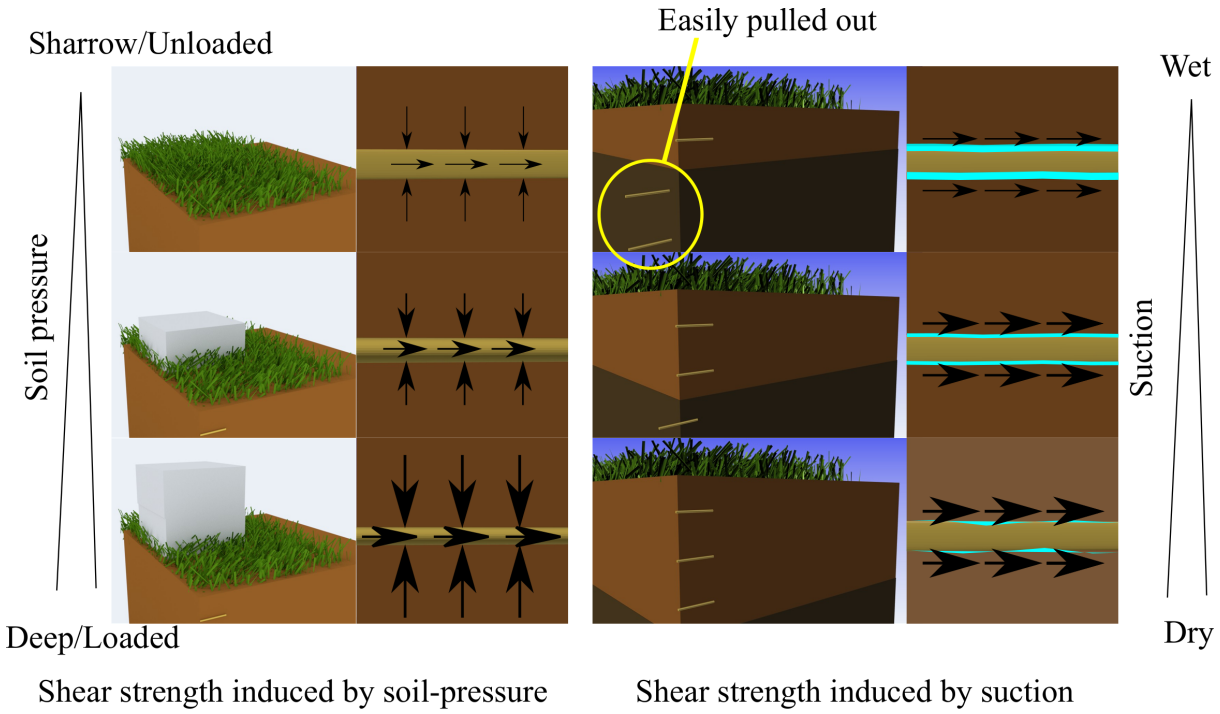

Figure 5.1: Schematic view of two major driving factors of shear strength of root-soil interface; soil pressure-induced friction (left) and suction-induced cohesion (right). Friction increases as the increase of soil pressure, and cohesion of root-soil interface is increased under high-suction conditions.

changing soil pressures, which is expected to be modeled by Mohr-Coulomb model.The suction-controlled test is conducted for measuring the relationship between shear displacement and shear stress under changing soil suction, which is expected to be modeled by Vilar model.The constitutive relationship of root-soil interfaces is modeled by combining MC model and Vilar model, which is called MCV model in this thesis. Both of the pullout tests are simulated by using MCV model, which is stated in latter sections.

5.2 Pressure-controlled pullout test

This section summarize the results of pressure-controlled pullout tests presented in Chapter 3 and gives new explanations from the viewpoint of MCV model to utilize the results for the validation of the MCV model in this chapter. Table 5.2 shows the dry density and the water content of the soil; these are measured after the experiments. For all cases, the original dry density is 0.97 g/cm^3 and the water content is 31.5 %. After the experiment, the dry density is 0.96 g/cm^3 to 0.98 g/cm^3, which is almost the same as the original value. The water content is also not changed significantly. From these results, the mechanical properties of soils are not changed significantly during the experiment since the soil pressure is extremely small.

The relationship between shear displacement and shear stress for under different normal stress is visible in Fig. 5.2. For all cases, shear stress is proportional to the shear displacement when the shear displacement is less than 4.0 mm. The shear stress starts declining as shear displacement reaches around 4.0 mm to 7.0 mm and reaches the maximum shear stress. After the peak shear stress is observed, the shear stress keeps almost the same value over 2.0 mm to 5.0 mm. The relationship between normal stress and maximum shear stress is shown in Fig. 5.3. It is indicated that the maximum shear stress is proportional to the normal stress (R^2 = 0.98). The intercept of the line is 3.14 kPa and the frictional coefficient is around 0.60. This relationship is consistent with the well-known Mohr-Coulomb's model and the coefficients are consistent with the frictional coefficient, hence, it shows that the frictional coefficient between the root and the soil is 0.60. From the standpoint of MCV model, it is considered that the cohesion of 3.14 kPa represents the suction-induced cohesion of the root-soil interface under given water condition. Further, it is also assumed that the frictional coefficient of 0.60 is not changed when the suction of root-soil interface is changed.

Table 5.2: Material properties of soil sample

Soil particle density (g/cm^3)	2.67
Dry soil density (g/cm^3)	1.28
Water content (%)	31.5
Maximum root diameter (mm)	0.74
minimum root diameter (mm)	0.68

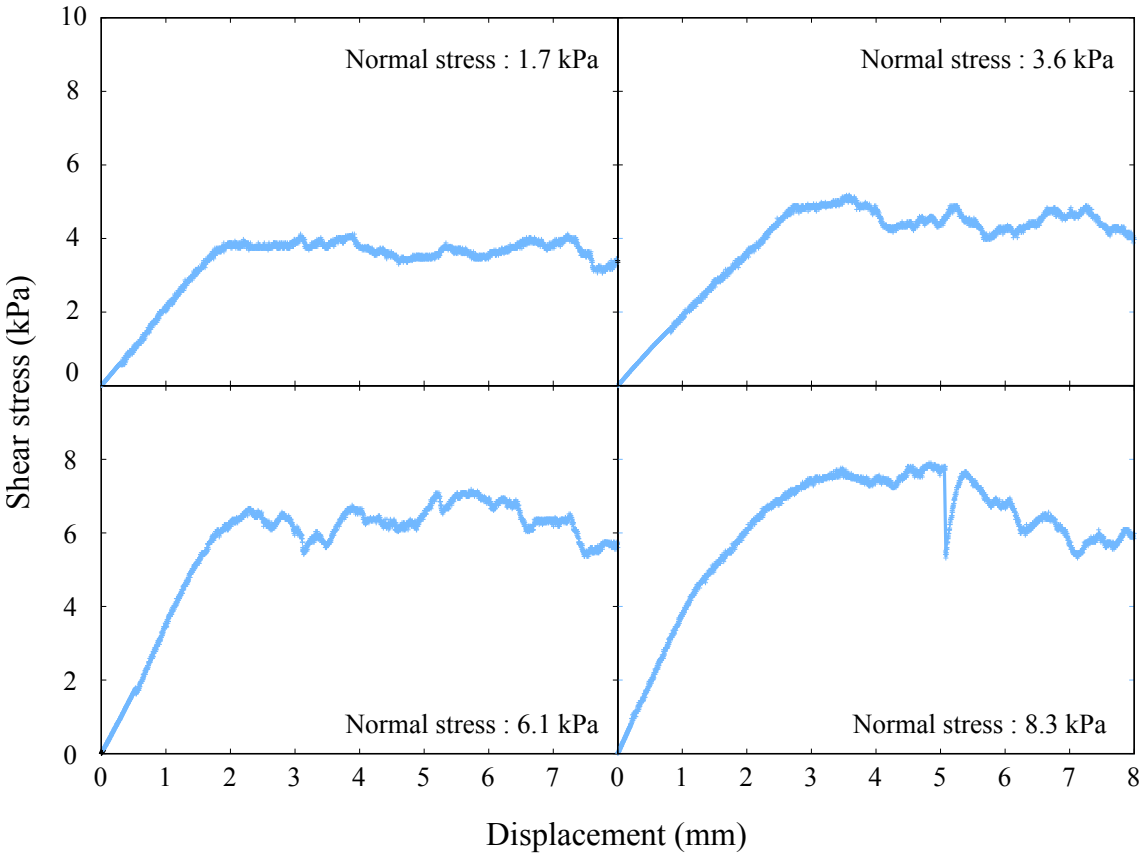

Figure 5.2: Relationship between shear displacement and shear stress measured by pressure-controlled pull-out tests for mean normal pressure of root-soil interface 1.7, 3.6 6.1 and 8.3 kPa, respectively.

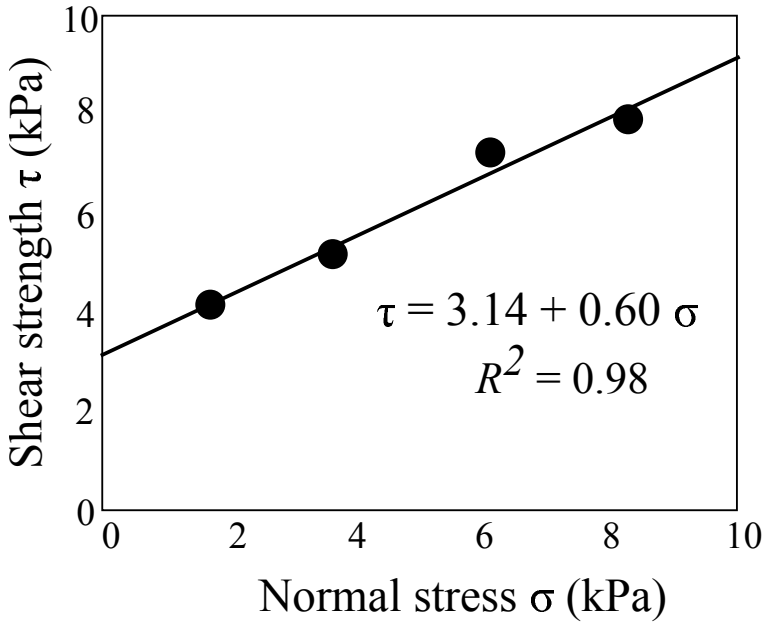

Figure 5.3: Relationship between normal stress and shear strength of root-soil interface measured by pressure-controlled pull-out tests: Mohr-Coulomb criterion is applicable to the slip criterion.

5.3 Suction-controlled pullout test

5.3.1 Apparatus and procedure

The objective of the experiment is to measure the shear properties of root-soil interfaces under prescribed suction. For this purpose, a novel pull-out apparatus is developed, which consists of a soil box, a vacuum pump, a root extractor, and a display server (Fig. 5.4). The soil box, the root extractor, and the display server are the same as the pull-out apparatus of Tomobe et al. (2016), by contrast, a vacuum pump (DIK-9230 Automatic Pressure Controller, DAIKI RIKA KOGYO, JAPAN) is newly installed to control the suction of the soil box. The vacuum pump is capable of keeping pressure from 0 kPa to -30.0 kPa, the performance of which is satisfactory for this experiment.

The root specimens are sampled from a barley plant (Hordeum vulgare L.) cultivated in Kyoto city, JAPAN (35 ° 01’57.2"N, 135 ° 47’00.4"E) in 2015, which is the same material as ones of Tomobe et al. (2016). Each root is straight, smooth and has roughly the constant diameters. The soil is sampled from the surface layer (0 to -15 cm) of the cultivated field after the sampling of the root; at the same time, the undisturbed soil samples are collected for measuring the bulk density, the water content, grain size analysis, and the density of the soil particles, where the soil properties are the same as the Chapter 3. The soil is categorized into sandy silt according to the method of classification of geo-materials for engineering purposes (JGS 0051-2009).

The procedure of the experiment is visible in Fig. 5.5. Before the experiment, the root

hole is filled up by grease which stops water, and the drain tube, the porous stone, and the soil box are carefully saturated with water. After the process, the root and the soil are put into the soil box, the dry bulk density of which is equal to one of the sampling points. Then, the pump vacuums the water at a prescribed pressure and the water starts to move from soil specimen to the cylinder until the equilibrium is achieved. The equilibrium is checked by measuring the water level in the cylinder. During the process, a thin plastic cover is put on the soil specimen to prevent drying.

After the equilibrium is achieved, the root is slowly (less than 0.1 mm/min) pulled out from the soil box by the root extractor illustrated in Fig. (5.4); the reaction force and the horizontal displacement are measured until the shear stress reaches the peak strength. This reaction force is measured by a load cell (LUX-B-50N-ID, KYOWA ELECTRONIC INSTRUCTION, JAPAN) and the displacement is recorded by using the displacement gauge (DDP-20A, Tokyo Sokki Kenkyujo, JAPAN). Above process is repeated for six cases under different suction conditions: 0.5 kPa, 4.4 kPa, 5.8 kPa, 8.8 kPa, 22.0 kPa, and 28.0 kPa. These suctions are chosen since the possible maximum suction realized by the apparatus is 28.0 kPa under automorphic pressure, and it ranges from water-saturated conditions to field water capacity.

The profile of the shear stress in the root-soil interfaces is computed by dividing the total pull-out force by the surface area of the root segment. Hence, the shear stress is computed as explained in CHapter 3. It is worth noting that the simple relationship can be used only when the diameter of the root segment is almost constant and the branch roots are not present, therefore, the root segment is sampled from a straight root with no branch and root hair is not observed at the root segment.

Furthermore, the relationship between suction and the shear strength is plotted to evaluate the shear reinforcement in the root-soil interfaces due to the suction, which is necessary to model the suction-induced cohesion so that the effect of suction is implemented in numerical schemes such as FEM. A similar relationship has been obtained in the cases of soil-soil interfaces and geotextile-soil interfaces and the models are available for FEM analysis, however, it has not been measured or modeled for root-soil interfaces. This thesis models the strength-suction curve based on the formulation of Vilar (2006); it has been utilized for modeling the suction-induced cohesion in the unsaturated soils, the detail which is explained below with the results.

5.3.2 Results and formulation based on Vilar's model

The profiles of the shear stress of each experimental case are measured by using the pull-out tests, which is seen in Fig. 5.6. The curves show that the shear stresses increase with the increase of the displacement for all experiments and soon approach asymptotically to the maximum shear stress. This process is described in more detail as following; the shear

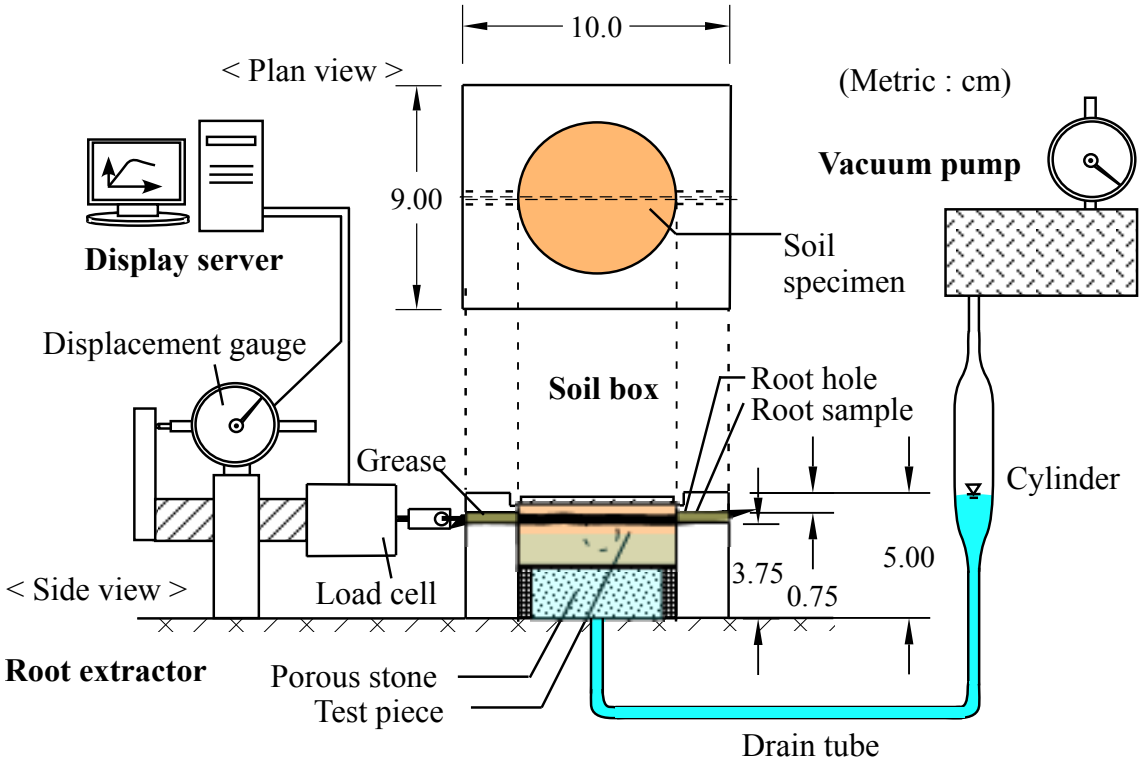

Figure 5.4: Apparatus for suction-controlled pull-out tests: Suction is loaded by left-hand-side vacuum pump and no soil pressure is loaded.

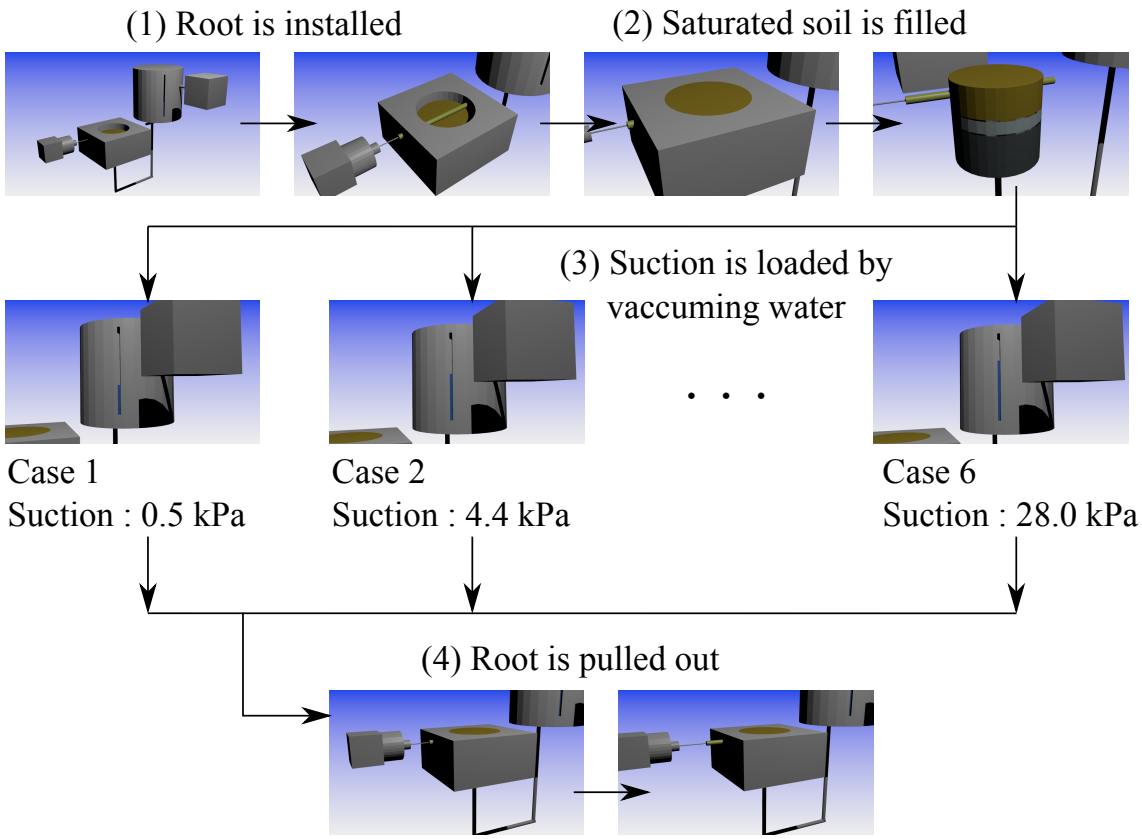

Figure 5.5: Procedure of suction-controlled pull-out tests: (1) a straight root is installed into a empty soil-box, (2) water-saturated soil is filled into the soil-box, (3) prescribed suctions are loaded for case 1 to case 6, where the soil suction are 0.5, 4.4, 5.8, 8.8, 22.0, and 28.0 kPa, respectively. (4) The root is pulled out from the soil and reaction force is measured.

stresses initially increase by constant rates for the displacement is 0.0 to 5.0 mm, and then keeping almost the constant values when the displacement is 5.0 mm to 18.0 mm. After the shear stresses reach the shear strength, the roots globally slip and the stresses decrease moderately (Cases (a), (b) and (c)) or rapidly (Cases (d), (e) and (f)). Compared with the curve of Case (a), the angles and the peaks of the curves in other cases are significantly large, and the suction-induced cohesion in the root-soil interfaces are significantly increased from 0 kPa to 25 kPa while the suction increases from 0.0 kPa to 28.0 kPa. The relationship between the maximum shear stress and the suction is seen in Fig. 5.7. The shear strength increases with the increase of the suction during the suction are smaller than 10.0 kPa; subsequently, the shear strength becomes almost the constant value. Similar responses have been observed for geotextile-soil interfaces (Jotisankasa and Rurgchaisri, 2018) and soil-soil interfaces (Song et al., 2017), however, to the knowledge of the authors, the current results are first of its kind for root-soil interfaces. As can be seen in Fig. 5.8, this section applies the model of Vilar (2006) to model the relationship between suction and shear strength of root-soil interfaces. The model is written as

$$\tau = c + \frac{s}{a \cdot s + b} \tag{5.1}$$

where τ is the shear strength of the root-soil interfaces, s is the suction, c is cohesion, and a and b are model parameters. The model is chosen for three reasons: (1) it is indicated that the mechanism of the suction-induced reinforcements of soil-soil interfaces which are often modeled by the Vilar model, and the root-soil interfaces are similar as described in Fig. 5.9. This illustrates the hypothetical structure of the soil-soil and the root-soil interaction under the unsaturated condition. As is well known, the surface water can generate the apparent cohesion between soil particles as seen in the left, therefore, the same phenomena must occur in root-soil interfaces, (2) the model is capable of expressing the nonlinear properties by using the possible simplest function, and (3) in the other methods such as Fredlund et al. (1996), the effective angle of friction should be same as the friction angle relative to suction, however, in this case, the frictional angle estimated from the relationship between suction and shear strength is 68 degrees, which is significantly greater than one measured based by frictional tests (Tomobe et al., 2016). Similar differences are reported by Likos et al. (2018) in soil-soil interfaces under low-pressure conditions. They point out that the dilation of the strength development may cause the phenomenon, and that further studies are to be done to reveal the mechanism. The result of the curve fitting is presented in Fig. 5.8 and the parameters a and b are shown in Table 5.3, which can precisely express the suction-induced cohesion. In this result, the normal stresses are considered to be zero since the normal pressure on the root-soil interfaces is negligibly small in during the experiment.

Table 5.3: Model parameters of roots, soils and root-soil interfaces

	Young's modulus (kPa)	Poisson's ratio	Penalty parameter (kPa/m)	Frictional coefficient	a	b
Root	60000.0	0.35	-	-	-	-
Soil	6038.9	0.35	-	-	-	-
Root-soil interface	-	-	50000.0	0.60	0.191	0.00343

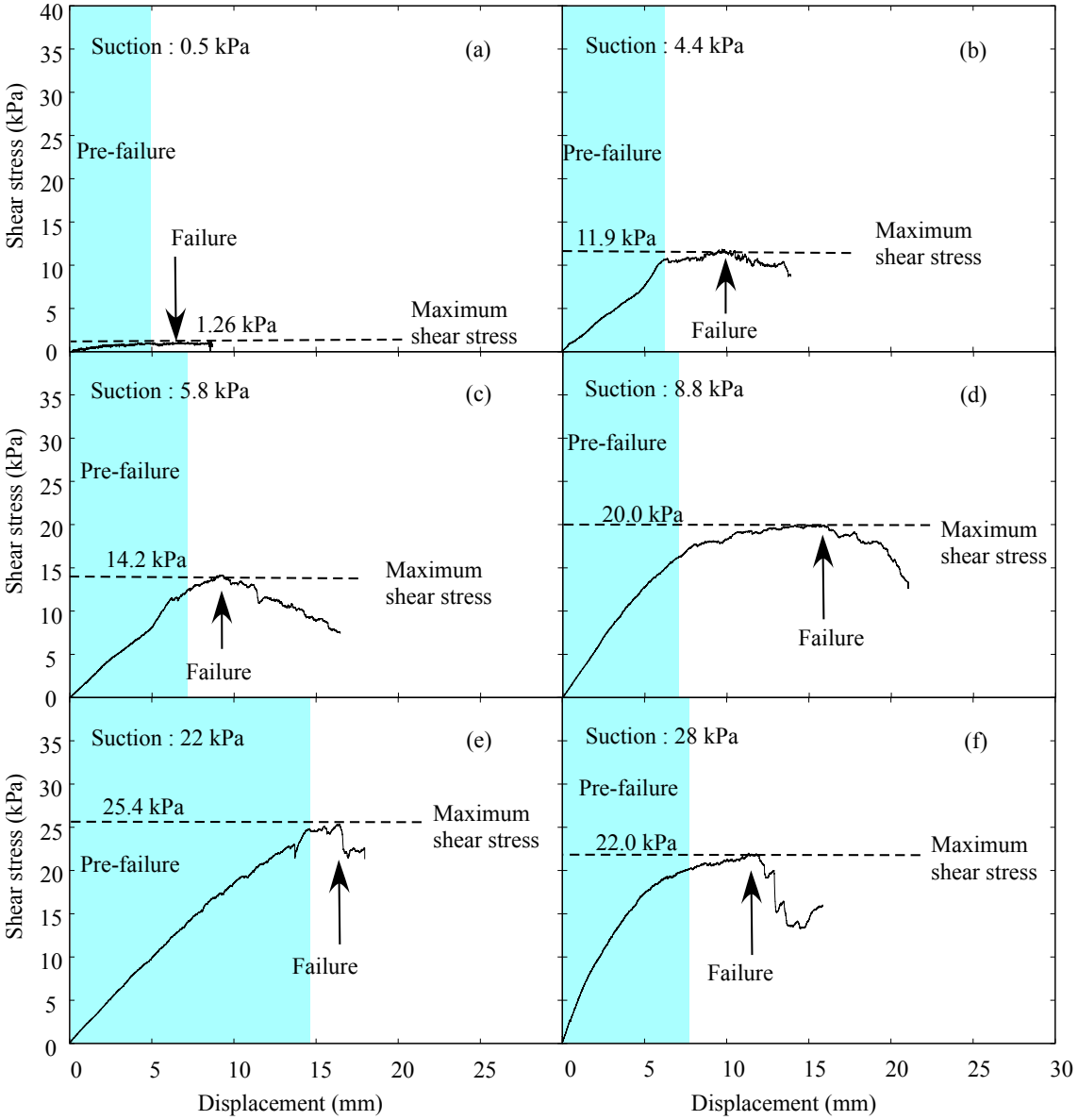

Figure 5.6: Relationship between shear displacement and shear stress measured by -controlled pull-out tests for suctions of root-soil interface 0.5, 4.4, 5.8, 8.8, 22.0, and 28.0 kPa, respectively.

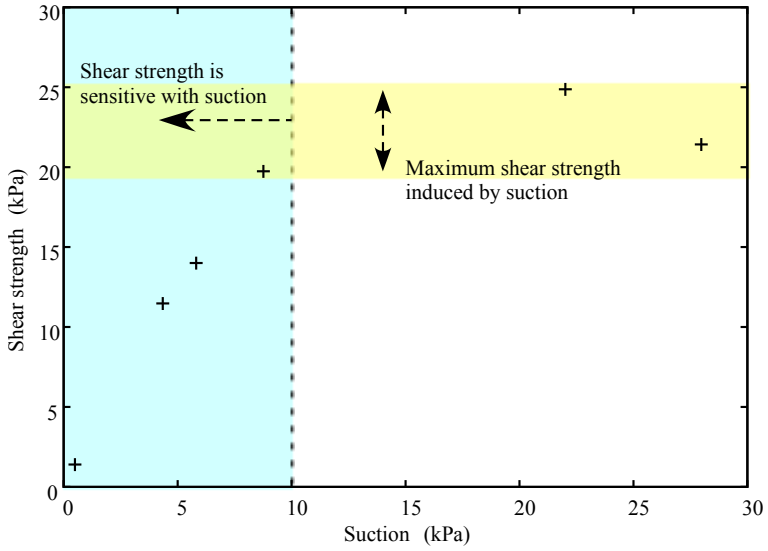

Figure 5.7: Relationship between suction and shear strength of root-soil interface measured by suction-controlled pull-out tests.

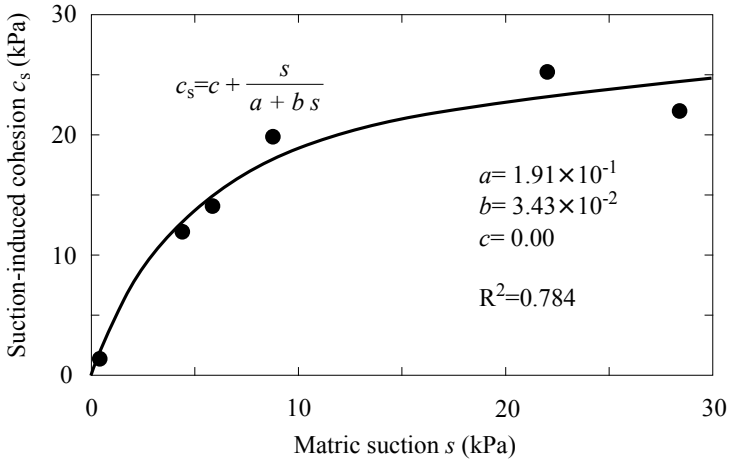

Figure 5.8: Parameter fitting of Vilar model for the Relationship between suction and shear strength of root-soil interface.

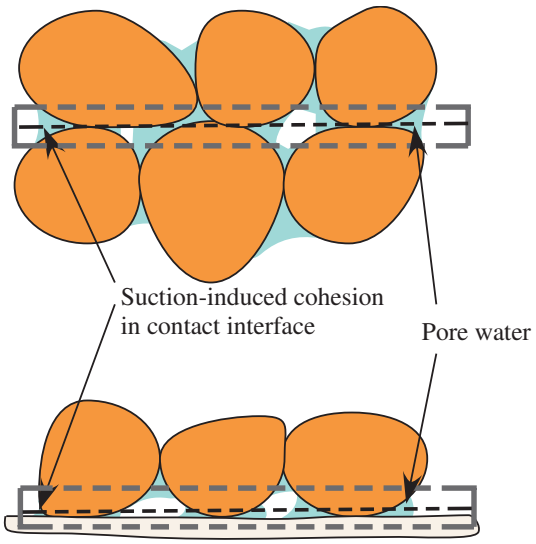

Figure 5.9: Schematics of root-soil interface and soil-soil interface

5.4 Constitutive Model of shear strength of root-soil interface under changing pressure/suction

5.4.1 MCV model

The last section utilizes the Vilar model along with Mohr-Coulomb model to model the suction-induced cohesion of root-soil interfaces under different suction/stress conditions: This subsection defines the model as MCV model, in which the shear strength of root-soil interfaces are expressed as

$$\tau_{max} = c + \mu \cdot \sigma_N + \frac{s}{a \cdot s + b} \tag{5.2}$$

where τ_{max} is shear strength, μ is frictional coefficient and σ_N is soil pressure. The frictional coefficient is measured by conventional pullout tests, for instance, the frictional coefficient of the root-soil interfaces is 0.60 according to Section 2 and Tomobe et al. (2016). Fig. 5.10 maps the shear strength under different soil pressure and suction and the box illustrates the possible condition under the practical situations. Here, the soil pressure is supposed to be caused by the soil pressure in grasslands and cultivated field, the value of which is less than 10 kPa since the depth of the rhizosphere is less than 1.0 meters. In such cases, as displayed, the shear strength is mainly determined by suction in these results, which suggests that the suction prevents slips at interfaces between roots and cohesive soils.

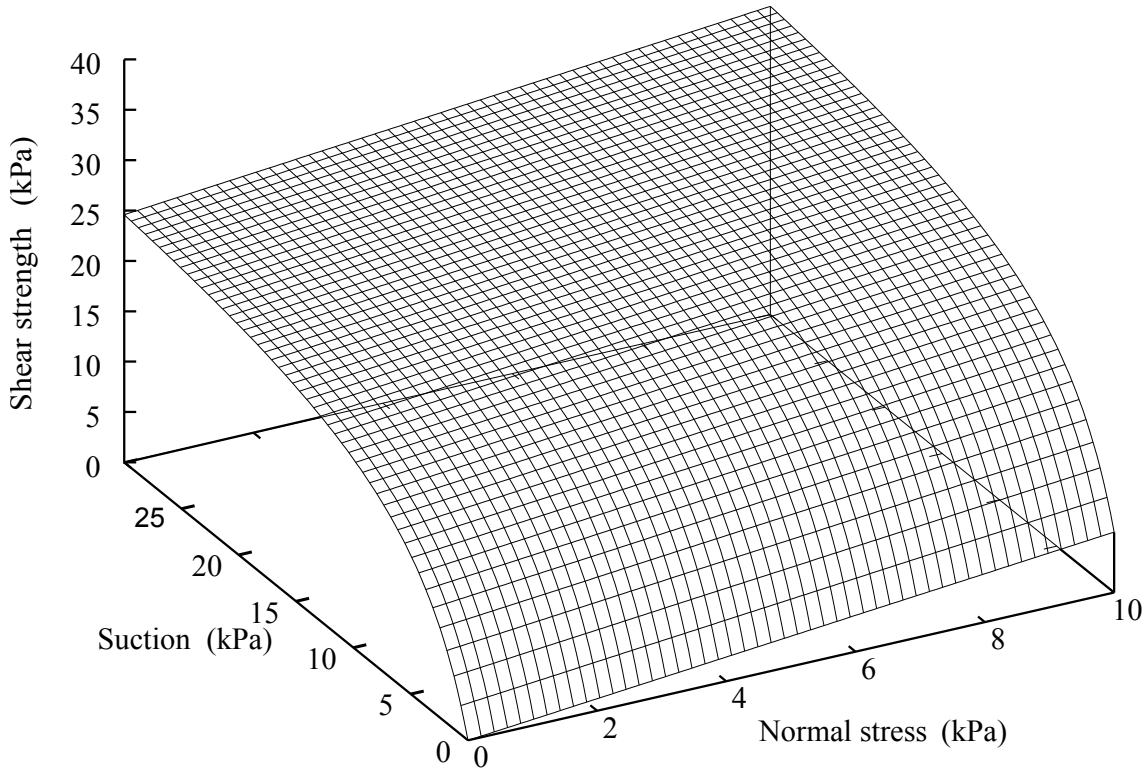

Figure 5.10: Critical state surface of root-soil interface based on Mohr-Coulomb-Vilar model.

5.4.2 Implementation of MCV model based on NTS approach

The model of the shear strength in the root-soil interfaces is numerically implemented by using the NTS approach (Wriggers 2006) within the framework of FEM to apply the experimental results for the prediction of the risk of landslides in the presence of vegetation. This subsection summarizes the NTS approach in terms of root-soil contact problems and then proposes the implementation of the suction-induced reinforcement in root-soil interfaces. Recently, the FEM has been applied for predicting the mechanical behavior of rooted soils, which provides accurate analysis for root-soil interaction by using realistic root morphology. In this method, both roots and soils are discretized into finite elements as depicted in Fig. 5.11, and the root-soil interfaces are installed by using some strategies such as Node-To-Node (NTN) approach or Line Elements (LE) scheme. However, developing the precise implementation of the root-soil interfaces still has been a challenging problem. This subsection applies the NTS approach to implement the friction and the suction-induced cohesion into the FEM analysis. Here, the NTS approach is the widely-used method to express the mechanical interactions between deformable bodies in numerous engineering problems (Wriggers, 2006). It consists of one node on a body and a surface element on the other body as seen in the Chapter 2. The approach is capable of expressing both slip and separation in root-soil interfaces, which cannot be done by using conventional methods as NTN or LE

methods. The governing equation and the discretization of the contact problems between roots and soils can be described as the following: Let us consider that a root and a soil mass are in contact and the contact surface is identified as illustrated in Chapter 2. Under the condition, the governing equation for the displacement field is given by the virtual work equation seen in Eq. (5.3).

$$\begin{aligned} \delta W = \left(\int_\Omega \sigma \cdot \nabla \delta \mathbf{u} d\Omega - \int_\Omega \mathbf{f} \cdot \mathbf{u} d\Omega - \int_\Gamma \mathbf{t} \cdot \mathbf{u} d\Gamma \right)^r \quad + \\ \left(\int_\Omega \sigma \cdot \nabla \delta \mathbf{u} d\Omega - \int_\Omega \mathbf{f} \cdot \mathbf{u} d\Omega - \int_\Gamma \mathbf{t} \cdot \mathbf{u} d\Gamma \right)^s + \delta W^{rs} \quad = \quad 0 \end{aligned} \tag{5.3}$$

Within Eq. (5.3), δW denotes the total virtual work, superscript r, s, and rs denotes the root, the soil and the interfaces, respectively, σ is the Cauchy stress tensor, $\delta \mathbf{u}$ and $\nabla \delta \mathbf{u}$ are the virtual displacement and its gradient with respect to the current configuration, $\mathbf{f}$ is the gravitational force and $\mathbf{t}$ is the traction forces. The last term denotes the virtual work of the contact surface, which is explicitly expressed as Eq. (5.4);

$$\delta W^{rs} = \int \mathbf{t}_N \cdot \delta \mathbf{g}_N d\Gamma + \int \mathbf{t}_T \cdot \delta \mathbf{g}_T d\Gamma \tag{5.4}$$

where $\mathbf{t}_N$ and $\mathbf{t}_T$ are the normal/shear stress, $\mathbf{g}_N$ is the gap vector from the soil surface to the closest point on the root surface and $\mathbf{g}_T$ is the tangential displacement from the initial contact point. Further, a penalty parameter ϵ is introduced in order to prevent unnatural overlaps between roots and soils;

$$\mathbf{t}_N = \epsilon \cdot \mathbf{g}_N \tag{5.5}$$

Hence, the contact pressure is proportional to the degree of overlaps: the overlaps theoretically become zero in case that the penalty parameter is enough large. The terms in the first and the second parentheses within Eq. (5.3) are discretized by using finite elements and the last term is discretized by using the NTS elements, thereby, the discretized equations are expressed by Eq. (5.6),

$$\delta W = \sum_{I=1}^{ne} \delta \mathbf{u}^{d(I)} \cdot \mathbf{R}^{d(I)} + \sum_{I=1}^{nc} \delta \mathbf{u}^{c(I)} \cdot \mathbf{R}^{c(I)} = 0 \tag{5.6}$$

in which ne is the number of finite elements for both the root and the soil mass, nc denotes the number of NTS elements in the contact interfaces, $\delta \mathbf{u}^{d(I)}$ and $\delta \mathbf{u}^{c(I)}$ are variations of the discretized displacement vectors for the bodies and the contact interfaces. $\mathbf{R}^{d(I)}$ is the residual vector for the domain, the derivation of which is presented by Wriggers (2006) and Hashiguchi and Yamakawa (2011). $\mathbf{R}^{c(I)}$ is the residual vectors and the derivation is exhibited in detail by Wriggers (2006) and Zavarise and Lorenzis (2009). Since Eq. (5.6) is nonlinear for the displacement field, the Newton‘s method are employed as the solving algorithm. The algorithm is presented in Fig. (5.12).

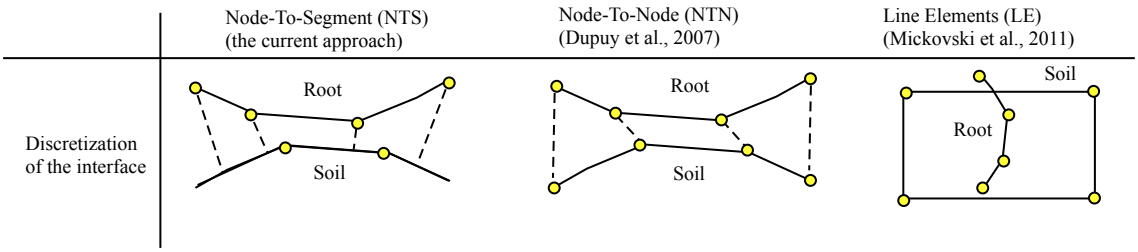

Figure 5.11: Comparison among contact elements used in current and previous studies.

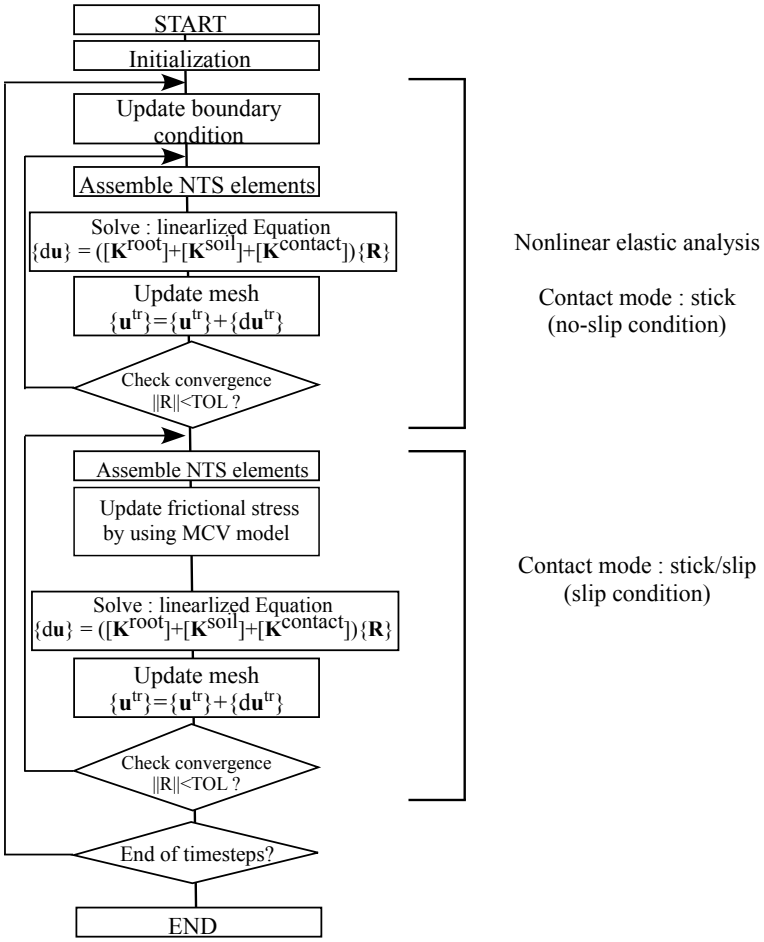

Figure 5.12: Solution algorithm for current numerical simulation based on FEM and CCM.

5.4.3 Solution algorithm

This subsection proposes a method to use MCV model in terms of NTS method summarized in Section 4. In Eq. (5.4), the tangential gap is decomposed into two parts, stick and slip;

$$\mathbf{g}_T = \mathbf{g}_T^{stick} + \mathbf{g}_T^{slip} \tag{5.7}$$

Here, $\mathbf{g}_T$ is tangential gap between two material points on the contact surfaces, $\mathbf{g}_T^{stick}$ is elastic part of the gap and $\mathbf{g}_T^{slip}$ is the plastic part. The shear stress $\mathbf{t}_T$ takes the form of Eq. (5.8).

$$\mathbf{t}_T = \epsilon \cdot \mathbf{g}_T^{stick} = \epsilon \cdot \left(\mathbf{g}_T - \mathbf{g}_T^{slip} \right) \tag{5.8}$$

This is derived by a natural assumption that the shear stress is caused by stored energy on the interface and the slip decays the stored energy, hence, it decreases the shear stress. By introducing the penalty method, the shear stress increases with the increase of tangential gap until the stress is smaller than the frictional strength. Based on the model of the friction and the suction-induced cohesion under unsaturated conditions, the slip criterion of the root-soil interfaces can be calculated as follows:

$$f = \|\mathbf{t}_T\| - c - \mu \cdot \|\mathbf{t}_N\| - \frac{s}{a \cdot s + b} \tag{5.9}$$

In case that f is positive, the increment of the slip $\dot{\mathbf{g}}_T^{slip}$ is updated by the flow rule as shown in Eq. (5.10),

$$\dot{\mathbf{g}}_T^{slip} = \dot{\lambda} \frac{\partial f}{\partial \mathbf{t}_T} \tag{5.10}$$

where $\dot{\lambda}$ is the increment of the plastic multiplier. Eqs. (5.8) – (5.10) are analogous to those of elasto-plasticity theory (Wriggers, 2006) and it enforces a constraint that the direction of the slip has to be identical to the direction of shear stress. The increment of the slip $\dot{\mathbf{g}}_T^{slip}$ is integrated by employing the backward Euler scheme, Eq. (5.10) is written as

$$\frac{\mathbf{g}_T^{slip}\left(t_{n+1}\right) - \mathbf{g}_T^{slip}\left(t_n\right)}{\Delta t} = \dot{\lambda} \frac{\partial f\left(t_{n+1}\right)}{\partial \mathbf{t}_T^{tr}\left(t_{n+1}\right)} \tag{5.11}$$

where t_n and t_{n+1} indicate current and next time-step, respectively. Substituting Eq. (5.9) into Eq. (5.11) we obtain Eq. (5.12).

$$\dot{\lambda} = \frac{\|\mathbf{t}_T^{tr}\left(t_{n+1}\right)\| - \left(\mu \cdot \epsilon \cdot \|\mathbf{g}_N\| - \frac{s}{a \cdot s + b}\right)}{\epsilon \cdot \Delta t} \tag{5.12}$$

Therefore, the slip and shear stress is updated by Eq. (14).

$$\dot{\mathbf{g}}_T^{slip} = \frac{\|\mathbf{t}_T^{tr}\left(t_{n+1}\right)\| - \left(\mu \cdot \epsilon \cdot \|\mathbf{g}_N\| - \frac{s}{a \cdot s + b}\right)}{\epsilon \cdot \Delta t} \frac{\partial f}{\partial \mathbf{t}_T^{tr}} \tag{5.13}$$

Eqs. (5.8), (5.9) and (5.13) are utilized in the solution algorithm as depicted in Fig. (5.12).

5.5 Summary

The current chapter proposes the MCV model with the NTS approach, and the MCV model is capable of expressing both friction and suction-induced cohesion. The following conclusions are remarked from the results in this chapter. A novel pull-out apparatus is developed for measuring the suction-induced cohesion of root-soil interfaces. The results show that the suction-induced cohesion increases with the increase of suctions during the suction are in the range of 0 to 10 kPa, and it reaches 25 kPa., which is larger than the contribution of friction under low-confirming conditions as the topsoils of grasslands or slopes. Both of the suction-induced cohesion and friction are modeled by using the MCV model, which is a combination of Mohr-Coulombs slip criterion as a friction model and the Vilar model (Vilar, 2006) for suction-induced cohesion. The model is capable of reproducing the shear strength of root-soil interfaces as a function of normal stress and suction. The MCV model is implemented by using the NTS approach (Wriggers, 2006), which is the first of its kind to the best knowledge of the authors. The MCV model is introduced as a slip criterion, and the return-mapping scheme updates total slip. The slip criterion has both suction and soil pressure as variables, therefore, the shear stress of the root-soil interfaces are affected by both hydraulic and mechanical conditions, and such models have not been used for root-soil contact problems.

Chapter 6

Numerical Simulation of Shear Behavior of Root-Soil Interface Under Dynamic Suction Condition

6.1 Introduction

The present chapter demonstrates the applicability and accuracy of the MCV-NTS approach that is displayed in the last chapter. For this purpose, this chapter provides two numerical simulations. First, the pressure-controlled pull-out tests and suction-controlled pull-out tests are simulated, the experiments of which is shown in the previous chapter. The aim of present simulations is to validate the accuracy and stability of the MCV-NTS approach, under dynamic suction conditions. Furthermore, the applicability of the MCV-NTS approach under dynamic suction condition is tested by simulating pulled-out roots under dry-to-wet conditions for different soil pressure conditions. This condition is consistent with the rainfall events, therefore, more realistic conditions. The latter simulation focuses on the accuracy and stability of the present model.

Both of the MCV-NTS formulation and the application to the root-soil contact problems are first of its kind. Sections 2 and 3 validate the MCV-NTS by solving the numerical simulation of pressure-controlled pull-out tests of Section 2 of the last chapter as well as suction-controlled pull-out tests of Section 3 of the last chapter. Further, Section 4 conducts a numerical experiment of pull-out behavior of straight roots under the dynamic change of suction to validate the applicability of the MCV-NTS scheme. Section 5 summarizes the discussions mentioned above.

6.2 Numerical simulation of pressure-controlled pullout test

This section aims to validate the accuracy of the current numerical approach based on MCV model and NTS method through the comparison with the experimental studies. The validation is consist of two parts: (1) numerical simulation of suction-controlled pullout test (see Section 3) with constant soil pressure, and (2) pullout tests of Tomobe et al., (2016) in which the soil pressure is changed and suction is constant.

6.2.1 Initial and boundary conditions

The schematics of the pullout tests are shown the Chapter 5, which is used. It is simulated that a root (8.0 cm $\times$ 0.05 cm) is pulled out from the soil specimen (6.0 cm $\times$ 2.0cm) towards the left sides under the prescribed normal pressure. This condition is consistent with the pullout tests of barley shown in Chapter 3. Before the pullout process, the normal pressure is loaded by enforcing downward displacement on the top of the soil, which is consistent with the experimental condition. The suction is supposed to be constant for each case and given as the environmental valuable since the specimen is small and the evaporation of the soil water is carefully prevented in the experiments. For simplicity, the analysis is conducted with plain strain condition with the unit depth (m), and the shear stress (kPa) on the root-soil interfaces are computed by dividing the pullout forces (N) into the left sides of the roots by the contact area (m^2) of the specimen. Also, for the symmetry on the horizontal line seen in the figure, only the lower half of the system is computed.

The numerical simulation of the pressure-controlled pullout tests is performed as follows: The normal pressure of 1.7, 3.6, 6.3, 8.1 kPa are loaded by prescribing the equivalent displacement. The suction is not explicitly measured in the previous research, and only the apparent cohesion is measured (3.14 kPa). Thereby, the value of suction is estimated by using the MCV model and the parameters which are measured in Section 3. As a result, the suction is estimated as 0.27 kPa. For simplicity, this analysis uses the value for all stress conditions and assumes that the suction is almost the same for the cases. The mesh and boundary conditions are visible in Fig. 6.1 Both roots and soils are supposed to be hyperplastic material, and the root-soil interfaces are governed by the MCV model seen in Section 5. The hyperplastic constitutive equation presented by Vladimirov et al. (2008, 2010) is utilized for its simplicity since the current paper focuses on the interfacial behavior and the deformation of roots and soils are relatively small. The material parameters of soils are obtained by the consolidation process of the current pullout tests, and these of roots are measured by the bending tests of soybean roots, which has similar mechanical behavior with the barley roots utilized in the pressure-controlled pull-out tests. The Poissons ratio of soil is taken by the relationship between the normal stress and vertical stress during the pullout tests, and soils are supposed to be the same value for simplicity. The model param-

eters are seen in Table 5.3, where the model parameters of the MCV model is consistent with Section 3.

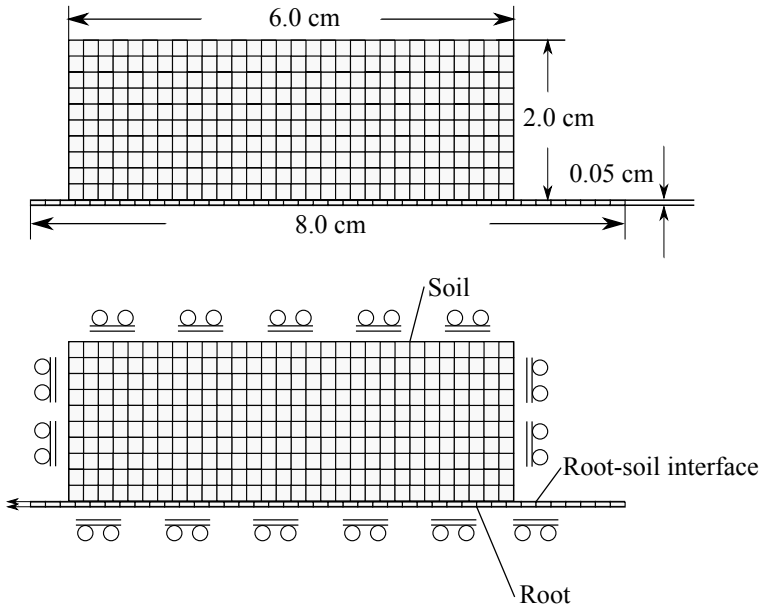

Figure 6.1: Mesh and Boundary condition of numerical simulations for pull-out test in latter sections.

6.2.2 Results and discussion

Fig. 6.2 compares the profile of shear stress of the root-soil interfaces in simulations and experiments of the pressure-controlled pullout tests. The simulations are the almost same as the experiment for all stress conditions. Although the initial (displacement is 0 to 3 mm) angle of the displacement-stress curve of simulation is larger than the ones of the experiment, the gap closes when slip starts (displacement is 3 mm to 8 mm). Therefore, the MCV model and NTS approach are capable of simulating the slip in root-soil interfaces under changing suction and soil pressure.

The contour of the deviatoric stress is visible in Fig 6.3 which is predicted by the simulation. As can be seen, the deviatoric stress of soil domain increases with the increase of soil pressure; this result is natural since it indicates that the shear stress of the root-soil interfaces increases due to the soil pressure and hence roots and soils are mechanically connected.

Above all, the MCV model can reproduce the shear strength root-soil interfaces observed by the experiment ass a function of normal stress and suction. The model can also provide an accurate solution of the pullout tests under different conditions of suction, which is the first of its kind to the best of our knowledge. Since the MCV model consistently expresses the shear strength of root-soil interfaces under changing wet-dry conditions and

allows large slip, it can apply to the large-deformation problems of rooted soil under changing hydro-mechanical conditions.

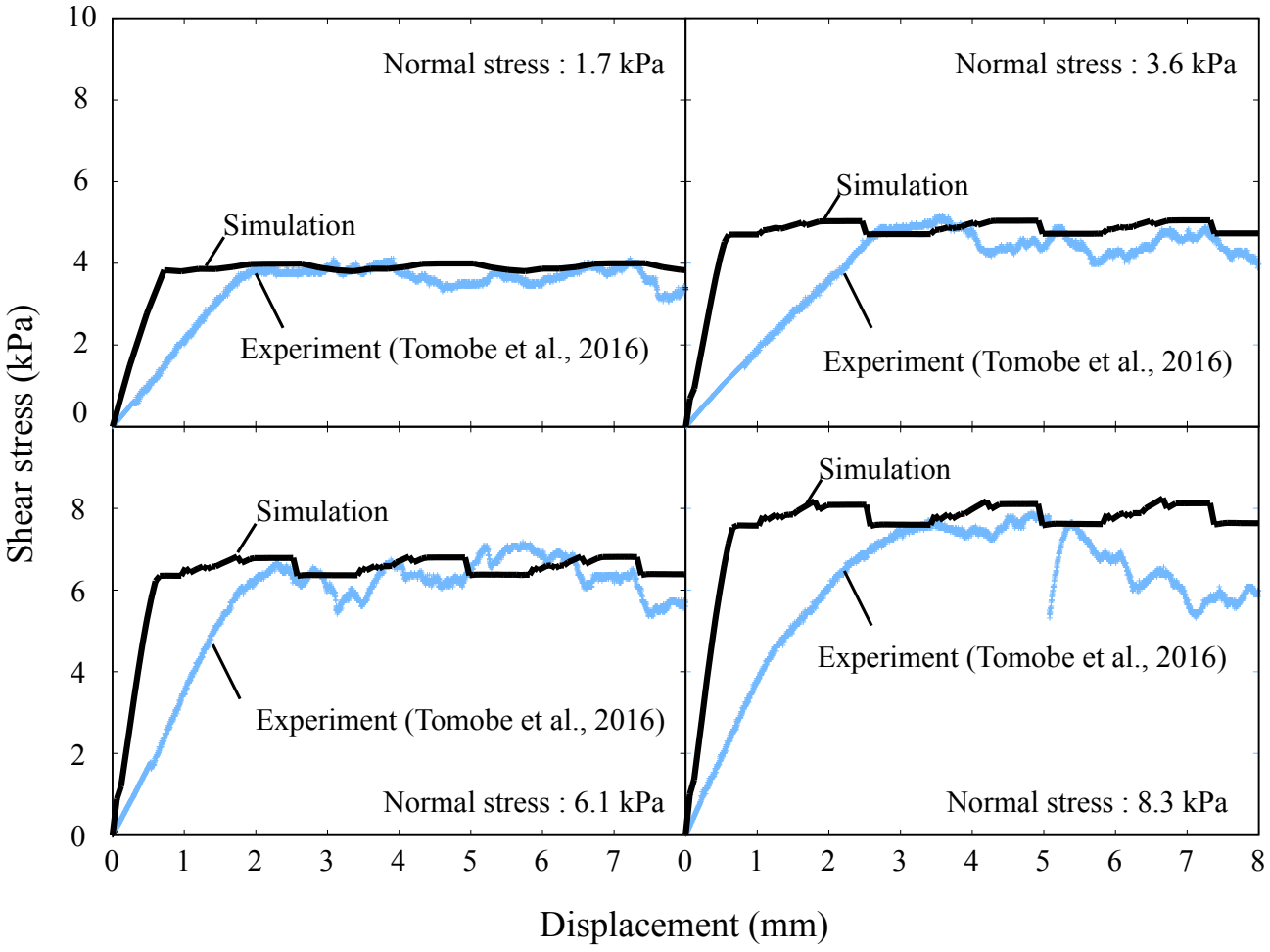

Figure 6.2: Validation of simulation with comparison to experiments under pressure-controlled condition, where the suction is not changed.

6.3 Numerical simulation of suction-controlled pullout test

The objective of this section is to validate the accuracy of the current numerical approach based on the MCV model and NTS method through the comparison with the experimental studies presented in Chapter 5. Since the MCV-NTS approach models shear strength of root-soil interfaces under changing soil pressure and suction, the validation presented in this section is consist of six suction conditions.

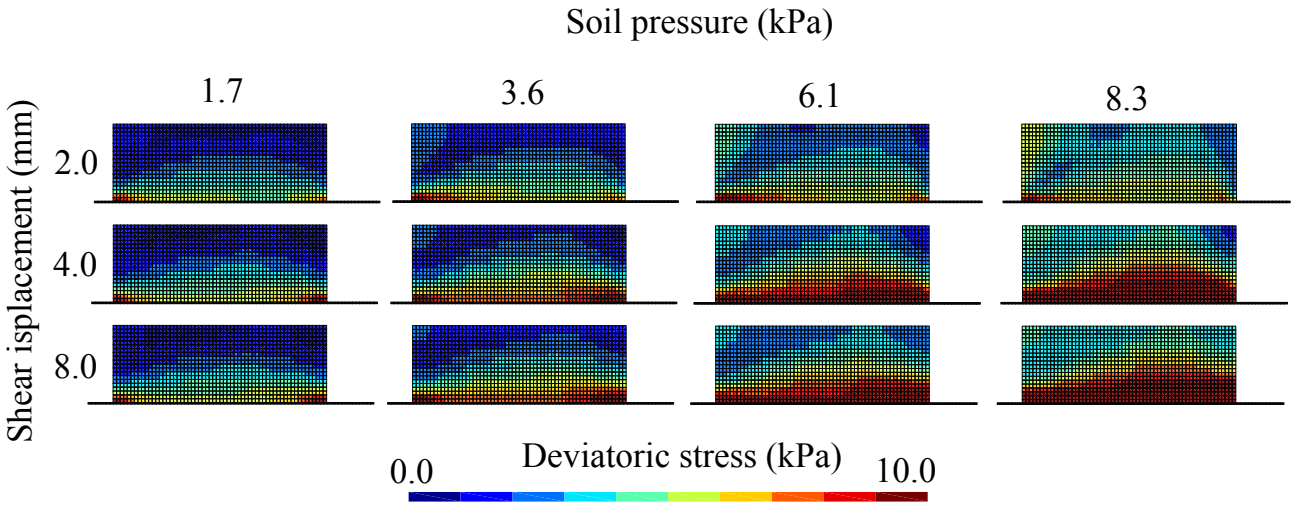

Figure 6.3: Contour map of deviatoric stress of soil and root domains. Shear stress of soil domain increases with the increase of soil pressure.

6.3.1 Mesh and boundary conditions

The mesh and boundary conditions of the suction-controlled pullout tests are shown in Fig. 6.1, which is common in all below cases. The lower half of the specimen is modeled and each case simulates the process that a root (8.0 cm $\times$ 0.05 cm) is pulled out from the soil specimen (6.0 cm $\times$ 2.0 cm) towards the left sides under the prescribed suction: The diameter of the root in the numerical simulation is identical to the experimental conditions seen in Chapter 5. Preliminary, initial conditions are prepared by uniform loading downward displacement on the top of the soil domain. For simplicity, the analysis is also conducted with plain strain condition and the shear stress on the root-soil interfaces is derived by dividing the pullout forces (N) on the left sides of the roots by the contact area (m^2) of the specimen as explained in Chapter 3. Both roots and soils are supposed to be hyperplastic material, and the root-soil interfaces are governed by the MCV equation seen in Section 5. The hyperplastic constitutive equation presented by Vladimirov et al. (2008, 2010) is utilized for its simplicity since the current paper focuses on the interfacial behavior and the deformation of roots and soils are relatively small. The Young's modulus of soil is obtained by the unconfined compression tests (JIS A 1216) where the E_{50} value is utilized as Young's modulus, and these of roots are measured by the bending tests of soybean roots, which has similar mechanical behavior with the barley roots. The Poissons ratio of soil is taken by the relationship between normal stress and vertical stress during the pullout tests, and soils are supposed to be the same value for simplicity. The model parameters are seen in Table 5.3, where the model parameters of the MCV model is consistent with Section 3.

This chapter assumes that the suction of the root-soil interfaces is spatially uniform, however, special considerations are necessary when the MCV-NTS is applied to situations

where the suction is not spatially uniform. The suction is supposed to be constant all over the interfaces since the root-soil interface is horizontal and the change of the soil water content is carefully prevented in the presented experiments. If the MCV-NTS is applied for more practical situations where the suction is in a spatially non-uniform, suction of root-soil interfaces are to be determined consistently. One of the consistency condition is that the consistency of the suction of root-soil interfaces with the suctions of root/soil domains in the vicinities. Since the root and soil domains contacts in the interface, a unique suction should be determined at the material points on the root-soil interfaces: it requires mathematical constraints that minimize the gap of suction between root surfaces and soil surfaces at each of the root-soil contact points. A possible solution for this problem is to introduce a penalty method or Lagrange multiplier method to enforce the gap-minimizing constraint, which is analogous to the thermal contact simulation (Wriggers, 2006) where the temperature gap between two surfaces is successfully minimized.

The numerical simulation of the suction-controlled pullout tests is performed as follows: The numerical simulation of the suction-controlled pullout tests are simulated as below: The suction of 0.5, 4.4, 5.8, 8.8, 22.0, and 28.0 kPa are applied, and the normal pressure is considered as 0 kPa. This condition is implemented by following; the top of the soil-mesh is vertically fixed, and a slight penetration (0.01 mm) is given in the root-soil interfaces at the initial condition. For simplicity, this analysis uses the value for all stress conditions and assumes that the suction is almost the same for the cases.

6.3.2 Results and discussion

Fig 6.4 shows the relationship between displacement and shear strength for each suction: (a) 0.5 kPa, (b) 4.4 kPa, (c) 5.8 kPa, (d) 8.8 kPa, (e) 22.0 kPa and (f) 28.0 kPa. Through all cases, profiles of both simulations and experiments are quantitatively similar, and the shear strength of the root-soil interfaces are almost the same. Consequently, the results suggest that the MCV-NTS approach is capable of predicting the shear stress of root-soil interfaces under changing suction.

Fig. 6.5 illustrates a contour map of deviatoric stress given by the numerical simulation of pullout tests. From root to soil, propagation of deviatoric stress is cut off when the suction is small enough (suction = 0.5 kPa). When the suction is 5.8 kPa, the deviatoric stress of soil is not considered when the displacement is relatively small. However, it increases when the displacement is large (> 2.0 mm). The deviatoric stress of soils in case that suction is 28.0 kPa is significantly large and continuously distributes across root-soil interfaces.

Although both contour maps of Figs. 6.3 and 6.5 are similar, an important difference appears between them. In the case of Fig. 6.5, the contour lines of the deviatoric stress are parallel with each other and symmetry concerning the center of the figure. By contrast, the contour line of Fig. 6.3 is more complex and not symmetry. This difference can be

explained as below: The suction-induced cohesion is independent with the stress field, therefore, under small soil-pressure condition, the shear stress of root-soil interfaces are uniformly distributed. On the other hand, the soil-pressure-induced friction depends upon the stress field of both soils and roots and the deformation of the roots and soils at the right sides are different from the left sides, thereby, the complexity and asymmetry are observed.

Above all, it is indicated that the MCV model can reproduce the shear strength root-soil interfaces observed by the experiment as a function of normal stress and suction. The model can also provide an accurate solution of the pullout tests under different conditions of suction, which is the first of its kind to the best of our knowledge. Since the MCV model consistently expresses the shear strength of root-soil interfaces under changing wet-dry conditions and allows large slip, it can apply to the large-deformation problems of rooted soil under changing hydro-mechanical conditions. The MCV-NTS approach is compatible with any FEM schemes if one uses the linear elements such as triangular or rectangular elements. Besides, since the NTS formulation is also presented for 3D analysis as well as 2D, it is expected that the MVC-NTS scheme can also be applicable for root-soil contact problems under 3D conditions to simulate the deformation of rooted soils under prescribed suction conditions.

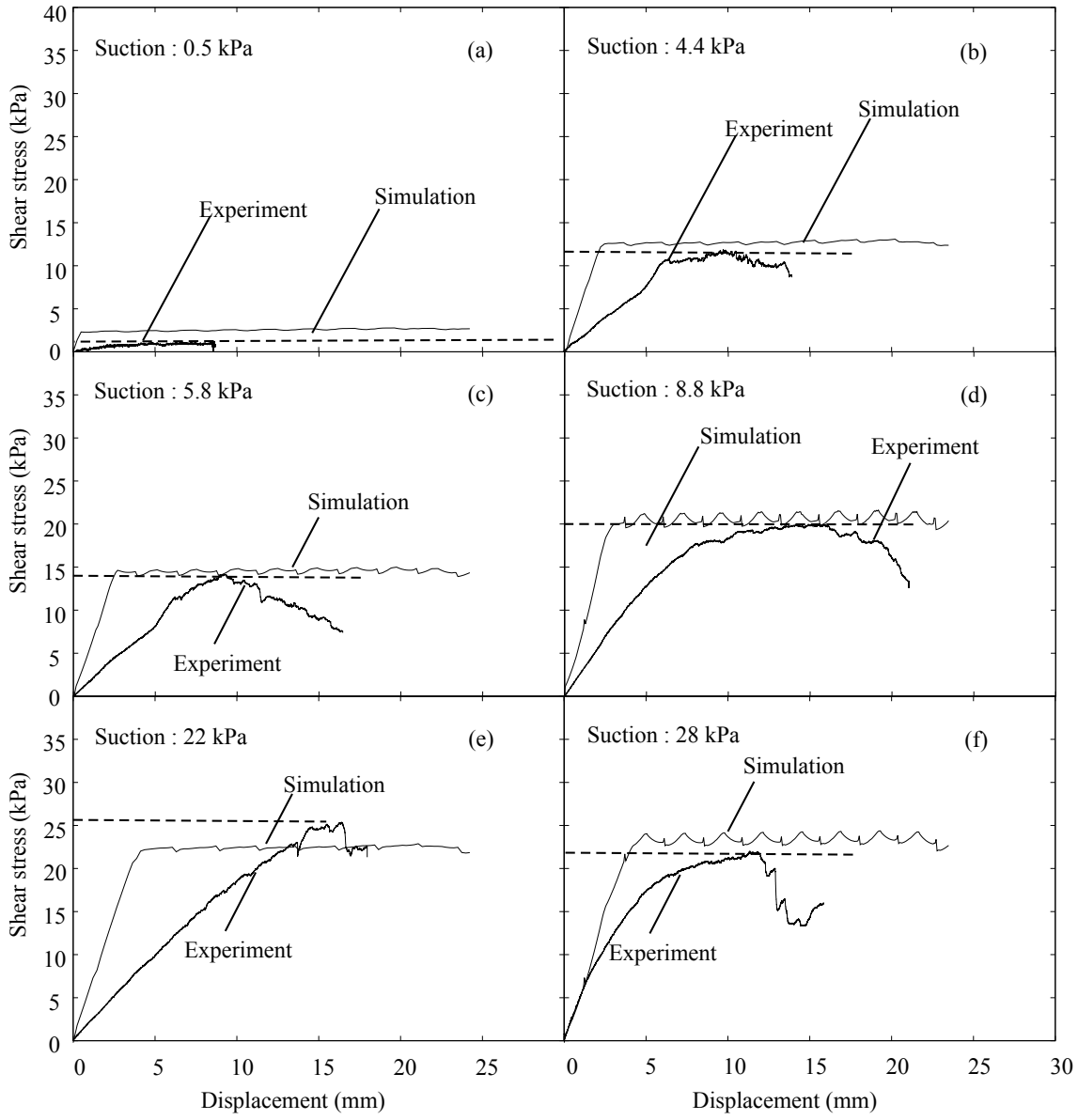

Figure 6.4: Validation of simulation with comparison to experiments under suction-controlled condition, where the soil pressure is not changed.

6.4 Pullout resistance of root under changing pressure/suction by MCV-NTS approach

The objective of this numerical experiment is to investigate the applicability of MCV-NTS approach, where pull-out problems of roots from soils under dynamic suction conditions for different soil pressure are simulated to test (1) whether the numerical simulation can continuously predict the shear stress of root-soil interfaces under dynamic suction conditions

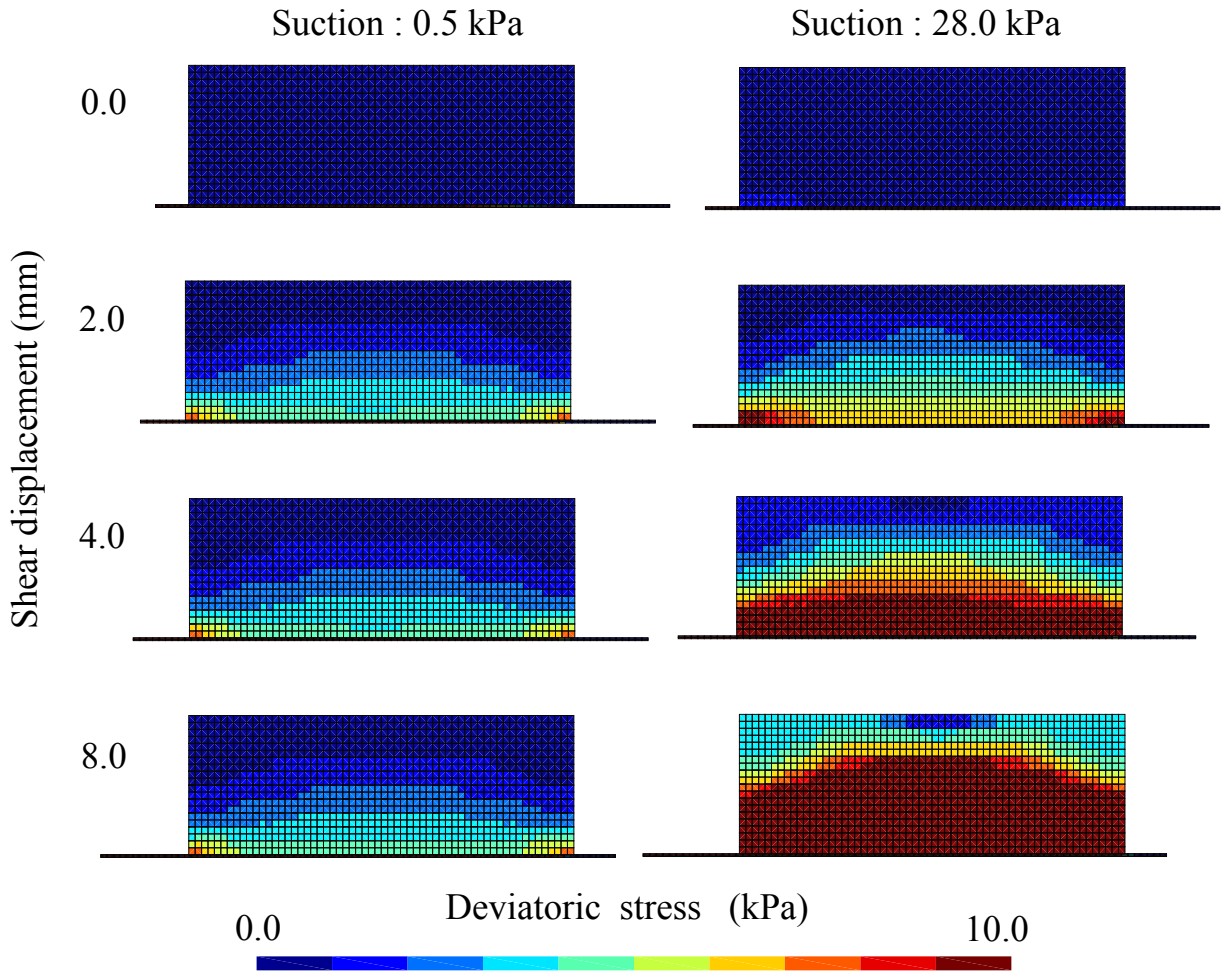

Figure 6.5: Contour map of deviatoric stress of soil and root domains. Shear stress of soil domain increases with the increase of suction.

or not, and (2) whether the simulation works under realistic and unconfined conditions of shallow soil depth. The problem described in this section is designated to demonstrate the pull-out behavior of roots from the soil as illustrated in Fig. 5.1 under more realistic conditions than previous sections. The previous sections show that the current numerical method can accurately predict the shear strength of the root-soil interface for different soil pressures, and also predict the shear strength for different suctions. Each of these simulations is validated through the comparison with the experiments, however, it remains still unclear whether the current method can provide reasonable prediction through the dynamic change of suction under different soil pressures or not. It is expected that the current method provides shear strength for each condition in every time based on the MCV model, however, the solution may not converge when the suction-induced cohesion is frequently changed. There is another question that the how stress field of soil is changed due to the dynamic change of suction-induced cohesion; noting that the suction is fixed during the pull-out process in the cases of previous sections.

6.4.1 Boundary conditions and suction control

From these standpoints, this section prepares three cases of simulations. The soil pressures are equivalent to the soil depth of 30 cm, 60 cm, and 90 cm: These soil pressures are computed from the bulk density (1.28 g/cm^3) of the sampling site of soils (Table 5.3), and loaded as pre-stress. For each case, a root is pulled out from soil for 1.6 cm, and the suction is set at 28.0 kPa during the shear displacement is 0.0 cm to 0.6 cm, in which the roots start slipping. The suction of 28.0 kPa is selected since (1) the simulation of drying process is appropriate for evaluating the applicability of the MCV-NTS scheme since the suction is dynamically changed, and (2) the suction-induced cohesion is almost maximized at the suction in the present combination of roots and soils, hence, the suction can be significantly declined. After the slip is observed, the suction is controlled so that the suction declines from 28.0 kPa to 5.5 kPa during the shear displacement is 0.6 cm to 1.6 cm, where the roots are slipping on the soils and the shear strength of root-soil interfaces declines as the shear displacement increases. It is expected that the stress state of root-soil interfaces is inside of the MCV slip surface at the initial condition and then moves on the MCV slip surface and remains on the same point before the suction is changed; afterward, the stress state moves along the MCV slip surface during the dynamic suction decline. The mesh and boundary conditions are identical to Section 5 and the pre-stress is set so that the soil pressure is the same as that of 0.3, 0.6 and 0.9 depth of the sampling site. The depth is utilized since the roots are distributed in the 0.0 to 1.0 m depth in the sampling site and similar conditions are reproduced in the simulation.

6.4.2 Demonstration of pullout behavior under dry-to-wet condition

Fig. 6.6 shows the stress-path of the simulation for three cases; the Fig. 6.6(a) shows the slip criterion of the MCV model which represents the shear strength for given soil pressure and suction, and Fig. 6.6(b) and (c) display the pathway of the shear stress in the relation of suction and soil pressure, respectively. Fig. 6.6 (d) presents that the soil pressure is mostly fixed for each case and the suction is dynamically changed during the pull-out process. As can be seen in the Fig, 6.6 (b), the stress state of root-soil interfaces is inside of the MCV slip surface at initial condition and then moves on the MCV slip surface and remains on the same point before the suction is changed; afterward, the stress state moves along hyperbolic curve of MCV model during the dynamic suction decline, which consistent with the MCV model. The shear strength in case of depth = 90 cm is greater than depth = 30 cm, which visualizes the contribution of friction, amount of which is also consistent with the MCV model and the pull-out experiments. According to Fig. 6.6 (c), the stress state of root-soil interfaces is also inside of the MCV slip surface at initial condition and then also moves on the MCV slip surface and remains on the same point before the suction is changed; after the suction starts declining, the Mohr-Coulomb line shrinks due to the decline of suction-induced cohesion, which is also consistent with the MCV model and suction-controlled pull-out tests. The above relationship is described in Fig. 6.6 (a) and the profile of shear stress are visualized with the MCV surface.

Fig. 6.7 visualizes the shear stress-displacement curve, suction-displacement curve, and soil pressure-displacement curve: The stress contour of the deviatoric stress is also exhibited. As the displacement is increased, the shear stress of the root-soil interfaces reaches the shear strength which is defined by the MCV model. At the failure, which indicates the slip, the displacement increases under the same shear stress. As can be seen, the shear stress of the depth = 0.9 m is greater than that of the depth = 0.3 cm; the difference reflects the contribution of friction-induced by soil pressure. The profile of soil pressure is shown in the left bottom of the figure, where the soil pressure is kept at an almost constant value for each case during the numerical experiment. When the displacement reaches 0.6 cm, the suction is artificially reduced, which expresses that the root-soil interface is gradually moistened. The decline of the suction lessens the suction-induced cohesion, which results in declines of shear stress during the slip. The right side of the figure visualizes the contour map of the deviatoric stress of both root and soil domains. The deviatoric stress of the bottom of the soil domain is increased as the displacement increases from 0.01 cm to 0.20 cm, then the stress contour keeps almost the same color during the displacement is 0.20 cm to 0.80 cm. Afterward, the zone of deviatoric stress $\geq$ 30.0 kPa shrinks as time passes, which is due to the decline of the suction. Although a little oscillation of the solution is observed, the degree of the oscillation is enough small from the standpoint of practical uses.

Another important point is seen in the topology of the contour of the deviatoric stress

in Fig.6.7, where the profile of the contour is similar to the ones of the simulation of soil-pressure-controlled pull-out tests, where the soil-pressure-induced friction is dominated. In detail, the gradient of the contour is enhanced and more complex. This indicates that the friction induces the spatial complexity of the stress field and the suction-induced cohesion enhances the spatial complexity.

From these results, the NTS-MCV approach can provide a reasonable solution for root-soil contact problems under dynamic change of suction for different soils. The results indicate that the current approach can be applicable for root-soil contact problems and provides consistent solution based on the MCV model. The proposed approach enhances the accuracy of the numerical simulation of deformation in rooted soils based on FE analysis (Dupuy et al., 2007; Rahardjo et al, 2009; Mickovski et al., 2010).

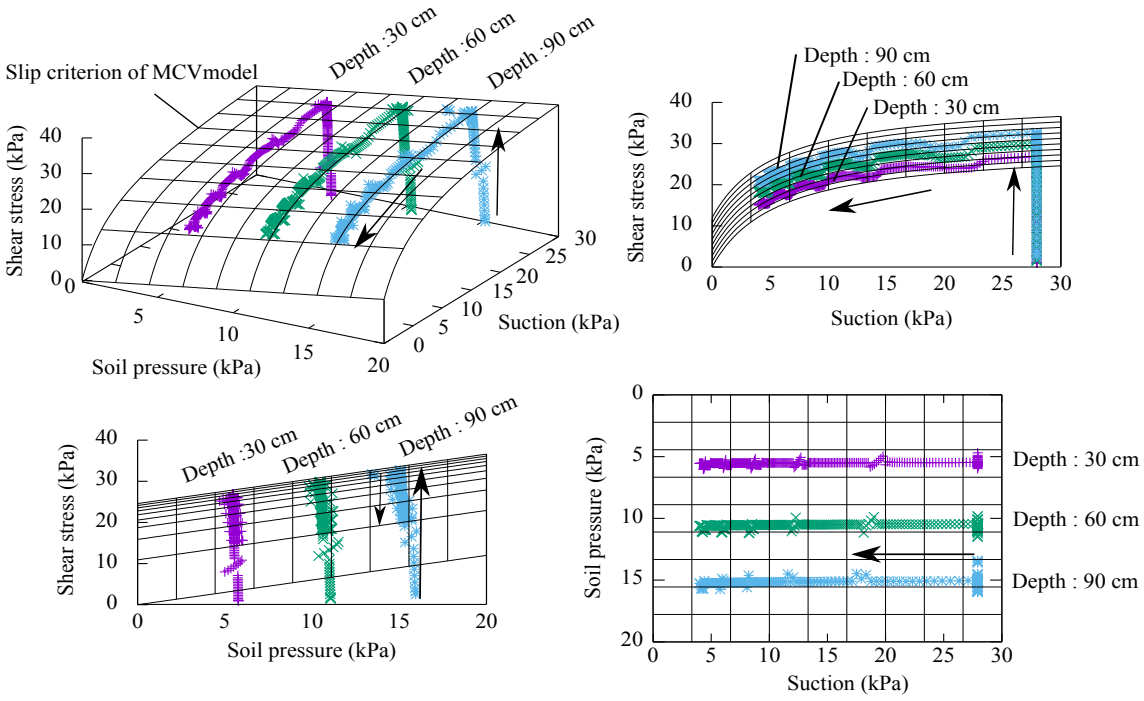

Figure 6.6: Stress path plotted with MCV surface under dynamic suction conditions for different soil pressure conditions. The soil pressures are equivalent to that of the depth of 30.0, 60.0 and 90.0 cm from the ground surfaces.

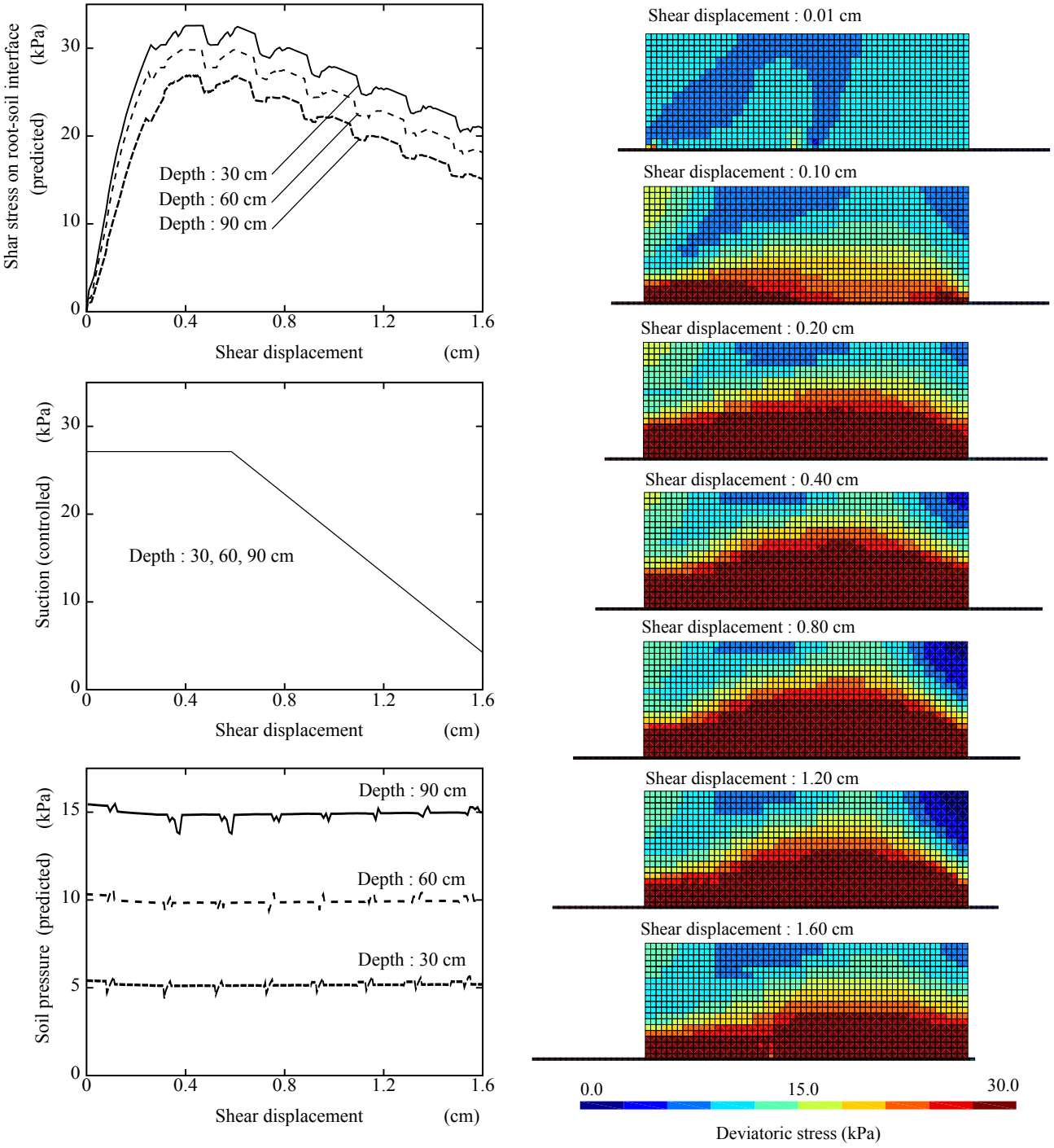

Figure 6.7: Profiles of shear stress of root soil interfaces and deviatoric stress of root and soil.

6.5 Summary

The current chapter presents that the MCV model and NTS approach can successfully simulate the deformation and the shear strength of rooted soils. The conclusion is drawn below.

The current simulation code is validated by simulating the pull-out tests under pressure-controlled conditions and suction-controlled conditions. The results show that the current model and implementation can accurately reproduce the relationship between shear stress and displacement for both of the pressure-induced friction and the suction-induced cohesion. The results also visualize the deviatoric stress under different suctions, and the results suggest that the propagation of shear stress from the roots to the soils is cut off when the suction is almost zero and it continuously proper gates as suction increases. It is an important suggestion since the distribution of the deviatoric stress can be changed due to the presence of the suction-induced cohesion in the root-soil interfaces.

A numerical experiment of pulling-out of roots is performed to evaluate the applicability to the dynamic suction conditions where the suction of root-soil interfaces is changed during the pull-out process. The results indicate that the NTS-MCV approach can provide reasonable solutions for root-soil contact problems under dynamic change of suction for different soils. The results indicate that the current approach can be applicable for root-soil contact problems and provides consistent solution based on the MCV model. Accurate modeling shear strength of root-soil interfaces under changing soil pressure and suction has been required to solve root-soil contact problems based on FEM (Dupuy et al., 2008; Rahardjo et al, 2009; Mickovski et al., 2010), and proposed method consistently provides a series of experiment, modeling, and implementation addressing with this problems by a possible simplest way.

Chapter 7

Concluding Remarks

7.1 Summary

This thesis proposes a series of experiments, constitutive models, and numerical approaches to simulate the contact problem between roots and soils accurately. Chapter 2 proposes an NTS-FEM formulation and a solution algorithm, where the CCM and the finite elasto-plasticity is consistently combined. Chapter 3 presents an apparatus and a protocol to measure friction and cohesion of root-soil interfaces. The results show that the proposed methods can measure both of frictional coefficient and the cohesion of root-soil interfaces and indicated that the elasto-plasticity and Mohr-Coulomb model is applicable for the stick-slip phenomena of root-soil interfaces. This apparatus and procedure are utilized with the continuum model of Chapter 2, as shown in Chapter 4, in order to simulate the pull-out tests of Chapter 3 and the lodging problem. Through the comparison between simulations and experiments, it is suggested that the current method precisely simulate root-soil contact problems in both mesoscale and plant-scale ones. Chapter 5 and 6 extends the Mohr-Coulomb model for expressing suction-induced cohesion and, for this purpose, a novel pull-out apparatus is presented. The apparatus controls the suction of the root-soil interface. Hence, the relationship between suction and suction-induced cohesion is measured. The results are modeled by employing Vilar's model (Vilar, 2006), and a numerical method for simulating root-soil contact problem under dynamic suction conditions are presented by combining the MCV model with the NTS approach. It is seen in the results that the proposed method accurately reproduces suction-induced cohesion under dynamic suction conditions, and the wet-to-dry condition is successfully expressed in root-soil contact simulations. It is worth noting that the root-soil contact problems under dynamic suction conditions are not solved in the previous researches Dupuy (2007) and Michovski (2011).

7.2 Future study

Future studies will apply the experimental and numerical methods to predict the mechanical strength and deformation behavior of rooted soil to utilize the root-induced reinforcement for soils. As can be seen in Chapters 3 and 4, the present method only utilizes small specimens to measure the material parameters. Therefore, it is not costly to perform experiments and numerical analysis. Further, by using mesh-models created from root-generation algorithms, such as L-systems, it is also possible to conduct root-soil contact analysis for practical slope-stability problems. Although the computational costs are significant when the proposed numerical scheme is utilized for slope-scale issues, it is possible to introduce parallelization to accelerate simulations. Future studies will also conduct numerical simulations of lodging to find optimal root shapes to design root phenotypes for preventing root lodging of cereals. The presented methods can accurately simulate the lodgings of crops, as shown in Chapter 4. Hence, the next target will be the utilization of the modern approach to design and selection in terms of breeding to minimize the lodging. The numerical scheme will also useful for bio-inspired engineering to develop optimal designs of pile-structures. Root morphology is considered to be optimized for supporting upper-gound structures. However, it has been few applications of the morphology to pile structures. The proposed scheme will be utilized for investigating the essence of the root-shapes and also will apply the mechanism of the roots for optimal designs for geotechnical structures.

References

Abe, K., and Ziemer, R.R. 1991. Effect of tree roots on a shear zone: modeling reinforced shear stress. Canadian Journal of Forest Research, 21(7): 1012−1019.

Ali, F.H., and Osman, N. 2008. Shear strength of a soil containing vegetation roots. Soils and Foundations, 48(4): 587−596.

Baker, C.J., Berry, P.M., Spink, J.H., Sylvester-Bradley, R., Griffin, J.M., Scott, R.K., and Clare, R.W. 1998. A method for the assessment of the risk of wheat lodging. Journal of Theoretical Biology, 194(4): 587−603.

Baker, C.J., Sterling, M., and Berry, P. 2014. A generalised model of crop lodging. Journal of Theoretical Biology, 363: 1−12.

Berry, P.M., Sterling, M., Spink, J.H., Baker, C.J., Mooney, S.J., Tams, A.R., Ennos, A.R., Rosemaund, A., Wynne, P., and Hr, H. 2004. Understanding and reducing lodging in cereals. Advances in Agronomy, 84(4): 217−271.

Berry, P.M., Spink, J., Sterling, M., and Pickett, A.A. 2003. Methods for rapidly measuring the lodging resistance of wheat cultivars. Journal of Agronomy and Crop Science, 189(6): 390−401.

Bischetti, G.B., Chiaradia, E.A., DAgostino, V., and Simonato, T. 2010. Quantifying the effect of brush layering on slope stability. Ecological Engineering, 36(3): 258−264.

Bizet, F., Bengough, A.G., Hummel, I., Sciences, E., and Dd, D. 2018. 3D deformation field in growing plant roots reveals both mechanical and biological responses to axial mechanical forces. 67(19): 5605−5614.

Das, G.K., Hazra, B., Garg, A., and Ng, C.W.W. 2018. Catena Stochastic hydro-mechanical stability of vegetated slopes : An integrated copula based framework. 160(March 2017): 124−133.

Docker, B.B., and Hubble, T.C.T. 2008. Quantifying root-reinforcement of river bank soils by four Australian tree species. Geomorphology, 100: 401−418.

Dupuy, L.X., Mimault, M., Patko, D., Ladmiral, V., Ameduri, B., Macdonald, M.P., and Ptashnyk, M. 2018. ScienceDirect Micromechanics of root development in soil. Current Opinion in Genetics & Development, 51: 18−25. Elsevier Ltd.

Dupuy, L.X., Fourcaud, T., Lac, P., and Stokes, A. 2007. A generic 3D finite element model of tree anchorage integrating soil mechanics and real root system architecture. American Journal of Botany, 94(9): 1506−1514.

Eab, K.H., Likitlersuang, S., and Takahashi, A. 2015. Laboratory and modelling investigation of root-reinforced system for slope stabilisation. Soils and Foundations, 55(5): 1270−1281. Elsevier.

Endo, T. 1980. Effect of tree roots upon the shear strength of soil. Forest and Forestry Products Research Institute, 14(2): 112−115.

Fan, C., and Su, C. 2009. Effect of soil moisture content on the deformation behaviour of root-reinforced soils subjected to shear. (132): 57−69.

Fredlund, D.G., Anqing Xing, Fredlund, M.D., B.S.L. 1996. The relationship of the unsaturated soil shear strength to the soil-water characteristic curve. Canadian Geotechnical Journal, 32: 440−448.

Freer, R. 1991. Bio-engineering: the use of vegetation in civil engineering. Construction and Building Materials, 5(1): 23−26.

Geuzaine, C., and Remacle, J.-F. 2009. Gmsh: A 3-D finite element mesh generator with built-in pre- and post-processing facilities. International Journal for Numerical Methods in Engineering, 79(11): 1309−1331.

Giadrossich, F., Stokes, A., Schwarz, M., Cohen, D., Cislaghi, A., Vergani, C., Hubble, T., and Phillips, C. 2017. Methods to measure the mechanical behaviour of tree roots : A review. Ecological Engineering, 109(November): 256−271. Elsevier.

Gray, D.H., and Ohashi, H. 1983. Mechanics of fiber reinforcement in sand. Journal of Geotechnical Engineering, 109(3): 335−353.

Hashiguchi, K., and Yamakawa, Y. 2013. Introduction to finite strain theory for continuum elasto-plasticity. WILEY.

Hejazi, S.M., Sheikhzadeh, M., Abtahi, S.M., and Zadhoush, A. 2012. A simple review of soil reinforcement by using natural and synthetic fibers. Elsevier Ltd.

Huang, R., Becker, A.A., and Jones, I.A. 2012. Modelling cell wall growth using a fibre-reinforced hyperelasticviscoplastic constitutive law. Journal of the Mechanics and Physics of Solids, 60(4): 750−783. Elsevier.

Hudek, C., Sturrock, C.J., Atkinson, B.S., Stanchi, S., and Freppaz, M. 2017. Root morphology and biomechanical characteristics of high altitude alpine plant species and their potential application in soil stabilization. Ecological Engineering, 109: 228−239. Elsevier B.V.

Hughes, T.J.R., Taylor, R.L., Sackman, J.L., Curnier, A., and Kanoknukulchai, W. 1976. A finite element method for a class of contact-impact problems. Computer Methods in Applied Mechanics and Engineering, 8: 249−276.

Ji, X., Cong, X., Dai, H., Zhang, A., and Chen, L. 2018. Studying the mechanical properties of the soil-root interface using the pullout test method. Journal of Mountain Science, 15(3): 309−322.

Jotisankasa, A., and Rurgchaisri, N. 2018. Geotextiles and Geomembranes Shear strength of interfaces between unsaturated soils and composite geotextile with polyester yarn rein-

forcement. Geotextiles and Geomembranes, 46(3): 338−353. Elsevier.

Kim, G.W., Kim, M.S., Do, G.S., Kang, S.W., Lee, S.H., Sagara, Y., Lee, I.B., and Bae, Y.H. 2008. Determination of the Viscoelastic Properties of Apple Flesh under Quasi-Static Compression Based on Finite Element Method Optimization. Food Science and Technology Research, 14(3): 221−231.

Kiyota, T., Soma, R., Munoz, H., Kuroda, T., Ohta, J., Harata, M., and Tatsuoka, F. (2009). Pullout behaviour of geo-cell placed as reinforcement in backfill. Geosynthetics Engineering Journal 24(0), 75-82.

Liang, T., Bengough, A.G., Knappett, J.A., MuirWood, D., Loades, K.W., Hallett, P.D., Boldrin, D., Leung, A.K., and Meijer, G.J. 2017. Scaling of the reinforcement of soil slopes by living plants in a geotechnical centrifuge. Ecological Engineering,.

Liu, H.W., Feng, S., and Ng, C.W.W. 2016. Computers and Geotechnics Analytical analysis of hydraulic effect of vegetation on shallow slope stability with different root architectures. 80: 115−120.

Liu, W.N., Meschke, G., and Mang, H.A. 2003. Algorithmic stabilization of FE analyses of 2D frictional contact problems with large slip. Computer Methods in Applied Mechanics and Engineering, 192(16−18): 2099−2124.

Mickovski, S.B., Bransby, M.F., Bengough, A.G., Davies, M.C.R., and Hallett, P.D. 2010. Resistance of simple plant root systems to uplift loads. Canadian Geotechnical Journal, 47(1): 78−95.

Mickovski, S.B., Stokes, A., Beek, R. Van, Ghestem, M., and Fourcaud, T. 2011. Simulation of direct shear tests on rooted and non-rooted soil using finite element analysis. Ecological Engineering, 37(10): 1523−1532. Elsevier B.V.

Muir Wood, D., Diambra, A., and Ibraim, E. 2016. Fibres and soils: A route towards modelling of root-soil systems. Soils and Foundations, 56(5): 765−778. Elsevier.

Ng, C.W.W., Woon, K.X., Leung, A.K., and Chu, L.M. 2013. Experimental investigation of induced suction distribution in a grass-covered soil. 52: 219−223.

Ni, J.J., Leung, A.K., Ng, C.W.W., and Shao, W. 2018. Computers and Geotechnics Modelling hydro-mechanical reinforcements of plants to slope stability. 95: 99−109.

Ookawa, T., Hobo, T., Yano, M., Murata, K., Ando, T., Miura, H., Asano, K., Ochiai, Y., Ikeda, M., Nishitani, R., Ebitani, T., Ozaki, H., Angeles, E.R., Hirasawa, T., and Matsuoka, M. 2010. New approach for rice improvement using a pleiotropic QTL gene for lodging resistance and yield. Nature Communications, 1(8). Nature Publishing Group. doi:10.1038/ncomms1132.

Peric, D., and Owen, D.R.. 1992. Computational model for 3-D contact problems with friction based on the penalty method. International Journal for Numerical Methods in Engineering, 35: 1289−1309.

Rahardjo, H., Harnas, F.R., Indrawan, I.G.B., Leong, E.C., Tan, P.Y., Fong, Y.K., and Ow, L.F. 2014. Understanding the stability of Samanea saman trees through tree pulling,

analytical calculations and numerical models. Urban Forestry and Urban Greening, 13(2): 355−364.

Rahardjo, H., Harnas, F.R., Leong, E.C., Tan, P.Y., Fong, Y.K., and Sim, E.K. 2009. Tree stability in an improved soil to withstand wind loading. Urban Forestry and Urban Greening, 8(4): 237−247. Elsevier.

Schwarz, M., Cohen, D., and Or, D. 2011. Pullout tests of root analogs and natural root bundles in soil: Experiments and modeling. Journal of Geophysical Research, 116(2): 1−14.

Shimada, H., Kono, Y., Takada, Y., Sakai, T., and Shimada, S. 2002. Evaluation of root lodging resistance in soybean (Glycine max (L.) Merr.) cultivers by measurement of pushing resistance and top weight moment. Breeding Research,: 185−191.

Simo, J.C., and Taylor, R.L. 1986. A returning mapping algorithm for plane stress elastoplasticity. International Journal for Numerical Methods in Engineering, 22(July 1985): 649−670.

Song, L., Li, J.H., Zhou, T., and Fredlund, D.G. 2017. Experimental study on unsaturated hydraulic properties of vegetated soil. 103: 207−216.

Tomobe, H., Fujisawa, K., and Murakami, A. 2016. Shear tests and modeling of root-soil contact interface by using novel pullout test. IDRE Journal, 84(3): 223−232.

Uesugi, M, and Kishida, H. 1986. Influential factors of friction between steel and dry sands. Soils and Foundations, 26(2): 3346.

Vilar, O.M. 2006. A simplified procedure to estimate the shear strength envelope of unsaturated soils. Canadian Geotechnical Journal, 43(10): 1088−1095.

Vladimirov, I.N., Pietryga, M.P., and Reese, S. 2008. On the modelling of non-linear kinematic hardening at finite strains with application to springbackcomparison of time integration algorithms. International Journal for Numerical Methods in Engineering, 75: 1−28.

Vladimirov, I.N., Pietryga, M.P., and Reese, S. 2010. Anisotropic finite elastoplasticity with nonlinear kinematic and isotropic hardening and application to sheet metal forming. International Journal of Plasticity, 26(5): 659−687.

Wriggers, P., and Haraldsson, A. 2003. A simple formulation for two-dimensional contact problems using a moving friction cone. Communications in Numerical Methods in Engineering, 19(4): 285−295.

Wriggers, P., Krstulovic-Opara, L., and Korelc, J. 2001. Smooth C1-interpolations for two-dimensional frictional contact problems. International Journal for Numerical Methods in Engineering, 51(12): 1469−1495.

Wriggers, P. 2006. Computational contact mechanics. In Springer, 2nd edition. Springer Berlin Heidelberg, Berlin, Heidelberg.

Wriggws, P., Van, T.V., and Stbin, E. 1990. Finite element formulation of large deformation impact-contact problems with friction. Computers & Structures, 37(3): 319−331.

Wu, S., Zhang, S., Guo, C., and Xiong, L. 2017. A generalized nonlinear failure crite-

rion for frictional materials. Acta Geotechnica, 12(6): 13531371. Springer Berlin Heidelberg. doi:10.1007/s11440-017-0532-6.

Yamakawa, Y., Hashiguchi, K., and Ikeda, K. 2010. Implicit stress-update algorithm for isotropic Cam-clay model based on the subloading surface concept at finite strains. International Journal of Plasticity, 26(5): 634−658.

Zavarise, G., and De Lorenzis, L. 2009. The node-to-segment algorithm for 2D frictionless contact: Classical formulation and special cases. Computer Methods in Applied Mechanics and Engineering, 198(41−44): 3428−3451. Elsevier B.V.

Zavarise, G., and Laura, D.L. 2009. A modified node-to-segment algorithm passing the contact patch test. International Journal for Numerical Methods in Engineering, 79: 379−416.

Zhu, H., Zhang, L.M., Xiao, T., and Li, X.Y. 2017. Computers and Geotechnics Enhancement of slope stability by vegetation considering uncertainties in root distribution. 85: 84−89.